# Sub-gap Absorption Spectroscopy and
# Its Applications to Amorphous Semiconductor Materials

**By**

**Deniz AKDAS**

**A Dissertation Submitted to the**

**Graduate School in Partial Fulfillment of the**

**Requirements for the Degree of**

# MASTER OF SCIENCE

**Department: Materials Science and Engineering**

**Major: Materials Science**

**Izmir Institute of Technology**

**Izmir, Turkey**

**September, 2002**

We approve the thesis of **Deniz AKDAS**

                                                              **Date of Signature**


-----------------------------------------                     **14.09.2002**
**Assoc. Prof. Dr.  Mehmet GÜNES**                            ------------
Supervisor
Department of Physics



-----------------------------------------                     **14.09.2002**
**Assoc. Prof. Dr. Orhan ÖZTÜRK**                             ------------
Co-Adviser
Department of Physics



-----------------------------------------                     **14.09.2002**
**Prof. Dr. Muhsin ÇIFTÇIOGLU**                               ------------
Department of Chemical Engineering



-----------------------------------------                     **14.09.2002**
**Prof. Dr. Dogan ABUKAY**                                    ------------
Department of Physics



-----------------------------------------                     **14.09.2002**
**Asst. Prof. Salih OKUR**                                    ------------
Department of Physics



-----------------------------------------                     **14.09.2002**
**Prof. Dr. Muhsin ÇIFTÇIOGLU**                               ------------
Head of Interdisciplinary
Materials Science and Engineering Program

# ACKNOWLEDGEMENTS

# ABSTRACT

Subgap absorption spectroscopy is one of the most fundamental experimental tools to investigate absorption coefficient, $\alpha(h\nu)$, spectrum in amorphous semiconductors. The effects of the disorder and defect states can be observed in the $\alpha(h\nu)$ spectrum. For this goal, dual beam photoconductivity technique (DBP) has been established and applied to the hydrogenated amorphous silicon, (a-Si:H), thin films prepared by different deposition systems, both in the annealed and light soaked states.

In the annealed state, the effects of the native defect states in a-Si:H films were studied using dark conductivity, steady state photoconductivity and the DBP technique. The samples showed different dark and photoconductivity values. The $\alpha(h\nu)$ spectrum obtained from the DBP measured at different bias light intensities shows three regions. At high energies, parabolic extended state absorption dominates. As energy decreases below the bandgap, the exponential valence band tail absorption appears. At energies below 1.4 eV, the subgap absorption due to the midgap defect states exhibits a shoulder in the spectrum. Absorption coefficient at $\alpha$ (1.2 eV) showed variation among the films. Photoconductivity and subgap absorption values could not be correlated directly. This implies that more than one type of native defects is present in a-Si:H.

In the light soaked state, samples were left under a white light source of a few sun intensity. All the samples showed the Staebler-Wronski effect. However, the magnitude of degradation in photoconductivity is different for all the samples and is not directly proportional to the increased subgap absorption. It is inferred that both measurements are not controlled by the same defect states. As a summary, the DBP technique established in this thesis was found to be a reliable characterization tool to study amorphous and microcrystalline silicon films. The DBP results with those of photothermal deflection spectroscopy (PDS) and constant photocurrent method (CPM) techniques showed very good agreement, implying that DBP is a reliable spectroscopic tool for future investigations.

# ÖZ

Düsük enerjili isik sogurma izgegözlemi, amorf yariiletkenlerde sogurma katsayisinin enerjiye bagimliligini incelemek için kullanilan en temel deneysel araçlardan biridir. Elektronik kusurlarin ve düzensizligin etkileri, sogurma katsayisi izgegözleminde gözlenebilir. Bu yüzden, iki demetli isililetkenlik (DBP) teknigi kuruldu ve degisik sistemlerde hazirlanmis, tavlanmis ve isik altinda bozunuma ugratilmis hidrojenlestirilmis amorf silisyum ince filmlere uygulandi.

Tavlanmis durumda, a-Si:H filmlerdeki dogal elektronik kusurlarin etkileri karanlik iletkenlik, isililetkenlik ve DBP teknigi kullanilarak incelendi. Örnekler degisik karanlik ve isililetkenlik degerleri göstermektedir. Degisik isik siddetlerinde ölçülen DBP sonuçlarindan elde edilen sogurma katsayisi dagilimi üç bölge göstermektedir. Yüksek enerjilerde, parabolik dagilimi gösteren durumlardan dolayi olusan sogurma baskindir. Enerji, yasak enerji araliginin altina düstügünde, eksponansiyel valans bant kuyruk sogurmasi ortaya çikar. 1.4 eV'un altindaki enerjilerde, yasak enerji araliginin ortasindaki elektronik kusurlara bagli olarak sogurma spektrumu bir çikinti gösterir. Bu bölgedeki sogurma katsayisi degerleri filmler arasinda farklilik göstermektedir. Isililetkenlik ve sogurma katsayisi degerleri direk olarak orantili olmadigi bulunmustur. Bu, a-Si:H filmlerde, bir türden fazla dogal kusurlarin oldugunu ifade etmektedir.

Isik altinda bozunuma ugratilmis durumda, örnekler birkaç günes siddetindeki beyaz isik kaynaginin altinda birakildi. Bütün örnekler Staebler-Wronski etkisini göstermektedir. Fakat, isililetkenlikteki azalma miktari her örnek için farklilik göstermektedir ve sogurma katsayisindaki artis ile dogru orantili degildir. Buradan, bu iki ölçümünde ayni tür elektronik kusurlar ile kontrol edilmedigini çikartabiliriz. Ayrica, DBP ile elde edilen sogurma katsayisinin saptirma izgegözlemi (PDS) ve sabit isilakim teknigi (CPM) sonuçlari ile çok uyumlu oldugu gözlenmistir. Sonuç olarak, DBP tekniginin, amorf ve mikrokristal silisyum filmlerin incelenmesinde güvenilir bir karakterizasyon araci oldugu ve ilerideki arastirmalarda da kullanilabilecegi anlasilmistir.

# TABLE OF CONTENTS

# LIST OF FIGURES

# LIST OF TABLES

# CHAPTER 1

# INTRODUCTION

In the pseudo world of crystalline materials, everything is perfect due to infinite regular lattices. There are Block waves and symmetry on all sides. However, in the real world, there are many deviations from that perfection like in the situation of amorphous materials. Although amorphous materials lack the long-range order of crystals, atoms in the structure do not have random locations like those in a gas. Rather, they conserve the same short-range order of atoms as in crystalline materials. Therefore, local bonding relations are maintained and similar energy band structures at higher energies exist in both amorphous and crystalline semiconductors.

Amorphous silicon (a-Si) is one of the disordered materials showing local short-range order. It conserves approximately the same tetrahedral first nearest neighbor configuration as in crystalline silicon. However, the local ordering is lost beginning from the second nearest neighbor picture. Here, the main distinction is that the bond angles in a-Si are not $109.5^o$ like in crystalline silicon but rather are distributed with a deviation of about $10^o$. This distortion beyond the second nearest neighbor leads to the lack of translational symmetry and periodic potential of the structure. In addition, the bond lengths also show deviations from that in crystalline silicon. These result in exponential tails of localized states at the band edges extending into the forbidden gap. In these tail states, carrier mobility falls to low values at low energies and a threshold in the energy spectrum of mobilities is formed. This is called mobility edge. The energy gap between the energies of the mobility edge for electrons in the conduction band and the mobility edge for holes in the valence band is defined as the mobility gap or the recombination gap, which is slightly larger than the optical band gap of the material.

In addition to exponential tail states, unsatisfied broken bonds with different occupations of electrons also create electronic defect states near the middle of the mobility gap. These are called midgap defect states. They are mainly responsible for the recombination and generation of free carriers. Hence, these defects determine the carrier transport and lifetimes, and thereby photoconductivity. The density of these states is so large ($10^{20}$ cm$^{-3}$) that the material behaves like an insulator and a non-photoconductor. Therefore, any optically excited electron-hole pair immediately recombines.

Consequently, these large number of recombination centers makes a-Si useless for electronic applications.

The first innovation on this material was the incorporation of hydrogen in amorphous silicon in 1969. Chittick et al. [1] discovered that amorphous silicon thin films deposited by glow discharge decomposition of silane ($SiH_4$) have the density of midgap defect states to a value as low as $10^{15}\,cm^{-3}$, a concentration that allows Fermi level to be moved by doping. This new material was then called to be *hydrogenated amorphous silicon (a-Si:H)*. A distinctive feature or disadvantage of these films prepared by glow discharge deposition is their high dark resistivity, which is appreciably larger than that of films prepared by evaporation [2] and sputtering [3] techniques. However, in 1975, Spear and Le Chomber [4] showed that hydrogenated amorphous silicon (a-Si:H) could be doped as n-type or p-type by adding phosphine ($PH_5$) or diborane ($B_2H_6$) to the plasma, respectively. Thereby, a-Si:H became a convenient material to be used in electronic device applications such as p-n junctions. It was observed that these doped materials satisfied a very low overall density of midgap defect states, a narrow range of band-tail states below the conduction band and above the valence band. Figure 1.1 shows the possible states in the bandgap of a-Si:H. In addition, the doping increases the conductivity of specimens by about five to seven orders of magnitude. In another study, the same authors reported the first amorphous semiconductor junction, which is an amorphous silicon p-n junction [5]. Previous junction studies in this area involved placing the amorphous material in contact with a metal [6], a crystalline semiconductor [7], or heterojunctions [8]. Right after this discovery in 1976, the first hydrogenated amorphous silicon solar cell was reported by Carlson and Wronski [9] with a power conversion efficiency of 2.4% using hydrogenated amorphous silicon p-i-n structure.

In fact, the significant role of hydrogen was not fully appreciated by these researchers. After infrared absorption [10] and hydrogen evolution [11] experiments were performed, in which materials contain up to 50% hydrogen, it was accepted that hydrogen plays a significant role in passivating dangling bonds. Thus, it removes a large number of midgap defect states in the gap and permits the Fermi level to be shifted in the bandgap. Hydrogen also modifies the amorphous network by inserting itself into weak bonds. Thereby, it removes the disorder in the amorphous network, which results in sharpening the valence band tail and widening the gap. Furthermore, the increased hydrogen content in the film as much as 10-15% improves photoconductivity.
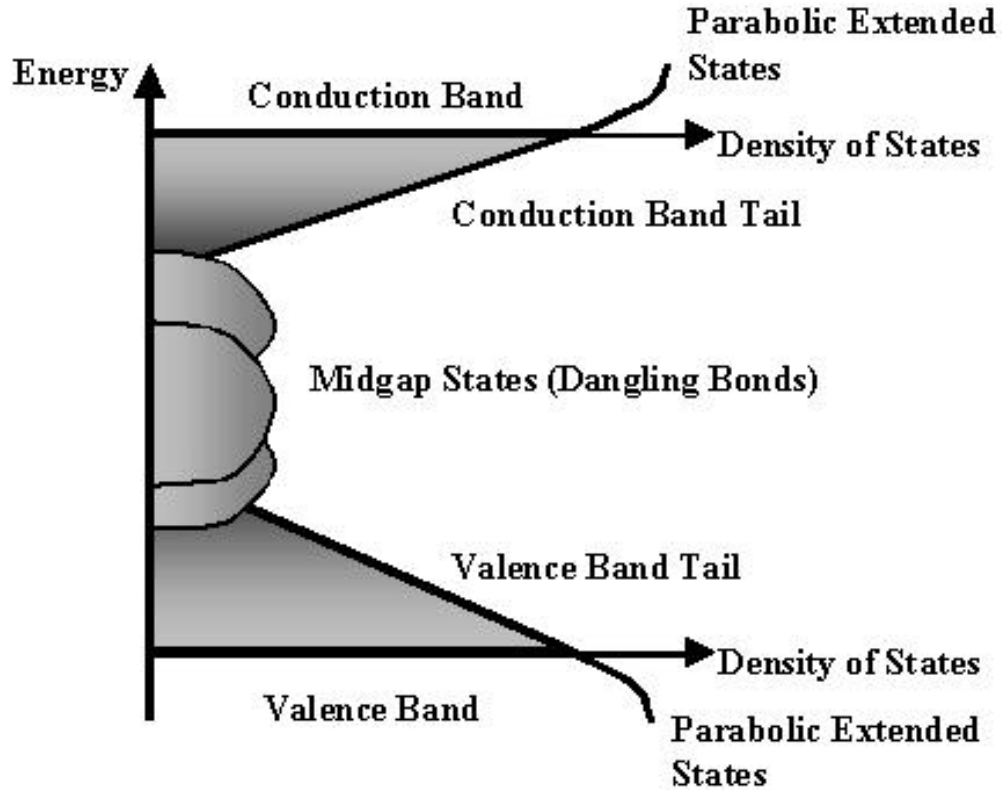
Figure 1.1    The schematic illustration of the energy distribution of gap states for a-Si:H material. In crystalline silicon, the tail and midgap states are not observed.

All these improvements and understanding the role of hydrogen have led to a number of studies on a-Si:H and it has been extensively studied due to its technologically important applications. Today, a-Si:H is widely used in large area electronic applications such as photovoltaic cells, photoreceptors, image sensors, thin film field effect transistors, memory junction devices. It possesses very attractive features which may be summarized as follows: The most important property is that hydrogenated amorphous silicon thin film has larger optical absorption than single crystalline silicon in the visible region of spectrum; It absorbs sunlight extremely well so that only a very thin active layer of about 1 $\mu$m is sufficient for solar cells. As a comparison, a thickness of about 200 $\mu$m active layers is necessary in single crystalline solar cells. Secondly, although a-Si:H behaves like an insulator in its undoped state, when it is doped, it is highly conductive ($\sigma \propto 10^{-2} \, \Omega^{-1} \, cm^{-1}$). Third attractive property is that it has an adjustable bandgap when doped with Germanium, Carbon and Hydrogen.

This property allows manufacturing of multijunction solar cells to absorb the whole solar spectrum efficiently. Since the material is amorphous, there is no lattice-matching problem seen as a major problem in the single crystalline multilayer devices. The fourth property is related to its cost. It can be deposited as large area thin films (about 1 m$^2$) on inexpensive materials such as glass, plastics, and sheet steel at low substrate temperatures (200 $^o$C-250 $^o$C). Finally, it can be finely patterned with photolithography due to its low Vicker's hardness.

Even though hydrogenated amorphous silicon has many advantages, there is a main disadvantage of these materials. In 1977, Staebler and Wronski [12] discovered that both dark conductivity and photoconductivity of a-Si:H thin films decrease after being exposed to white light illumination. In addition, conversion efficiency of solar cells made from this material also decreases after long-term illumination. These conductivities can be perfectly restored to their original values by annealing the films above 150 $^0$C. This phenomenon is known as the *Staebler-Wronski Effect* (SWE). Those observed changes were attributed to a reversible increase of the density of midgap defect states acting as recombination centers for photoexcited carriers and leading to a shift of the dark Fermi level toward the midgap. Direct evidence for the creation of midgap states by light comes from a variety of experiments: reversible changes in the field effect [13,14], deep-level transient spectroscopy [15], defect luminescence [16], sub-bandgap absorption [17], and an increase of silicon dangling bond signal in electron spin resonance (ESR) [18,19]. Subsequent studies on hydrogenated amorphous silicon thin films produced by various deposition conditions such as SiH$_4$ diluted with H$_2$ [18], SiH$_4$ diluted with Ar [20], SiH$_4$ diluted with SiF$_4$ [21], reactive magnetron sputtering [22] and homogenous chemical vapor deposition [23] showed that they all exhibit reversible light induced changes, i.e. Staebler-Wronski effect is an intrinsic property of a-Si:H films. Studies using different films indicated that the amount of reversible light induced changes depend on fabrication conditions, doping and impurities. Overall, the different studies concluded that illumination with intense light leads to the creation of additional metastable states in the mobility gap of a-Si:H which influences its electronic and optical properties by decreasing the lifetime of excess carriers and shifting the position of the dark Fermi level in a reversible manner. However, discrepancies in interpretations still exist regarding the absolute density of the metastable defects, their energy locations and distributions in the mobility gap.

After the observation of reversible light induced changes on different films, the importance of hydrogenated amorphous silicon based materials increased. Many researchers have been investigating the reasons behind the Staebler-Wronski effect (SWE) and how to eliminate its results. Until now, many models have been proposed to reveal the mechanism of light induced defect creation and what is happening in the midgap region. However, none of these models have been widely accepted as a satisfactory explanation for the SWE in amorphous silicon based materials yet.

Staebler and Wronski proposed two possible models in an early paper [24]. They hypothesized that light exposure leads to bond reorientation and atomic displacements at localized defects associated with hydrogen or a transfer of electrons to deep defects. Pankove and Berkeyheiser [16] suggested that the breaking of weak Si-Si bonds by light is responsible for the effect and thus dangling bonds are created. Actually, the first observation of light induced dangling bonds in undoped a-Si:H was reported by Dersch et al. in 1981 by using Electron Spin Resonance (ESR) [19]. Today, it is widely believed that most optoelectronic properties of a-Si:H are controlled by the threefold-coordinated silicon defect called dangling bond, which is the most common defect in a-Si:H materials. The dangling bond may have one of three charge states: positive (+), neutral (0), or negative (-). These three states correspond to a diamagnetic-positively charged state ($D^+$) with no electrons, a paramagnetic-neutral state ($D^0$) occupied by one electron and a diamagnetic-negatively charged state ($D^-$) occupied by two electrons, respectively. All of these states have a metastable configuration that is a broken bond on a silicon atom. A two dimensional picture of a-Si:H structure is shown in Figure 1.2.

A different picture from the dangling bond or the broken bond model of SWE involves reversible changes in the charge or hybridization state of already existing dangling bonds. This type of mechanism has been proposed by Adler [25]. According to this model, the neutral state has three of the same $sp^3$ hybrid bonds as for tetrahedral bonding, even though the fourth bond is broken. The bond angles are the same as in the ground state configuration, $109.5^o$. The neutral state defects contain an unpaired spin, which is observed by its ESR signal. The positively charged state is associated with rehybridized bonds that become $sp^2$ with a $120^o$ bond angle. The negatively charged state is associated with $p^3$ bonding with a $95^o$-$100^o$ bond angle. Because the ground state of the isolated Si atom is $s^2p^2$, another possible defect is the twofold-coordinated Si atom in its neutral state. Such states are spin paired and exhibit no ESR signal. These states can produce up to four localized states in the gap: two filled and two empty.
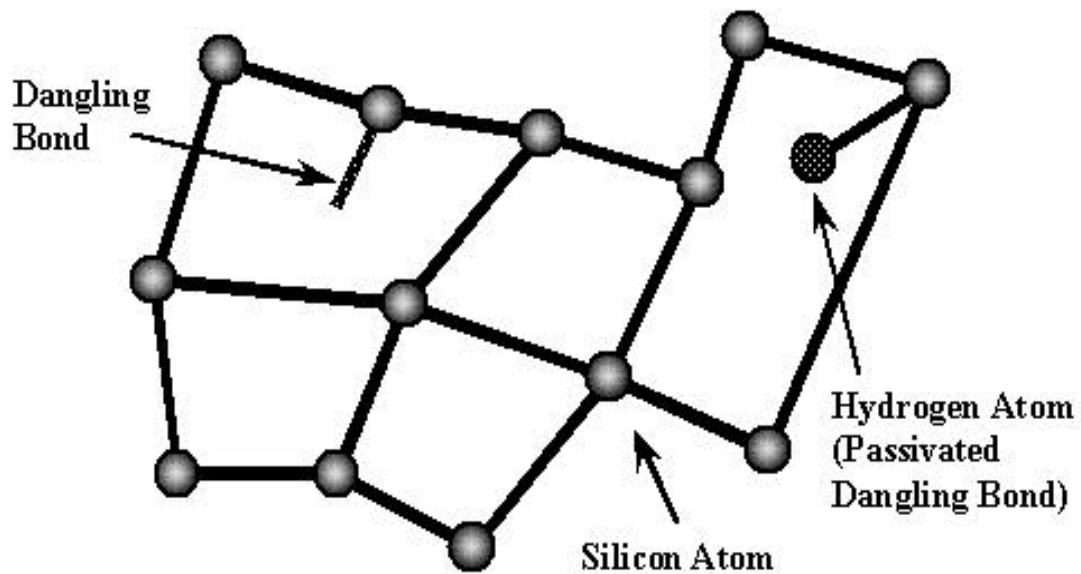
Figure 1.2    Two dimensional picture of a-Si:H structure. Hydrogen plays a passivating role for the dangling bond.


In Adler's model, positively and negatively charged states capture photoexcited carriers under light soaking. Then, they are converted to neutral rehybridized metastable states (neutral dangling bonds). Hence, carrier capture by the existing charged defects is central to the formation of the metastable state, i.e. new defects are not formed [26]. The defects have negative effective correlation energy ($U < 0$), which is the repulsion between two electrons with opposite spins, and U is on the order of a few tenths of an eV for localized state.

Another widely accepted model is the defect pool model, which is based on an assumption of a broad distribution (defect-pool) of possible energies for the dangling bonds within the bandgap. The general principle of the model is that dangling bonds are formed by the breaking of weak Si-Si bonds [27], which are stabilized by diffusive hydrogen motion through breaking and reforming Si-H bonds [28,29]. The density of dangling bonds is determined by a chemical equilibrium between the weak bonds and the dangling bonds. The equilibrium density of dangling bond states depends on the Fermi energy, which leads to a higher density of dangling bonds in doped a:Si-H than undoped a-Si:H [30,31].

The genesis of the defect pool model lies in the work of Bar-Yam and Joannapoulos [32], who first pointed out that the formation energy of a defect depends on its charge state and that the difference in the formation energies depends on the Fermi energy and the energy of the defect itself. Stutzmann [27] introduced the weak bond-dangling bond conversion model and proposed that the transitions are intimately connected with charged state effects. Like most weak-bond pictures, his proposal has a neutral ground state and this state is converted to a dangling bond that may or may not be charged, depending on the Fermi Energy. There are similarities between this kind of model and that of Adler, with the exception that Adler favored a negative U and did not change the total number of dangling bonds, only their charge state. Smith and Wagner [33] identified the weak bond energies with the valence band tail states, which are exponentially distributed in energy, giving a further distribution of formation energies. Winer [34] brought together these different aspects as a modern defect pool model. He was the first to incorporate weak bond-dangling bond conversion and to explicitly include hydrogen entropy in the chemical reaction of microscopic defect formation. He calculated the density of states in undoped and doped a:Si-H and proposed that $D^-$ defects in n-type a:Si-H were lower in energy than $D^+$ defects in p-type a:Si-H. Winer assumed that the density of states was dominated by defects with only one charge state in each type of material (negative in n-type, positive in p-type, and neutral in intrinsic). Schumm and Bauer extended this work by first considering the simultaneous formation of defects in all three charge states [35], but only later realized the importance of weak-bond depletion by defects of all three charge states [36]. Their results showed more charged defects than neutral defects in intrinsic a-Si:H. With a somewhat similar model, Branz and Silver [37] also concluded that there were more charged defects than neutral defects but expressed their model in terms of potential fluctuations. They pointed out that even if U>0 charged defects exist in some regions due to local potential fluctuations. They later refined this version of Adler's model in 1991 with much experimental evidence for charge trapping in the metastable configurations [38]. According to this model, the charged dangling bond defects form in a-Si:H films due to inhomogeneity and equilibrium statistics. Inhomogeneities (H clusters, microvoids, and impurities) create short-range potential fluctuations of about 0.3 eV full-widths, which are observed as the defect band width in optical absorption and other experiments. In the models of Bar-Yam and Joannopoulos [32], and Branz and Silver [37], there is no

weak bond-dangling bond conversion and no microscopic mechanism for the defect formation process.

Unlike the other models, Pantelides explained the overcoordination concept and proposed that fivefold and threefold-coordinated silicon dangling bonds are primitive conjugate intrinsic defects in a-Si:H [39-41]. According to this model, D center is fivefold-coordinated silicon with an unpaired electron in a state labeled that defect as "floating bond". During the prolonged illumination both dangling and floating bonds are created. As a floating bond, dangling bonds are nonmagnetic and have negative correlation energy U. Floating bonds are analogous to the interstitial whereas dangling bonds are analogous to the vacancy in crystalline materials.

In addition to the models proposed during the history of studies on a-Si:H, new defect models proposed by Branz and Biswas [42] appear distinctly as new perspectives. Branz's model is called as "hydrogen collision model". In this model, it was proposed that when two mobile hydrogen atoms generated by light induced carriers collide, they establish metastable, immobile complexes involving two Si-H bonds. Light induced metastable dangling bonds remain at the uncorrelated sites from which the colliding hydrogen atoms were excited. Thus, mobile hydrogen association into Si-H bond pairs is the vital step that creates metastable defects and mobile hydrogen density is the main parameter in this model.

On the other hand, "silicon network rebonding model" developed by Biswas et al. [43] is based on the breaking of the weak silicon bonds due to non-radiative recombination of photoexcited electron-hole pairs coupled with silicon and hydrogen bonding rearrangements in the amorphous silicon network. The broken bonds lead to the production of dangling bond and floating bond pairs. Since floating bonds are mobile species (from studies of Pantelides), they migrate away from the dangling bond site leaving an isolated dangling bond. Finally, two migrating floating bonds in the network come in close and recombine leading to the annihilation of floating bonds and generation of a new weak secondary dangling bond in the lattice. Hence, according to this proposal, the creation of light induced dangling bonds is caused by extended rearrangements of the silicon bonding network without direct participation of hydrogen.

According to the models described above, the explanation of metastability in a-Si:H can be divided into three group: The first group of models propose that existing defect states undergo structural modification. A sufficient density of localized structural defects (such as dangling bonds) is subjected to a considerable change of their

respective energy levels due to trapping of excess carriers without corresponding changes of the bonding topology. Charge induced structural relaxation of these defects increases the probability of negative correlation energy, which is the sum of the positive coulomb repulsion and the negative strong relaxation energy. In other words, these models can be termed as negative -U models. The second group is that local changes can occur in the bonding topology. In these models, such as Stutzmann's model [27], metastable defect formation is a consequence of local changes in the coordination of network atoms (charge induced bond breaking or bond formation). Charge trapping or recombination leads to atomic displacements that alter the coordination number of network atoms, predominantly in the vicinity of the trapping or recombination site. The final group includes the thermal equilibration models. According to these models, the entire macroscopic system relaxes toward a state, which is determined by a small number of external and internal state variables. Details of the microscopic processes leading to metastable state formation are unimportant, and are replaced by assumptions concerning the free energies of the ground state and the metastable state. In these types of models, bonding configurations and structural changes whose electronic activity depends on the presence of hydrogen atoms (the creation of metastable dangling bonds by hydrogen switching) exhibit a thermal-equilibrium behavior.

All these models have tried to present macroscopic and microscopic explanations of the metastability in a-Si:H. However, the non-crystalline structure of a-Si:H material itself is very convolute whether it is in native or in light soaked situation. Hydrogenated amorphous silicon thin films cannot be fabricated as a unique type since deposition conditions of the system determine their optical and electrical properties. From the microscopic point of view, each product (a-Si:H thin film) will be different from the others even if the deposition conditions are exactly the same. Therefore, it is difficult to construct a model, which covers all the phenomena including metastable defect formation, the energy positions and distribution of defect states etc. That is why none of these models have been satisfactorily successful in explaining the observed facts in a-Si:H yet.

Whatever the models try to elucidate, the major aim of all these studies is to put a-Si:H into action in the most efficient way by choosing the most convenient characterization techniques. Since the ultimate goal is to incorporate a-Si:H in to a wide variety of electronic devices, studies have focused on defining the properties which lead to the best performance known as device quality criterion for a-Si:H materials. A defect

density of $10^{15}$-$10^{16}$ cm$^{-3}$ is convenient for the device quality a-Si:H thin films. As mentioned before, defect density, light induced defects and their origins, defect distribution and types of defects are the main parameters that have been discussed and have led to extensive research on these materials by using various techniques. Each of these techniques has distinct sensitivities and limitations. They are mainly based on magnetic, electrical and optical characterizations. These techniques are spectroscopic ellipsometry [44,45], transmission and reflection [46], field effect transistor measurement [13,14], capacitance [15,47,48], steady state photoconductivity [49,50], electron spin resonance (ESR) [18,19,51], and sub-bandgap absorption techniques [52-54].

Spectroscopic ellipsometry [44,45] is mainly used to find depth-profiles of interfaces, thin films and multilayer structures, the composition for any layers (bulk, interface, or surface) which are composites or alloys, and the microroughness of the surface layer. Since it is sensitive to very thin layers, it is used to determine absorption coefficient for photon energies greater than the band gap energy. The density of extended states is deduced from the imaginary part of the dielectric function. The most accurate values of the dielectric functions (i.e. the real and the imaginary parts of the optical dielectric constant as a function of wavelength) of semiconductors, metals and even wide band gap materials as thin films can be obtained using this technique.

Transmission and reflection (T&R) measurements [46] are used to determine the optical absorption coefficients where photon energies are greater than the band gap. Midgap states located below bandgap energies do not respond to T&R measurements. In this method, the intensity of light reflected and transmitted by the sample from a beam of known intensity as a function of photon energy is measured. The absorption is proportional to the difference between the incident, the reflected and transmitted light intensities. Absolute optical absorption coefficient $\alpha$ (h$\nu$) is obtained by using the measured T&R spectra and detailed thin film physics. Absorption coefficient spectrum is then used to determine the optical bandgap of the material. The most common procedure to find out the optical bandgap is to use Tauc relation, $(\alpha h\nu)^{1/2} = C(h\nu - E_{GAP})$ [46]. The optical bandgap can be estimated using the zero intercept of $(\alpha h\nu)^{1/2}$ versus h$\nu$ plot. However, T&R method cannot give reliable absorption coefficient spectra for films thinner than 2 $\mu$m at energies lower than the optical bandgap.

In field effect transistor measurement [13,14], a voltage applied on the gate electrode induces a highly conductive channel inside a-Si:H. The observed change in conductance depends on how far the Fermi energy is moved by the field, which in turn depends on the density of states. However, field effect measurements are very sensitive to interface states and field effect data may be insensitive to changes in density of states, especially near the midgap.

Capacitance techniques like Deep Level Transient Spectroscopy (DLTS) [15,47,48] require a sample that is typically in the form of a film on a heavily doped crystalline substrate or a thin metal layer that serves as the bottom electrode. DLTS gives the distribution of midgap states in terms of thermal emission energy of the gap state electrons or holes to the nearest mobility edge. The absolute number of such emitted changes can be determined by analyzing the change of the carrier capacitance that is observed. Capacitance measurements can distinguish the sign of trapped charge within the depletion width by the sign of the capacitance change. The contact requirements are less stringent than for current measurements and the measurement is most sensitive to the bulk of the sample, i.e., it is less affected by the surface. The major disadvantage of these measurements is that, because of the requirement to transport charge in and out of the sample, the sample resistivity cannot be too high. Thus, undoped samples or samples with large densities of defects are not suitable for capacitance measurements.

Steady state photoconductivity measurement gives information about the nature of defects, transport and recombination kinetics of photogenerated carriers [49,50] through mobility-lifetime product. In a-Si:H materials, photoconductivity exhibits non-integer power law dependence on light intensity which is a consequence of the continuous distribution of gap states. Since the states between quasi-Fermi levels act predominately as recombination centers, steady state photoconductivity is sensitive to both the density and nature of these states. However, it is difficult to analyze the results of steady state photoconductivity to obtain quantitative information about the free carrier mobilities and the densities of the midgap defect states.

Electron spin resonance (ESR) senses only those dangling bonds having a single electron in them since those with either zero or two electrons are diamagnetic [18,19,51]. The observed well-known g (gyromagnetic ratio) value of 2.0055 indicates that the light induced defects responsible for SWE and the change of luminescence spectrum are due to the dangling bonds. The strength of the signal is also taken as a

measure of bulk density of these defects [51]. The main disadvantage of the ESR technique is that the neutral silicon dangling bond is not the only type of defect state located in the bandgap of a-Si:H, which is described in defect models as previously mentioned . The technique is also sensitive to the surface states for films with thickness less than a few micrometers.

Sub-bandgap absorption spectroscopy [52-57] techniques are very powerful methods to measure the absorption coefficient at lower energies below the bandgap energy. They give qualitative and quantitative information about the density, nature, and distribution of the electronic defect states in the bandgap region. These techniques have been especially developed to study a-Si:H thin film materials. They are Photothermal Deflection Spectroscopy (PDS) [52], Constant Photocurrent Method (CPM) [53] and Dual Beam Photoconductivity (DBP) [50,54-57] techniques. Their sub-bandgap absorption spectra are complementary to T&R spectra to investigate especially midgap defects in the annealed and light soaked states. These techniques are based on distinct assumptions and have different experimental arrangements. PDS is based on measuring beam deflection due to thermal energy change near the film surface whereas CPM and DBP spectra are obtained by measuring photocurrent due to transitions from electron occupied defects states into the conduction band. It is generally accepted that both CPM and DBP spectra reflect bulk defect states but PDS involves the influence of surface states, which is a consequence of additional transitions from and into the localized states near midgap. However, in CPM technique, since low generation rate of monochromatic light is used, the lifetime of the electron is almost constant and thereby only the electron occupied defect states below the Fermi level can be detected. The major advantage of DBP over CPM is that different bias light intensities can be used to detect more gap states, which is called the intensity dependence of the sub-bandgap absorption in DBP spectrum. Increasing bias light leads to the splitting of the quasi-Fermi levels towards the band edges. Therefore, in DBP technique, the defect states both below and above the Fermi level can be detected. In this study, dual beam photoconductivity technique has been established to investigate the defect states in a-Si:H based materials.

## 1.1 Thesis Objectives

Due to attractive features and technologically important applications of a-Si:H based materials, it is crucial to obtain reliable information about the densities and nature of the native and light induced defect states. Despite the mysteries behind the mechanism of light induced defect creation which have been studied over the last twenty-five years, a-Si:H based materials are needed to be investigated for further developments, such as more efficient solar cells, memory junctions, liquid crystal displays (LCD), light emitting diodes (LED), and oversensitive detectors.

It is essential to choose convenient characterization techniques to understand the effect of native and light induced defect states and to obtain feedback information for improving these materials. The objective of this thesis is to characterize undoped a-Si:H based thin films in the annealed and light soaked states by using steady state photoconductivity and sub-bandgap absorption spectroscopy techniques. Dual Beam Photoconductivity (DBP) technique has been established as a main goal of this thesis to obtain reliable sub-bandgap absorption coefficient spectra. The DBP system was established and calibrated using detailed light flux calibration. Then, magnitude and phase of sub-bandgap photoconductivity of a-Si:H films have been measured for different bias light intensities. In addition, transmission spectra of a-Si:H films have been recorded using a pyroelectric detector placed behind the samples and used to obtain the thickness of the films. Obtained sub-bandgap photoconductivity spectra will be normalized to the absolute absorption coefficient spectra measured either by T&R or PDS method. Resulting absolute sub-bandgap absorption spectra will be used to obtain valence band tail slope, $E_{0V}$, and to estimate the midgap defect states in the annealed and light soaked films. The results on different a-Si:H films will be compared and discussed.

# CHAPTER 2

# SUB-BANDGAP ABSORPTION SPECTROSCOPY
# AND THE OTHER CHARACTERIZATION TECHNIQUES

## 2.1 Introduction

Since amorphous materials possess continuous distribution of midgap states, photons whose energy less than the bandgap energy can also be absorbed by these materials. When photons with low energy impinge on an amorphous material, they can scatter electrons in the gap states into conduction band. The rapid scattering of free carriers leads to a large uncertainty in the electron and hole momentum. Thus, conservation of momentum can be no longer applied to transitions and the distinction between direct and indirect transition disappears. Hence, all optical transitions are allowed. Since these transitions involve the knowledge about defect states in the bandgap and carrier transport of the amorphous material studied, it is essential to obtain absorption profile of the material. Sub-bandgap absorption spectroscopy is a commonly used technique to characterize the optoelectronic quality of thin films for various device applications. Technically speaking, it is a direct way to obtain the spectral dependence of absorption coefficient, $\alpha$, in low absorption region ($10^{-2}$-$10^{3}$ cm$^{-1}$) [17,50,52,57]. The absorption coefficient spectrum is directly related to electronic transitions between extended, band tail and midgap defect states. Quantitative information on the density of states and valence band tail slope can be deduced from the optical absorption coefficient spectrum. The absorption coefficient, $\alpha(h\nu)$, is expressed in terms of the density of initial and final states and can be written as:

$$\alpha(h\nu) = \frac{C}{h\nu} \int_{-\infty}^{\infty} \left[N_{LOC}(E)\,f(E)\right]\left[N_{EXT}(E+h\nu)\right]\left[1 - f(E+h\nu)\right]dE \quad (Eq.2.1)$$

where $N_{LOC}$ (E) is the density of localized states at energy E, $N_{EXT}$ (E) is the density of extended states at energy E, f(E) is the occupation function at energy E, and C is a constant determined by the optical transition matrix elements, and h$\nu$ is the photon energy.

A characteristic absorption spectrum of a-Si:H thin film is shown in Figure 2.1. In this figure, there are three absorption regions. At above 1.8 eV, a parabolic absorption region exists due to electron transitions from parabolic valence band states to the conduction band extended states. In addition, the absorption spectrum of a-Si:H in red and near infrared region shows an exponential decaying region (Urbach edge) and a the residual shoulder (sub-bandgap absorption) below 1.4 eV. Parabolic region is caused by absorption of photons with energies greater than the band gap energy where $\alpha$ (h$\nu$) $>10^3$ cm$^{-1}$. The absorption coefficient in this region is also measured by spectroscopic ellipsometry [44,45] and transmission and reflection [46] techniques.

Excitations from the valence band tail states to conduction band due to absorption of photons with energies less than the bandgap energy results in an exponential region, $\alpha$ (h$\nu$) = C exp (E/E$_{0V}$), where the absorption coefficient is generally between 10 cm$^{-1}$ and 1000 cm$^{-1}$. The slope of the valence band tail (Urbach tail), E$_{0V}$, is the measure of the disorder in the amorphous network. In other words, it is an indication of the device quality parameter of these materials.

Absorption coefficient below 1.4 eV is due to excitations from deep lying states to conduction band it exhibits a shoulder in the spectrum. The absorption coefficient in this region lies down to $10^{-2}$ cm$^{-1}$. The shoulder in the sub-bandgap absorption spectrum is the most important part for the amorphous semiconductors since it gives information about the density of midgap states. These states lie in the midgap and mainly control the recombination kinetics of the material, thereby $\alpha$ (h$\nu$) below about 1.4 eV is an indication of usefulness of these materials in electronic applications. The main feature of the sub-band gap absorption curve in the low photon energy region is that it shows fringes rather than a smooth curve for films thinner than 2 $\mu$m due to multiple reflections at the film-substrate interface. There are no fringes in the real absorption spectrum. These fringes depend on the film thickness, for thicker films the fringes are smaller and closer together. For thinner films (t $\leq$ 0.7$\mu$m) the fringe pattern is less distinguishable from the actual spectrum. Generally, fast Fourier transform (FFT) smoothing procedure is applied to obtain actual fringe free $\alpha$ (h$\nu$) spectrum [66].
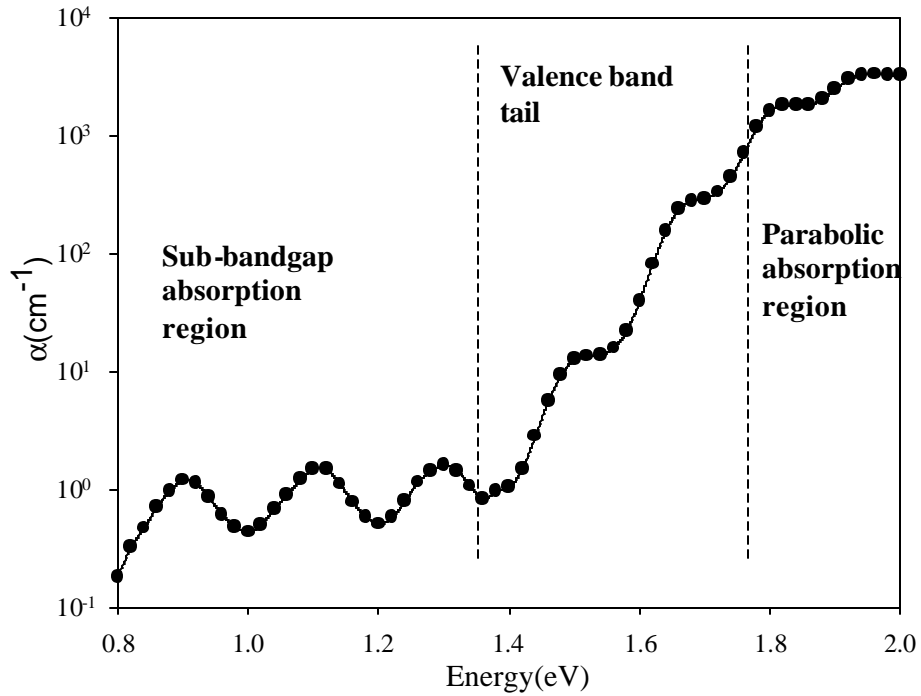
Figure 2.1.    Characteristic optical absorption spectrum of an undoped a-Si:H.

In order to obtain reliable sub-bandgap absorption coefficient spectra of the amorphous semiconductors, new techniques have been developed. These techniques are Photothermal Deflection Spectroscopy (PDS) [52], Constant Photocurrent Method (CPM) [53] and Dual Beam Photoconductivity (DBP) [50,54-57]. These techniques are based on different assumptions and their absorption spectra need to be calibrated by T&R data to obtain the absolute absorption coefficient values. Although all methods yield identical spectra of Urbach tail, their sub-bandgap absorption regions below about 1.4 eV differ occasionally. Especially the PDS spectra show large deviations from that obtained by CPM and DBP. Such differences are often ascribed to the influence of surface states and substrate or compensated by different calibration factors. All methods are highly sensitive ($\alpha t \sim 10^7$ for solids) and useful for obtaining information about parameters like the sub-bandgap defect density and valance band tail slope. In the following sections, these techniques and their underlying principles are explained in detail.

## 2.2 Photothermal Deflection Spectroscopy

Photothermal Deflection Spectroscopy (PDS) is based on measuring thermal energy deposited in the material when photons are absorbed. It has been developed by Jackson et al. [52]. Experimental setup of PDS is shown in Figure 2.2. An intensity modulated pump beam is absorbed by the thin film, which is immersed in the carbon tetrachloride ($CCl_4$). The pump beam results in a periodic heating. Heat is transferred to the $CCl_4$ medium causing a corresponding modulation in the index of refraction near the film surface. The probe beam grazing the film surface, experience a periodic deflection synchronous with intensity modulation. The amplitude and phase of this periodic deflection are measured with a position sensor and the outputs of position sensor are amplified by current amplifiers and fed into the A-B input of lock-in amplifier. Thus as the wavelength of the pump beam is varied, the deflection of the probe beam becomes a measure of optical absorption spectrum of the thin film. PDS is a difficult measurement and very sensitive to small modulations of probe beam. Therefore, very low vibration and fine adjustment are required to obtain reliable data.
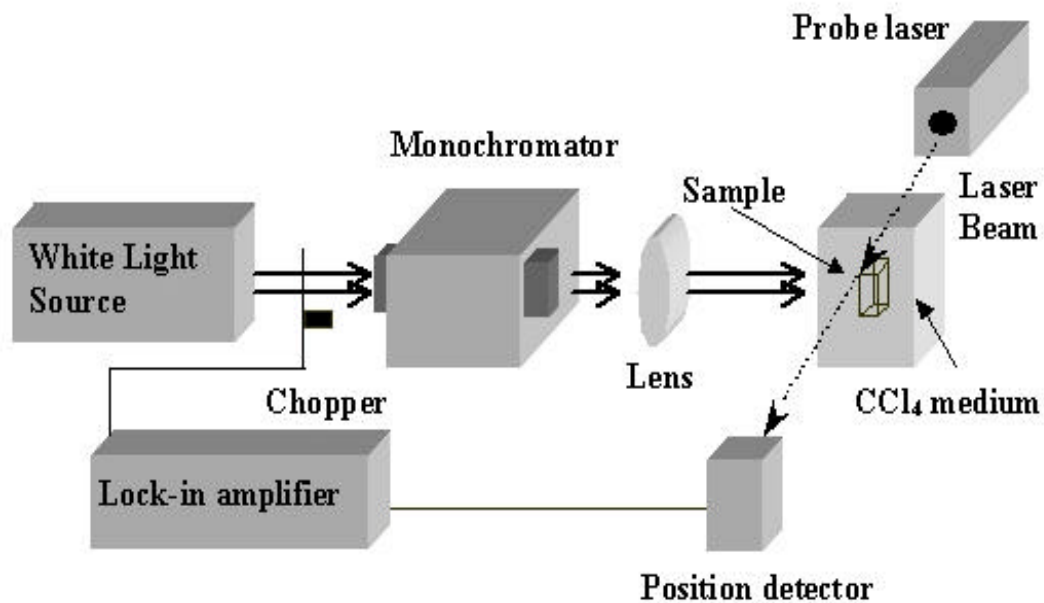


Figure 2.2.    The experimental arrangement of photothermal deflection spectroscopy.

Since PDS process is not a photoconductivity measurement, it does not depend on the Fermi level position. It is commonly believed that this technique is sensitive to surface, interface and bulk states. In other words, it measures all possible optical

transitions from and into the localized defect states in the mobility gap as illustrated in Figure 2.3. In addition to transitions into the conduction band (I, II, IV), PDS detects also the other transitions (III, V, VI), which are not observed in any photoconductivity measurement. The contribution of the other transitions appears as high sub-bandgap absorption in the optical absorption spectrum of PDS. Since surface and interface defects affect the absorption spectra, for accurate measurements, a series of high quality films with different thicknesses must be investigated to interpret sub-bandgap absorption correctly. Figure 2.4 gives an absorption spectrum obtained by PDS and also by CPM, which will be discussed in the next section. It can be observed that as the thickness of the film becomes smaller, the sub-bandgap absorption of the PDS spectrum increases since the contribution of surface defects to absorption becomes higher than the bulk defects. Two methods are used to obtain the density of defect states from the PDS spectrum. These are the deconvolution of the optical spectrum [55,58,59] and the integration of the excess sub-bandgap absorption [52,60,61]. Both methods are based on some assumptions and require calibration constants from ESR measurements. The constant of integration of the excess absorption for PDS is $7.9 \times 10^{15}$ cm$^{-2}$ eV$^{-1}$ [52]. These methods will be explained in next section in detail with CPM technique since CPM uses the same methods to acquire the density of defect states.
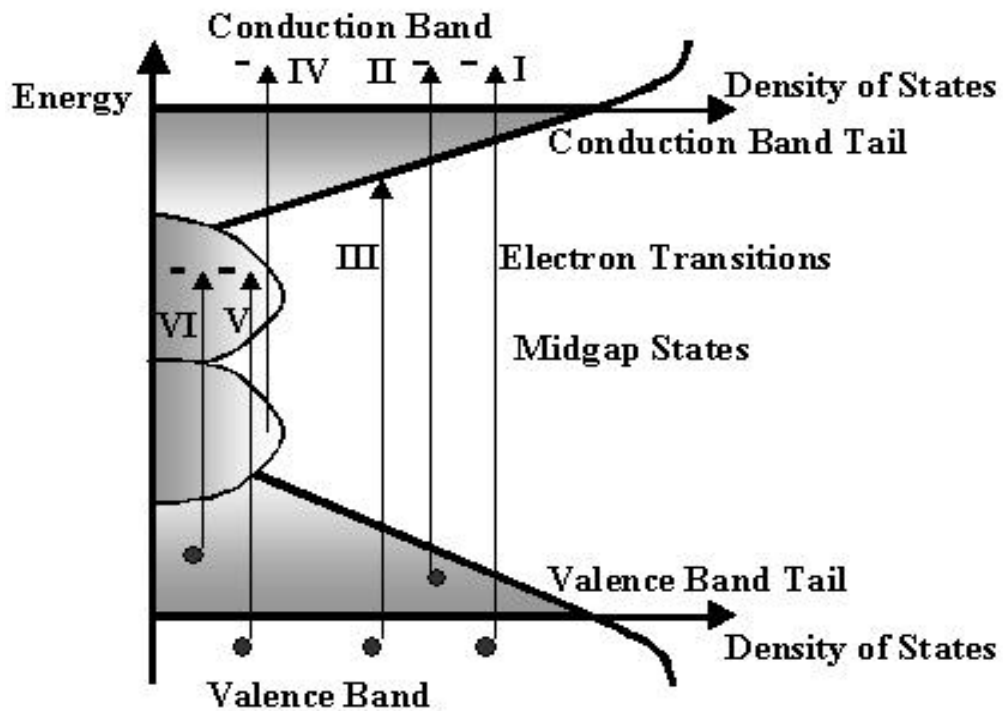


Figure 2.3.    Possible optical transitions in undoped a-Si:H where (-) denotes electrons and (●) denotes holes.
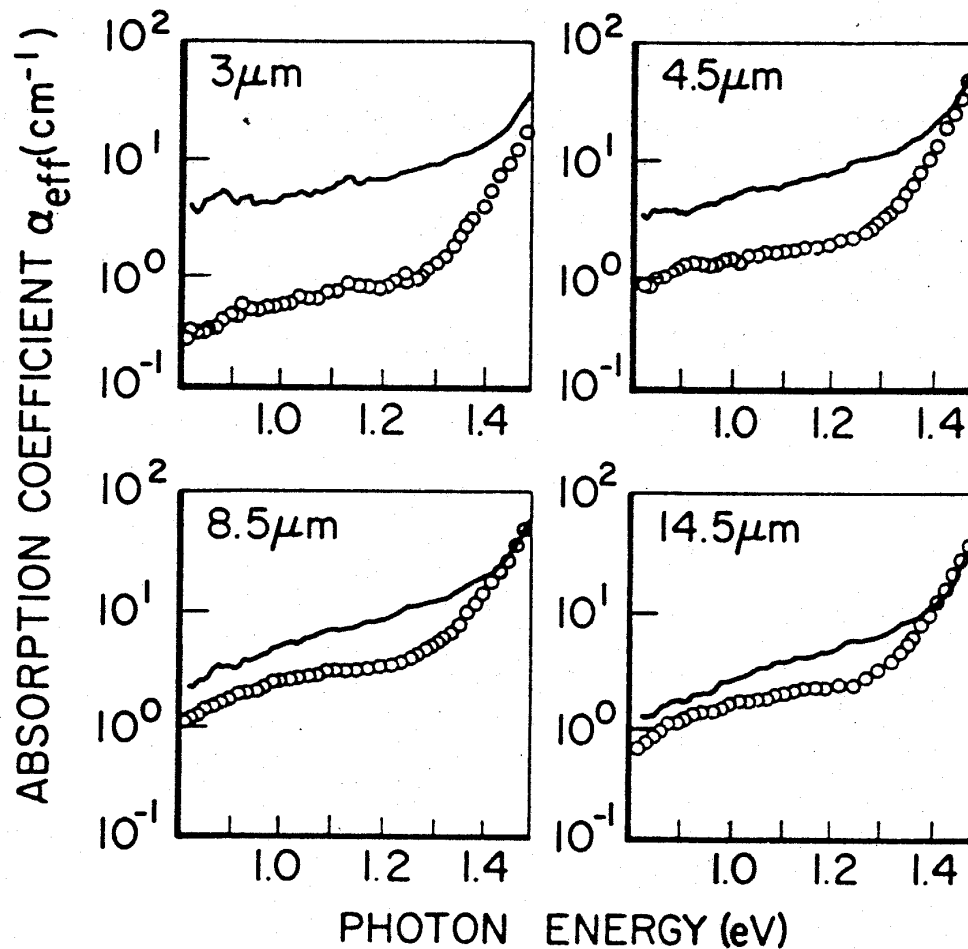
Figure 2.4.    Absorption coefficient spectra of a-Si:H films measured by both PDS (solid line) and CPM (circled line) [67]

## 2.3 Constant Photocurrent Method

Constant photocurrent method (CPM) was invented by Grimmeiss and Ledebo for the measurement of the spectral dependence of photoionization cross-section of deep impurities in semiconductors and applied to the investigation of deep levels in monocrystalline GaAs [68]. Then, it was developed for a-Si:H films as a quantitative determination method for the gap states density below the Fermi level [53].

In the CPM technique, photocurrent is maintained constant over the range of photon energy to get constant quasi-Fermi levels. Constant photocurrent implies that the steady state concentration and the lifetime of photogenerated electrons are constant, and thus the recombination mechanism is unchanged. The other assumptions are uniform

illumination where $\alpha$ t <<1, weak spectral dependence of reflectivity, dominant electron photocurrent, drift mobility independence of energy and constant quantum efficiency. The theoretical idea of CPM can be derived as the following:

Constant photocurrent sets a constant generation rate G as given by:

$$G = \frac{F(h\nu)\,\eta(h\nu)\,[1-R(h\nu)]\,[1-\exp[-\alpha(h\nu)\,t]]}{t}$$  (Eq.2.2)

where F is the incident flux in $(cm^{-2}s^{-1})$, $\alpha$ is the absorption coefficient at applied monochromatic light energy, $\eta$ is the quantum efficiency, R is the reflectivity of the material, and t is thickness of the film. In the low absorption region where $\alpha$ t <<1, R and $\eta$ are expected to depend little on h$\nu$, and thus the above equation reduces to:

$$G = F(h\nu)\,(1-R)\,\alpha(h\nu)$$  (Eq.2.3)

Therefore, a constant G implies that absorption coefficient is inversely proportional to flux. This can be written as the fundamental assumption of the CPM:

$$\alpha(h\nu) \propto \frac{1}{F(h\nu)}$$  (Eq.2.4)

where the absorption coefficient can be extracted by calibrating the data at high energies to the absorption spectra obtained from other measurements like T&R. However, the continuity equation for electrons ensures that under steady state conditions:

$$G = R = \frac{(n - n_0)}{t}$$  (Eq.2.5)

where R is the recombination rate for electrons, $n-n_0$ is the free electron concentration in excess to dark conditions, and $\tau$ is the free electron lifetime. Since the photoconductivity can be defined as:

$$s_{PH} = q\mu(n - n_0) \qquad \text{(Eq.2.6)}$$

where $\mu$ is the mobility of the electrons in extended states, it can be obtained that:

$$G = \frac{s_{PH}}{q\mu t} \qquad \text{(Eq.2.7)}$$

From this equation, it can be inferred that constant generation rate requirement of CPM depends on the condition that lifetime of electron, $\tau$, should be constant.

Eq.2.4 shows that the steady state concentration of photoexcited electrons can be kept constant during the change of photon energy by changing the light intensity. Hence, during the CPM measurement, incident flux of exciting light is adjusted at each energy to maintain photocurrent constant. The inverse of the incident flux values is plotted versus photon energy. This spectrum is normalized to the absolute scale by matching the values of T& R at about $\alpha = 1000$ cm$^{-1}$.

Unlike PDS, this method is only sensitive to electrons that are excited to the conduction band. In other words, only transitions I, II, IV shown in Figure 2.3 are detected. These are excitations from valence band, valence band tail states and localized states (midgap states) to the conduction band, contributing to the photocurrent. Since low generation rate of modulated light is used in CPM, only the occupied gap states below the dark Fermi level can be observed. This implies that the gap states at the upper part of the bandgap do not respond to the CPM measurement, and the knowledge about the distributions over there cannot be obtained. Hence, photon energies in the range of 0.8 eV and those greater than the band gap of the sample can be effective in the CPM measurements for undoped a-Si:H thin films since the mobility gap of a-Si:H is between about 1.8-1.9 eV. In Figure 2.4, an example of the absorption coefficient spectra of a-Si:H thin films measured by both CPM and PDS was shown. As seen in this figure, the absorption spectra of PDS and CPM are unlike below about 1.5 eV since different transitions or different types of defects are detected. In addition, the smaller the thickness of the film, the higher optical absorption is observed in PDS measurement since surface defects become more dominant in thinner films. However, CPM is more sensitive to bulk defects in a-Si:H.

Two procedures have been developed for both PDS and CPM measurements to obtain the densities of defect states from sub-bandgap absorption spectrum. These are deconvolution of the optical spectrum and integration of the excess sub-bandgap absorption. In the former procedure, the absorption coefficient $\alpha(h\nu)$ as a function of photon energy is related to the convolution between the densities of occupied initial and unoccupied final states and can be described as in Eq.2.1 [55,58,59]. This procedure requires some assumptions and knowledge of the density of states. The spectral dependence of the index of refraction (in the range of 0.8 eV-2.0 eV) is neglected. It also assumes parabolic bands and a free electron density value, a Gaussian distribution of deep defects and exponential band tails. The position, height, and width of this Gaussian distribution are fitted to the experimental data.

In the second procedure, integration of the excess sub-bandgap absorption is used to estimate the density of midgap states [52,60,61]. It is due to contribution of deep defects to the absorption up to the Urbach energy. If the sub-bandgap absorption were due to dangling bonds, a correlation between the magnitude of the absorption and the number of dangling bonds would be expected. In other words, there must be an underlying assumption for this procedure. The excess absorption $\Delta\alpha$ due to sub-bandgap states can be found by deducting the exponential absorption tail from the measured absorption spectrum. $\Delta\alpha(E) = \alpha - \alpha_{exp}$. The density of states in terms of excess absorption is:

$$N = C \int_{E_1}^{E_2} ?a(E)dE \qquad \text{(Eq.2.8)}$$

In this equation, C is a constant determined by the index of refraction of the material, electron mass and charge, speed of light etc. Jackson and Amer [52] assumed that excess absorption in the PDS spectrum is proportional to the ESR-determined neutral dangling bond ($D^0$) density, and found the constant $C = 7.9\times10^{15}$ cm$^{-2}$ eV$^{-1}$. Similar constant for the CPM was found to be $(1.9\pm0.3)\times10^{16}$ cm$^{-2}$ eV$^{-1}$ by Wronski et al. [60] and again the ESR calibrated data was taken into account. The comparison of these two techniques using integrated excess absorption showed that the PDS detects much higher absorption for the same defect density due to additional surface defects [60]. Although integrated excess absorption is useful technique, the contribution of the

charged dangling bonds is not taken into account. A proper constant depends on the accuracy of ESR measurements as well. In addition, appropriate choice of the initial and final energies is required since exponential tails and midgap defect distribution generally overlap [61]. Wyrsch et al. used another approach, absorption coefficient at a single energy, for both CPM and PDS [62]. For $\alpha_{CPM}$ (1.2 eV) = 1 cm$^{-1}$ or $\alpha_{PDS}$ (1.2 eV)=2 cm$^{-1}$, their calculation suggests that dangling bond density is in the range from 2.4x10$^{16}$ to 5x10$^{16}$ when light soaked state is investigated.

## 2.4 Dual Beam Photoconductivity Method

The dual beam photoconductivity (DBP) technique is based on measuring the photoconductivity of the sample while the energy of monochromatic light changes. It has similar principles with CPM. However, the assumptions necessary to obtain $\alpha(h\nu)$ from $\sigma_{PH}$ spectrum are treated in a different way in the DBP method. These assumptions can be summarized as follows. 1) The averaged $\mu\tau$ product is not altered by the monochromatic beam. In the DBP technique, $\mu\tau$ product is fixed to be a constant using the high intensity bias light. 2) The multiple reflections in the air-film-substrate structure are neglected. 3) R(t,E) and $\eta$(E) are assumed to be constants of energy. 4) $\alpha(h\nu)$t product is much smaller than unity. These assumptions are crucial points of the DBP method and must be satisfied to obtain reliable absorption coefficient spectrum.

Dual Beam Photoconductivity (DBP) technique [50,54-57] uses two light beams, and it has almost the same physical principal as the CPM technique to obtain absorption spectrum from the energy dependence of photoconductivity.  The idea of DBP is to maintain the free carrier lifetime constant by using the high generation rate dc bias light. This implies that dc bias light keeps the electron and hole quasi-Fermi levels constant during the measurement. A second light beam is monochromatic and modulated with a certain frequency. Modulated light beam has a very low generation rate than the dc bias light so that the quasi-Fermi levels are not altered by the ac light beam. For this reason, a.c. $\sigma_{PH}$ depends on the bias light intensity linearly, meaning no change in the mobility lifetime product of dc light. Therefore, the distribution of the occupied defect states will be unchanged in the mobility gap during the measurement. Then, the monochromatic a.c. light excites the electrons from the occupied localized defects to the conduction band. Those electrons in the conduction band are detected as photocurrent when energy

of the monochromatic light is changed. As a result, the effects of occupied localized defect states will be measured as photoconductivity. Since $\alpha t$ product is much smaller than unity in the sub-bandgap region as mentioned before, the DBP yield spectrum (photoconductivity divided by the incident flux) is directly related to the absorption coefficient spectrum of the film at energies below the bandgap.

The DBP yield spectrum is actually a direct measurement of the energy dependence of the generation rate. The generation rate can be expanded in terms of generation efficiency $\eta(E)$, which is defined as the number of delocalized electrons per absorbed photons, the incident photon flux $F(E)$, the absorbance where $[A(t,E) = 1-R(t,E)-T(t,E)]$ and the film thickness t;

$$G = \frac{?(E) \ F(E) \ A(t, E)}{t} \qquad \text{(Eq.2.9)}$$

Therefore, the effective absorbance $\eta(E)A(t,E)$, which is the portion of the absorbance contributing to photoconductivity, can be determined using a calibrated light source with a known flux. Hence, the DBP yield spectrum can also be viewed as the effective absorbance spectrum by using the following derivations.

The photoconductivity is defined as:

$$s_{PH} = q \, \mu_e n + q \, \mu_h p \qquad \text{(Eq.2.10)}$$

where $\mu_e$ and $\mu_h$ are the mobility of electrons and holes, and n and p are the number of free electrons and holes per cm$^3$, respectively. Since the mobility-lifetime product of holes is negligible compared to that of electrons, the contribution of hole transport to photoconductivity is insignificant. As a result, since the number of electrons equals to product of lifetime ($\tau$) and generation rate, the sub-bandgap photoconductivity arising from the monochromatic beam as a function of generation rate can be written as:

$$s_{PH}(a.c.) = q \, \mu \, t \, G \qquad \text{(Eq.2.11)}$$

By using the Eq.2.9, the photoconductivity can be written in terms of absorbance:

$$s_{PH}(a.c.) = \left[\frac{q\,\mu\,t\,F(E)}{t}\right]?(E)\,A(t,E) \qquad (Eq.2.12)$$

Since the normalized photoconductivity yield is obtained by dividing photoconductivity to incident flux:

$$Y_{DBP}(E) = \frac{s_{PH}(E)}{F(E)} = \left[\frac{q\,\mu\,t}{t}\right]?(E)\,A(t,E) \qquad (Eq.2.13)$$

Therefore, by using the Eq.2.12 and Eq.2.13, the effective absorbance can be written as:

$$A_{eff}(t,E) = ?(E)A(t,E) = \left(\frac{t}{q\,\mu\,t}\right)Y_{DBP}(E) \qquad (Eq.2.14)$$

Neither PDS and CPM nor DBP technique does actually provide an absolute spectrum. The absolute absorption coefficient $\alpha(E)$ is acquired by matching the yield spectrum $Y_{DBP}(E)$ with the optical absorption spectrum $\alpha_{TR}(E)$ obtained from the transmission and reflection measurement (T&R). If the multiple reflections in the air-film-substrate structure, which lead to the interference fringes in the yield spectrum, are neglected (by averaging the spectrum using FFT technique or other methods), the optical absorbance $A(t,E)$ is approximated by

$$A(t,E) \propto \left(1 - R(t,E)\right)\left[1 - \exp(-a(E)t)\right] \qquad (Eq.2.15)$$

In the sub-bandgap region, the product of the absorption coefficient and the film thickness, $\alpha(E)t$, is much smaller than unity. Since approximating [1-exp(-$\alpha$(h$\nu$)t)] by $\alpha$(h$\nu$)t outcome less than 5% error if $\alpha(E)t < 0.1$, this can be acceptable as an experimental error. As the typical a-Si:H film thickness is around 1 $\mu$m, this implies that

$\alpha(h\nu)$ must be smaller than $10^3$ cm$^{-1}$, which is the value where the photon energy is close to the bandgap energy. Therefore, this assumption can be used in the sub-bandgap region of the absorption spectrum. If it is further assumed that the generation efficiency $\eta(E)$ and the reflectance $R(t,E)$ are constants of energy, the yield $Y_{DBP}(E)$ can be approximated to $\alpha(h\nu)$. By using these assumptions, and Eq.2.14 and Eq.2.15:

$$A(t, E) \propto (1 - R(t)) t\, a(E) = C_1\, a(E) \qquad \text{(Eq.2.16)}$$

$$Y_{DBP} = ?\, A(t, E) \left[ \frac{q\,\mu\,t}{t} \right] = C_2\, A(t, E) = C\, a(E) \qquad \text{(Eq.2.17)}$$

where $C_1$, $C_2$ and $C$ are constants. Consequently, the optical absorption coefficient $\alpha(E)$ can be obtained by multiplying the yield by a constant $C$. The constant can be determined by matching $Y_{DBP}(E)$ to $\alpha_{TR}(E)$.

In the DBP, generation rate of the bias light is varied to change the electron and hole quasi-Fermi levels. Then, number of the electron occupied localized states in the bandgap will be increased by the increase of the generation rate of dc bias light. Therefore, this will lead to the increasing of electron excitations from occupied localized states in to the conduction band, and thus an increased absorption coefficient at lower photon energies. This is called intensity dependence of the sub-bandgap absorption in DBP spectrum. This feature is not present in CPM technique. It serves as an advantage over CPM technique. It gives additional information about the density, distribution and the nature of the localized defect states in the bandgap of the film. For low photon energies, $\alpha(h\nu)$ depends on the quality of the film, generation rate (G), photoconductivity ($\sigma_{PH}$), and non-integer power of G, $\gamma$ ($\sigma_{PH} \approx G^{\gamma}$). When electron and hole quasi-Fermi level move apart, they allow more gap states to act as recombination centers and their occupancy is reflected in $\sigma_{PH}$ and $\alpha(h\nu)$. Therefore, states above the Fermi level to be occupied by electrons lead to more electron transitions to conduction band. In CPM, only the occupied localized defects below the dark Fermi level are detected due to very low generation rates used in the measurement. However, in DBP, by using different generation rates of dc bias light, occupied localized defects both below and above the Fermi level can be probed.

Even though reliable absorption coefficient spectra are obtained by DBP using different bias light intensities, it is not straightforward to obtain information about defect states from the measured spectra. Absorption coefficient reflects somehow the contribution of defect states at lower energies but it requires a reliable calibration constant under some certain assumptions. Absorption coefficient at a single energy [62-64] is a convenient way for DBP to estimate the density of states in the bandgap but it needs a proper choice of reference energy point. The reference energy is dependent on the Fermi level position and is chosen arbitrarily. It is generally taken as 1.2 eV for a-Si:H [64]. It also requires a consistent calibration constant for both the native and light induced defect states. In this procedure, the absorption coefficient is linked with the deep defect density at a reference energy in the following manner

$$N_{DOS} = C\ \alpha(1.2\ eV) \qquad\qquad (Eq.2.18)$$

where C is a weakly energy dependent constant. The calibration constant comes from the ESR measurement [65]. The assumption is that both the ESR signal and sub-band gap absorption below 1.4 eV come from the same type of defect states, namely singly occupied neutral silicon dangling bonds ($D^0$). There are experimental difficulties in obtaining this calibration constant since the ESR measurements for about 1 $\mu$m films cannot give reliable calibration factors in the annealed state due to surface defects. Therefore, this calibration constant was obtained in the saturated light soaked state. Since light induced bulk defect states become much higher than surface states [62], ESR measurements can only be used to obtain calibration factors for the light degraded films. However, more reliable and quantitative information about the midgap states involve more detailed physics, and numerical simulations with prior knowledge about the defect states are required [57,65]. In this thesis study, the DBP technique was established to measure the absorption coefficient spectra for amorphous semiconductors. Experimental setup, calibration, and automation of the DBP technique are explained in detail in the following chapter.

## 2.5 Other characterization techniques

### 2.5.1 Steady State Photoconductivity

In general, steady state photoconductivity [49,50] exhibits a non-integer power-law dependence on light intensity F or generation rate G:

$$s_{PH} = C G^g \quad (O\text{-}cm)^{-1} \tag{Eq.2.19}$$

Therefore, from Eq.2.11 mobility-lifetime product can be written as:

$$\mu t \propto G^{(?-1)} \quad \left(cm^2 V^{-1}\right) \tag{Eq.2.20}$$

where C is a proportionality constant, and $0.5 = \gamma = 1.0$. $\gamma = 0.5$ represents bimolecular recombination kinetics, where electrons in the conduction band directly recombine with the holes in the valence band as in crystalline silicon. $0.5 < \gamma = 1.0$ represents that electrons in the conduction band recombine with holes in the valence band through the recombination centers in the bandgap. This process is called monomolecular recombination. Amorphous silicon materials exhibit monomolecular transport mechanism. The dependence of photoconductivity on generation rate can be deduced using the following expressions. Bimolecular recombination is related to intrinsic photoconductivity since it involves only electrons and holes in the conduction and valence bands. If the system is in equilibrium, the change in the carrier concentrations of electrons (n) and holes (p) are equal and given by the difference between generation (G) and recombination (R) rates.

$$\frac{dn}{dt} = \frac{dp}{dt} = G - R = G - R_C np \tag{Eq.2.21}$$

where $R_c$ is the recombination coefficient. At steady state, dn/dt =dp/dt = 0 and:

$$n = p = \sqrt{\frac{G}{R_C}} \tag{Eq.2.22}$$

Since $\sigma_{PH} = qn(\mu_e + \mu_h)$ from Eq.2.10, photoconductivity as a function of the generation rate can be written as:

$$s_{PH} = \left(\frac{q(\mu_e + \mu_p)}{\sqrt{R_C}}\right)G^{1/2} \propto CG^g \qquad \text{(Eq.2.23)}$$

This equation indicates that the intensity depends on photoconductivity and $\gamma$ must be 0.5 for bimolecular recombination process.

Unlike bimolecular process, monomolecular process involves defect levels in the bandgap and it is directly related to extrinsic photoconductivity. However, the carrier density follows the same bimolecular relationship

$$\frac{dn}{dt} = \frac{dp_A}{dt} = G - Cnp_A \qquad \text{(Eq.2.24)}$$

where $p_A$ is the density of holes in defect levels and C is a constant. In steady state, all time derivatives vanish. If defect levels are assumed to be completely filled ($n_i = N_i$) where $N_i$ is the density of defect levels and $n_i$ is the occupied levels of $N_i$ by electrons, the electron concentration using the quasi-neutrality condition ($n + n_i = p_A$) can be written as

$$n = \frac{1}{2}\left[-N_i + \sqrt{N_i^2 + 4\frac{G}{C}}\right] \qquad \text{(Eq.2.25)}$$

for small generation rate values, i.e., $G \ll N_i^2 C / 4$, this equation reduces to

$$n = \frac{G}{CN_i} \qquad \text{(Eq.2.26)}$$

Since $\sigma_{PH} = q n \mu_e$ from Eq.2.10 for negligible hole transport, photoconductivity as a function of the generation rate can be written as:

$$s_{PH} = \left(\frac{q\mu_e}{CN_i}\right)G = AG^g \qquad \text{(Eq.2.27)}$$

This equation indicates that the intensity also depends on photoconductivity for extrinsic case and $\gamma$ must be unity for monomolecular recombination process.

Steady state photoconductivity measurements give information about the nature of defects, mobility-lifetime product, and transport and recombination kinetics of photogenerated carriers as described above. The non-integer power law dependence on light intensity is a consequence of the continuous distribution of gap states. Since the states between quasi-Fermi levels act predominately as recombination centers, steady state photoconductivity is sensitive to both density and nature of these states. In this thesis, the following expressions were used to calculate flux, photoconductivity, mobility-lifetime product, and generation rate values. Experimental results were also used to obtain non-integer power ($\gamma$) values of amorphous semiconductor thin films.

For a p-i-n photodiode, flux is calculated by:

$$F(h\nu) = \frac{I_{PH}(h\nu)}{A\eta(h\nu)q} \qquad (cm^{-2}s^{-1}) \qquad \text{(Eq.2.28)}$$

where $I_{PH}(h\nu)$ is the measured photocurrent using p-i-n photodiode at photon energy $h\nu$, A is the detector area, $\eta(h\nu)$ is the quantum efficiency at energy $h\nu$ of monochromatic light, and q is the electron charge. The photoconductivity can be easily derived from the Ohm's law. If J is the current density and E is the electric field:

$$J = s_{PH} E \qquad \text{(Eq.2.29)}$$

$$\frac{I_{PH}}{t\,l} = s_{PH}\frac{V}{d} \qquad \text{(Eq.2.30)}$$

Therefore, for samples in coplanar geometry, the photoconductivity is:

$$s_{PH} = \frac{I_{PH}\,d}{V\,t\,l} \quad (\Omega\text{-cm})^{-1} \tag{Eq.2.31}$$

where d is the separation between the electrodes, l is the length of the electrodes, t is the thickness of the film, and V is the applied voltage. If the photoconductivity is known, the mobility-time product, $\mu\tau$, which is one of the most important parameters for photosensitive devices, can be obtained from Eq.2.11:

$$\mu\,t = \frac{s_{PH}}{q\,G} \quad (cm^2 V^{-1}) \tag{Eq.2.32}$$

Volume generation rate, G, can be calculated from the incident flux, thickness, absorption coefficient, and the reflectivity of the material investigated:

$$G = \frac{F(1-R)[1-\exp(a\,t)]}{t} \quad \left(cm^{-3}s^{-1}\right) \tag{Eq.2.33}$$

where F is the incident flux in $(cm^{-2}s^{-1})$, $\alpha$ is the absorption coefficient at applied monochromatic light energy, R is the reflectivity of the material.

A homemade steel box and an Osram 250 W ENH white lamp cooled by a fan were used for steady state photoconductivity measurements. The measurement system is shown in Figure 2.5. 800, 750, 690 nm interference filters and RG-610 bandpass filter were used to convert white light to monochromatic light to generate free carriers. Monochromatic light intensity was adjusted to lower flux values by using neutral density filters, which transmit 0.1%, 1%, 10% and 50% of incoming light. Constant voltage was applied to the samples, and current was measured in the Ohmic regime by using Keitley 6517A Electrometer. Indium flakes were used on the contacts to improve ohmic behavior of the films. A p-i-n photodiode, which has 14.5 mm$^2$ active area, was used to calibrate the incident white light for respective photon energies.
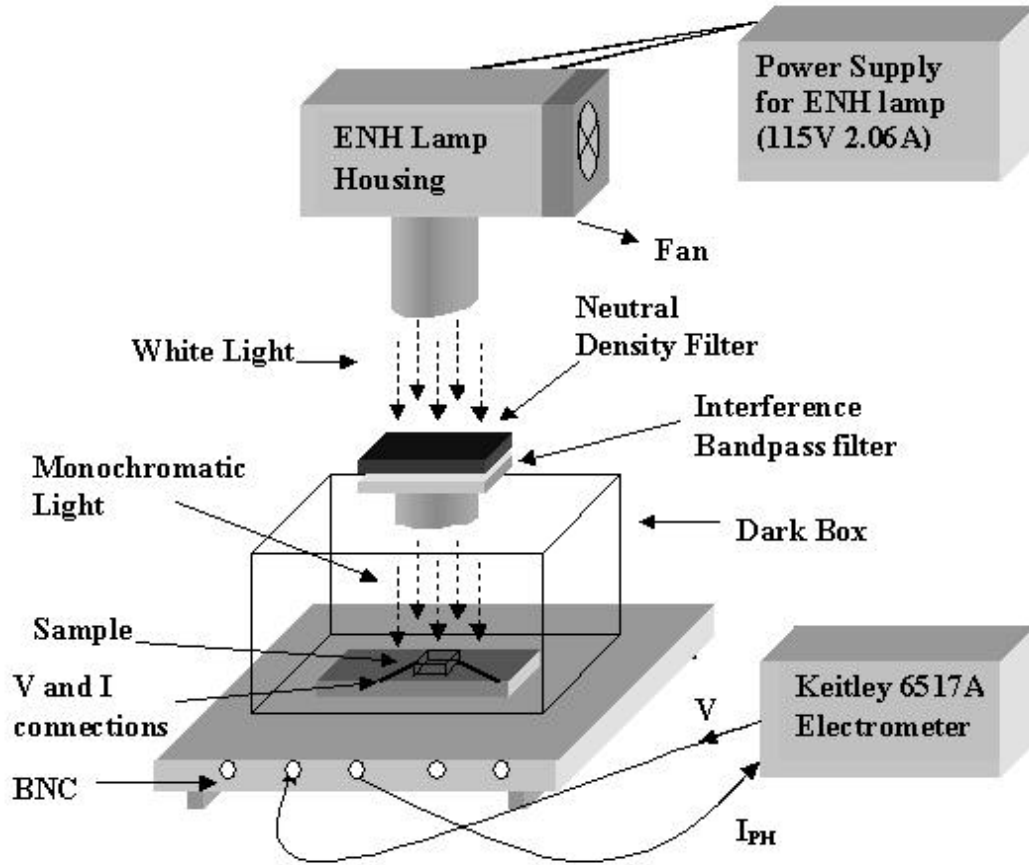
Figure 2.5.     The steady state photoconductivity measurement system.

## 2.5.2 Dark Conductivity Measurement

Temperature dependent dark conductivity of thin films is an important characterization tool to determine the position of dark Fermi level from the conduction band mobility edge. This energy difference is called the activation energy for the electrons. The activation energy is an important physical parameter of the film since the position of the dark Fermi level is highly sensitive to the presence of impurities, defects, and dopants and it determines the occupation of gap states.

For a semiconductor, the dark conductivity, $\sigma_D$, is given as:

$$s_D = s_0 \exp\left(\frac{-(E_C - E_F)}{kT}\right) = s_0 \exp\left(\frac{-E_A}{kT}\right) \qquad \text{(Eq.2.34)}$$

where $E_C$ is the conduction band energy, $E_F$ is the Fermi level, $E_A$ is the activation energy, k is Boltzmann's constant, and $\sigma_0$ is the constant that is determined from the intercept on $\log \sigma_D$ axis. If the logarithm of Eq.2.35 is taken:

$$\text{In} s_D = \text{In} s_0 - \left(\frac{E_A}{kT}\right) \qquad \text{(Eq.2.35)}$$

$$\text{In} s_D = \text{In} s_0 - \left(\frac{E_A}{1000k}\right)\left(\frac{1000}{T}\right) \qquad \text{(Eq.2.36)}$$

Therefore, the activation energy $E_A$ can be obtained from the slope of $\text{In}\sigma_D$ versus 1000/T graph, which is the Arrhenius plot.

In this thesis, the films used for the steady state conductivity and sub-bandgap absorption are also characterized by the temperature dependent dark conductivity technique to understand the quality of the samples. For this purpose, a system shown in Figure 2.6 was established in our laboratory. The dark conductivity measurements were performed in a steel vacuum box, which was manufactured at IZTECH, having pressure about 0.2-0.3 Torr measured by a Leybold vacuum gauge. The same system was used to anneal the thin films by keeping them in a vacuum for a few hours at about 150 $^{\circ}$C. Temperature was measured by using Omega CL8500 meter with a K-type thermocouple connected to an identical substrate on a copper base (Figure 2.7) heated by a 40 W heater. Current was measured in the Ohmic regime by using Keitley 6517A Electrometer. The slope of the Arrhenius plot of dark conductivity resulted in the activation energy of the films.
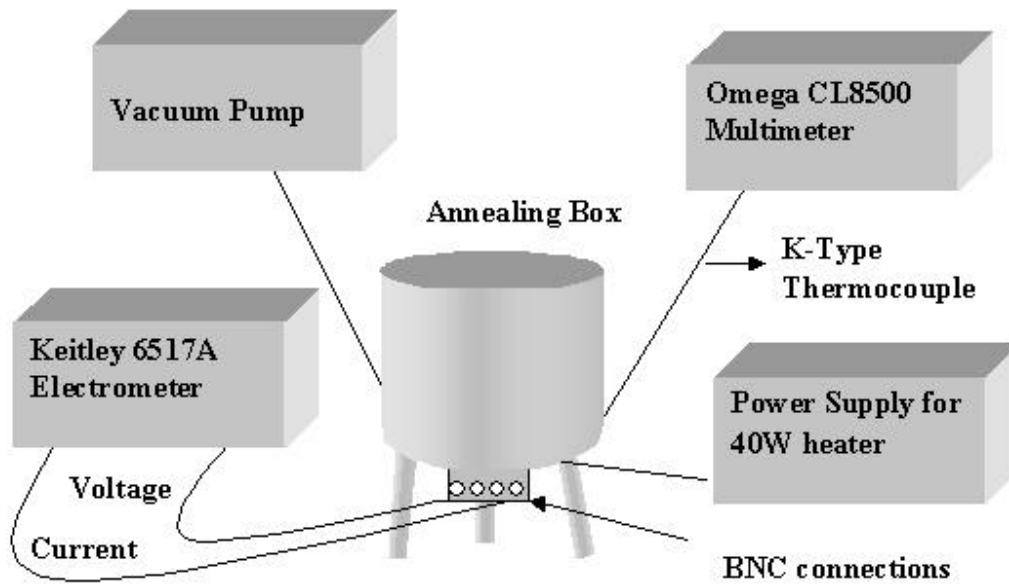
Figure 2.6.    The system used to measure activation energy and to anneal the sample s.
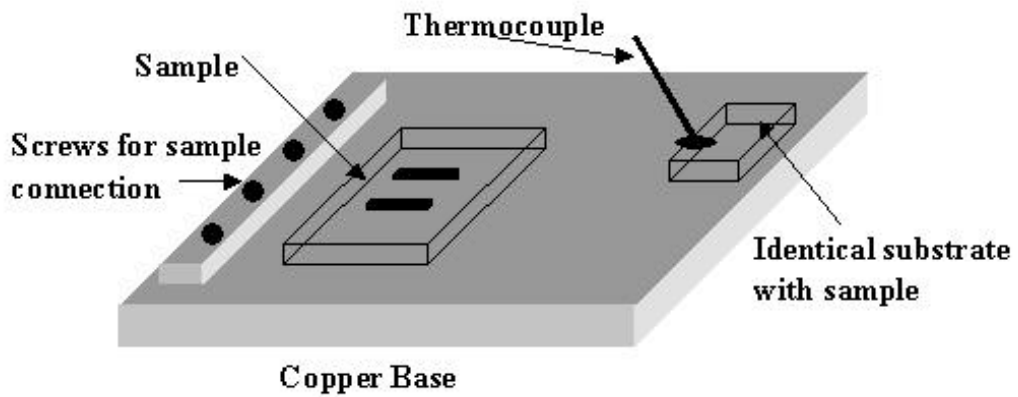


Figure 2.7.    Copper Base inside the annealing box

# CHAPTER 3

## DUAL BEAM PHOTOCONDUCTIVITY SPECTROSCOPY

### 3.1. Introduction

Dual beam photoconductivity (DBP) technique is one of the sub-bandgap absorption spectroscopy techniques used to characterize amorphous semiconductors. The physical principles and the assumptions necessary to measure the sub-bandgap absorption coefficient was explained in detail in the previous chapter. In this chapter, the system design and calibration of DBP method is going to be presented in detail.

### 3.2. System Design

The Dual beam photoconductivity system used to obtain sub-bandgap absorption spectrum is shown in Figure 3.1. An Oriel model 66182 lamp housing was used as a white light source. 300 W Radiometric power supply was used to control Quartz Tungsten Halogen (QTH) lamps in the lamp housing. All optical elements were aligned on a small optical table with rails designed and manufactured at IZTECH. A chopper blade was mounted on the table near the lamp housing to chop the white light so that the light behaves as an a.c. light. In general, 13 Hz was used as chopping frequency for the measurements. Frequency of the chopper blade was controlled by a chopper controller, which has ±1 Hz sensitivity. The chopper controller is connected to lock-in amplifier to determine the reference frequency of the measurements. An Oriel monochromator having 0.2 nm sensitivity was used to convert white light to desired wavelengths by using a 600-lines/mm grating. Monochromator crank was controlled by using an Oriel monochromator driver. At the other end of the monochromator, a filter driver, which includes three long pass filters with wavelength of 500 nm, 700 nm, 900 nm and single crystalline silicon with wavelength of 1100 nm, was placed to cut-off unwanted second and higher order wavelengths.
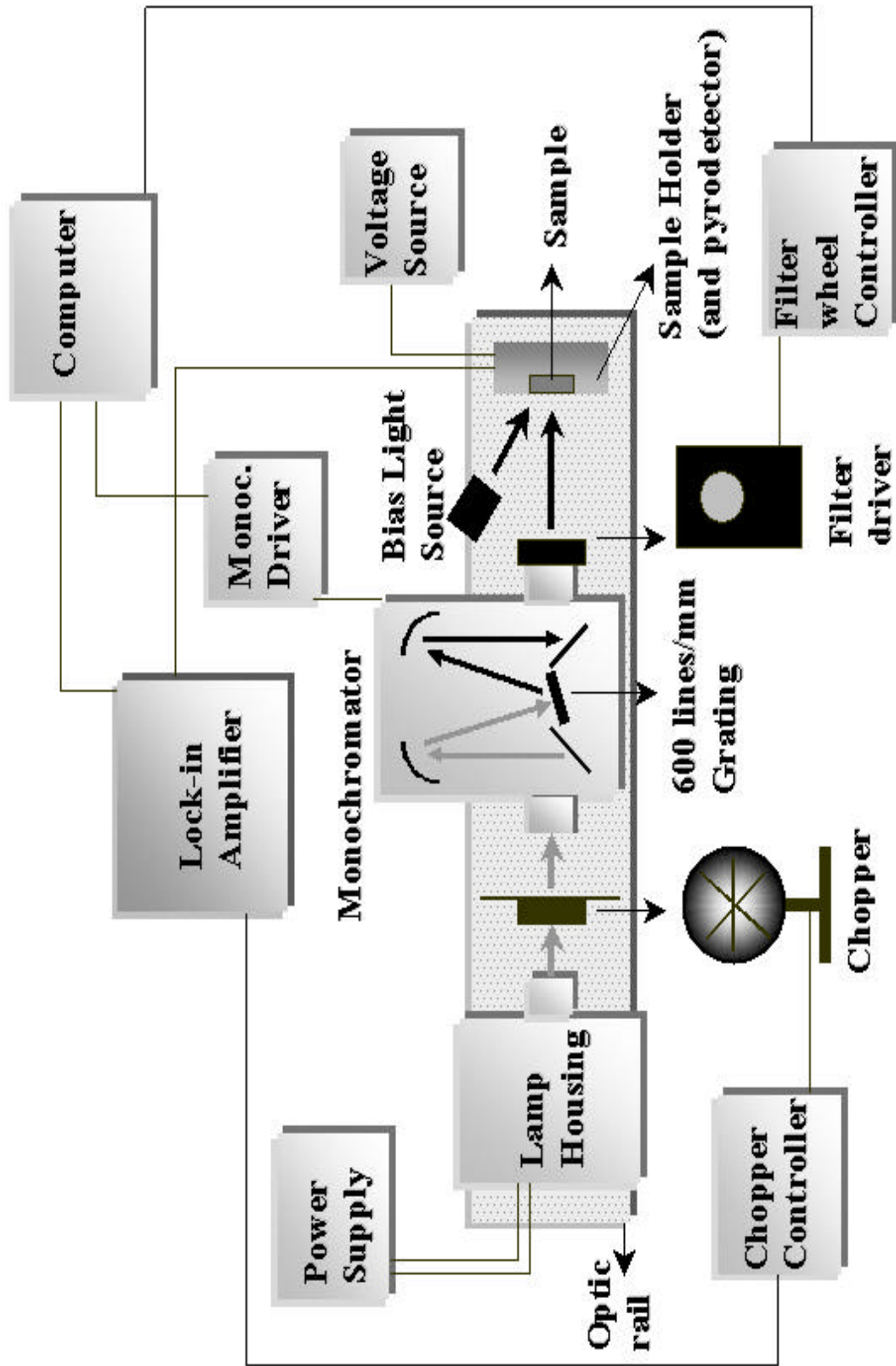
Figure 3.1 Dual beam photoconductivity system used to measure sub-bandgap absorption and transmission in a-Si:H based materials.

An Oriel filter driver controller was used to change filter. A homemade sample holder, shown in Figure 3.2, was designed with BNC connections to hold the samples and pyroelectric detector to perform the measurements. Monochromatic light after the filter drive shines either on the sample or on the detector. Pyroelectric detector or Silicon and InGaAs p-i-n type photodetectors are used to calibrate the flux spectrum of the white light source. Keitley 6517A Electrometer was used to apply external d.c. bias voltage to the sample and to measure current due to bias light. A.c. signals coming from the sample and detectors were detected by SR830 lock-in amplifier. All system excluding measurement devices was placed in a closed box to stimulate a dark room to prevent unwanted signals due to other light sources. A computer program has been developed as a part of this thesis to control the whole system with a computer as explained below.

## 3.3. Software

The computer program used to control the DBP system was written by using Objectbench software. Keitley IEEE 488 card was used to provide General Purpose Interface Bus (GPIB) protocol. The program controls the drivers of monochromator and filter, and lock-in amplifier, which are connected to IEEE 488 card. After initializing the devices and sample or any detector, the program is started to obtain photocurrent (for DBP and p-i-n detectors) or voltage (for the pyroelectric detector, transmission) data itself. In the program, some parameters such as the number of measurement, initial energy and energy step can be adjusted before the program is started. The desired wavelength or energy values of the monochromator are adjusted by the program. At each energy, raw current or voltage data and phase of the signal are measured by lock-in amplifier in both the flux and DBP measurement and then the data averages are written to the data file. In DBP and transmission measurements, photocurrent or voltage data are divided by the corresponding flux data to normalize the spectrum as mentioned before. The bandpass filters are changed at certain energy values by the program. After the measurements, the data files are processed using a graphics program to obtain true $\alpha(h\nu)$ spectra. The normalized photocurrent spectra are normalized to absolute absorption coefficient values obtained from T&R or PDS data. The computer program of the system is given in appendix.
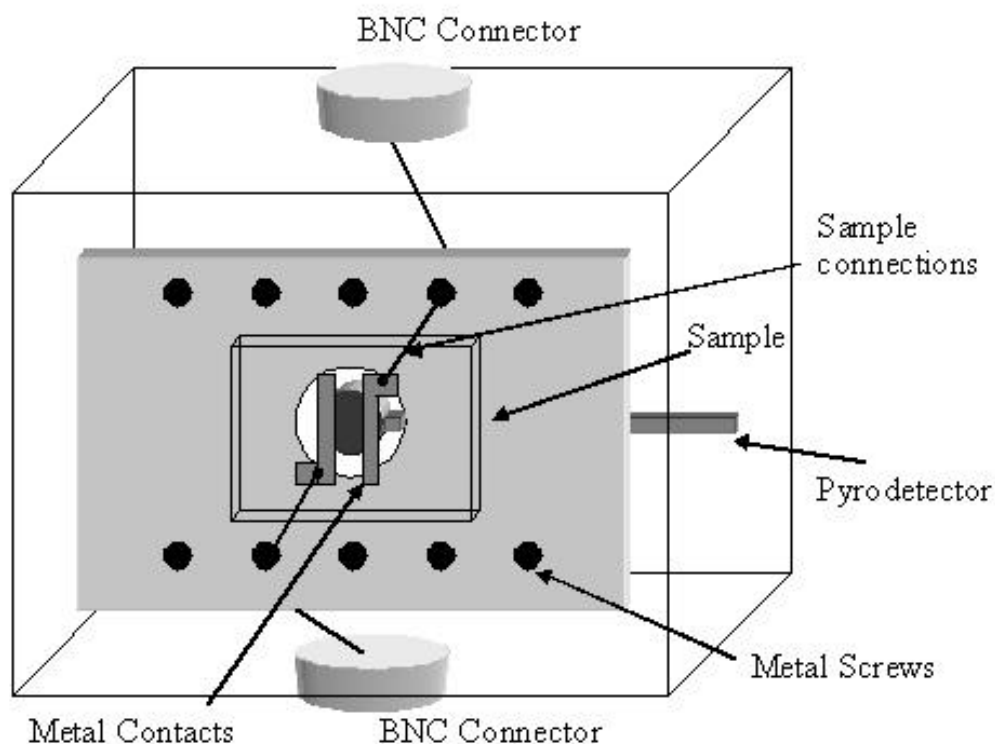
Figure 3.2    The sample holder used in dual beam photoconductivity and flux calibration measurements.

## 3.4. Flux Calibration

A Quartz Tungsten Halogen lamp (QTH) is used as a white light source in the DBP system. It does not have a flat flux spectrum, i.e. flux depends on the photon energy. Therefore, flux calibration is necessary and it is a crucial step to perform the DBP measurement. The energy dependence of flux is used to normalize raw current and transmission data of the samples. Flux calibration was carried out using a pyroelectric detector and two p-i-n type photodiodes. Both Silicon and InGaAs p-i-n photodiodes are used together to cover the energy range approximately from 2.1 eV to 0.8 eV. The same flux calibration in energy range from about 0.6 eV to 2.5 eV was achieved using a single pyroelectric detector. These are explained in detail in the following sections.

### 3.4.1 Flux Spectrum Calibration by Pyroelectric Detector

A pyroelectric material has electric polarization even in the absence of an applied voltage. The materials are usually crystalline. Pyroelectric detectors are thermal type infrared detectors that feature stable operation at room temperature and responsivity independent of wavelength. The schematic illustration and the circuit of pyroelectric detector are shown in Figure 3.3. When light enters the element such as $CaF_2$ and is absorbed, the element temperature increases, resulting in a change in the state of spontaneous polarization. These changes are detected as a voltage change. Since the pyroelectric detector detects light only when a temperature change in the element occurs, it is necessary to use an optical chopper and lock-in amplifier to receive data. The advantage of the pyroelectric detector over Si and InGaAs detectors is that it is sensitive to a wide range (0.1 μm-100 μm) of the optical spectrum. Moreover, since pyroelectric detector has a constant quantum efficiency, which was accepted as unity, the normalization procedure was not applied. However, this is a necessary step in the case of p-i-n photodiodes. The raw measurements were used as relative flux data. Pyroelectric detector was also used in transmission measurements by mounting it to the sample holder just behind the sample. As in DBP measurements, transmission measurements require normalization by dividing the voltage-photon energy ratio to flux since voltage should be detected by lock-in amplifier when pyroelectric detector is used.
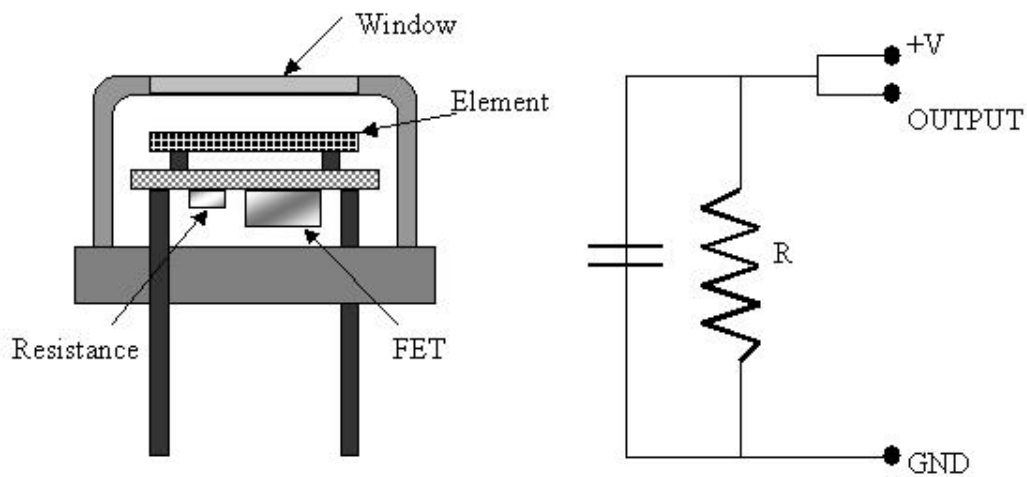


Figure 3.3.    Schematic illustration of Pyroelectric detector and its circuit

### 3.4.2 Flux Spectrum calibration by Silicon and InGaAs detectors

When a p-i-n photodiode is operated under a reverse bias of a few volts or is shorted, the diode carries a reverse current $I = -( I_S + I_L )$, where $I_S$ is the saturation current and $I_L$ is the light generated current. The diode operated in this mode acts as a photodiode and can be used to measure the light intensity. Figure 3.4 shows the I-V characteristics of a p-i-n photodiode for different generation rates.
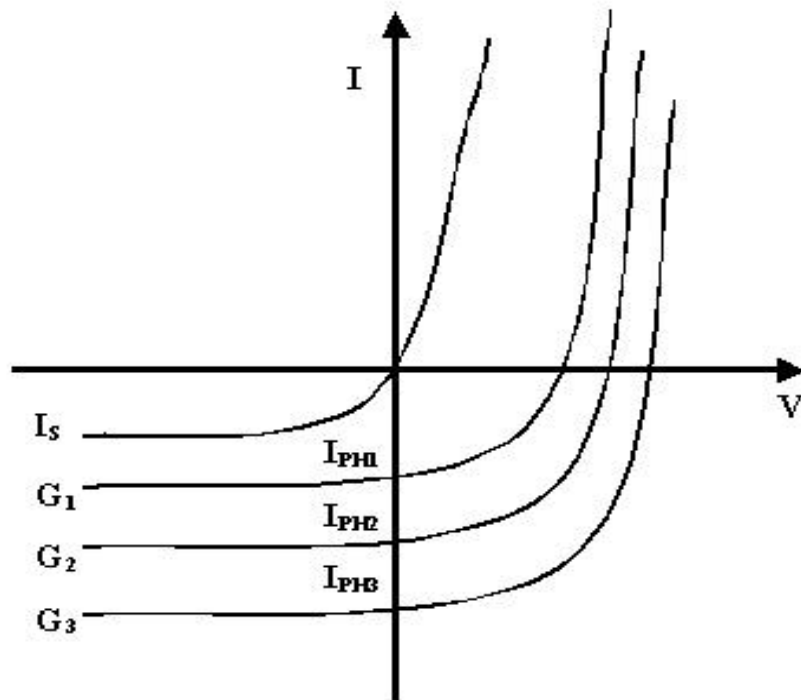


Figure 3.4.     I-V characteristics of p-i-n detectors

When the generation rate of light increases, the resulting short circuit current also increases. Therefore, operation of p-i-n photodiode under the short circuit or under reverse biased case can be used to obtain flux spectrum of white light even for different generation rates. The following equation is used to calculate the flux where $I_{PH}(\lambda)$ is short circuit current at wavelength $\lambda$, A is the area of the p-i-n photodiode, QE is the quantum efficiency of p-i-n photodiode at each wavelength $\lambda$, and q is the charge of electron.

$$\text{Flux}(\text{cm}^{-2}\text{s}^{-1}) = \frac{I_{PH}(\lambda)}{AqQE(\lambda)} \qquad \text{(Eq. 3.1)}$$

QE spectra of Si and InGaAs photodiodes are not identical due to difference in the bandgap of semiconductors. The QE spectra for both photodiodes are shown in Figure 3.5. It is essential to have accurate QE spectrum to obtain reliable flux spectrum. In flux calibration, measured photocurrent at each wavelength is divided into corresponding quantum efficiencies to obtain relative flux as explained in Eq. 3.1. In this equation, only measured current and quantum efficiency values depend on photon energy. Since Si detector responds for the region approximately between 600 nm and 1000 nm (2.06 eV-1.24 eV) and the sensitivity of InGaAs detector includes the region approximately between 1000 nm and 1600 nm (1.24 eV-0.8 eV), the whole flux curve was obtained by combining two curves or normalizing the one to the other. Example of the flux spectrum for the white light source calibrated using photodiodes and pyrodetector is shown in Figure 3.6. As seen in the figure, both relative flux spectra agree quite well. These values are used to normalize the raw photocurrent spectrum of the DBP measurement. Thereby, the effect of the nonuniform flux of the white light source is eliminated.
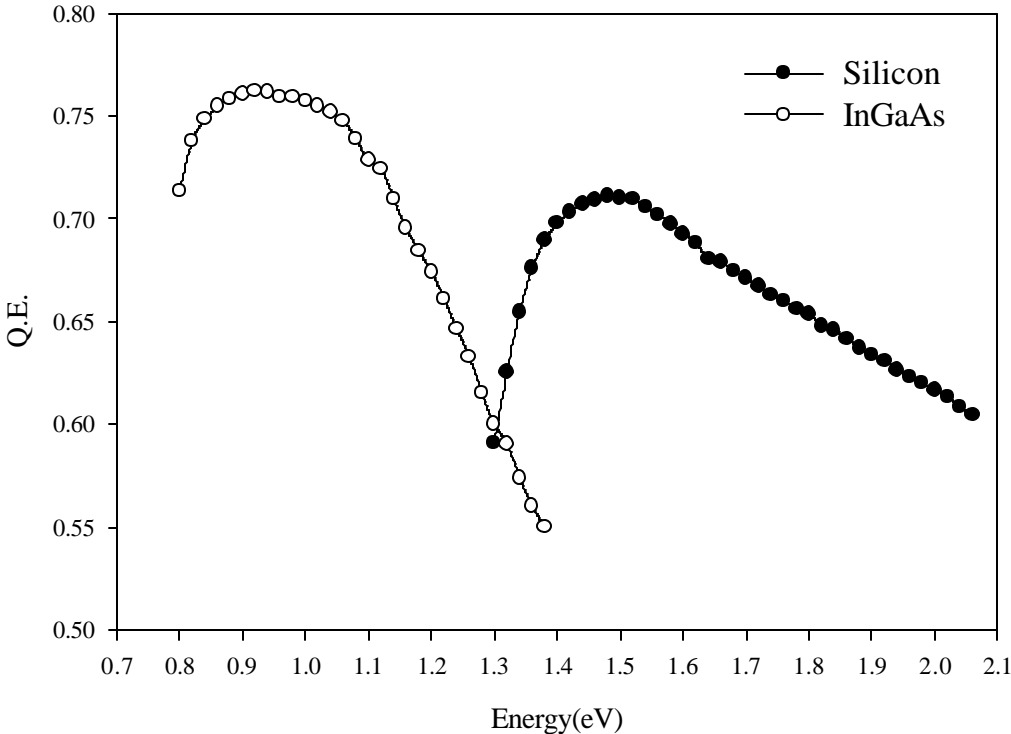


Figure 3.5.    Quantum Efficiency spectra of Silic on and InGaAs p-i-n detectors
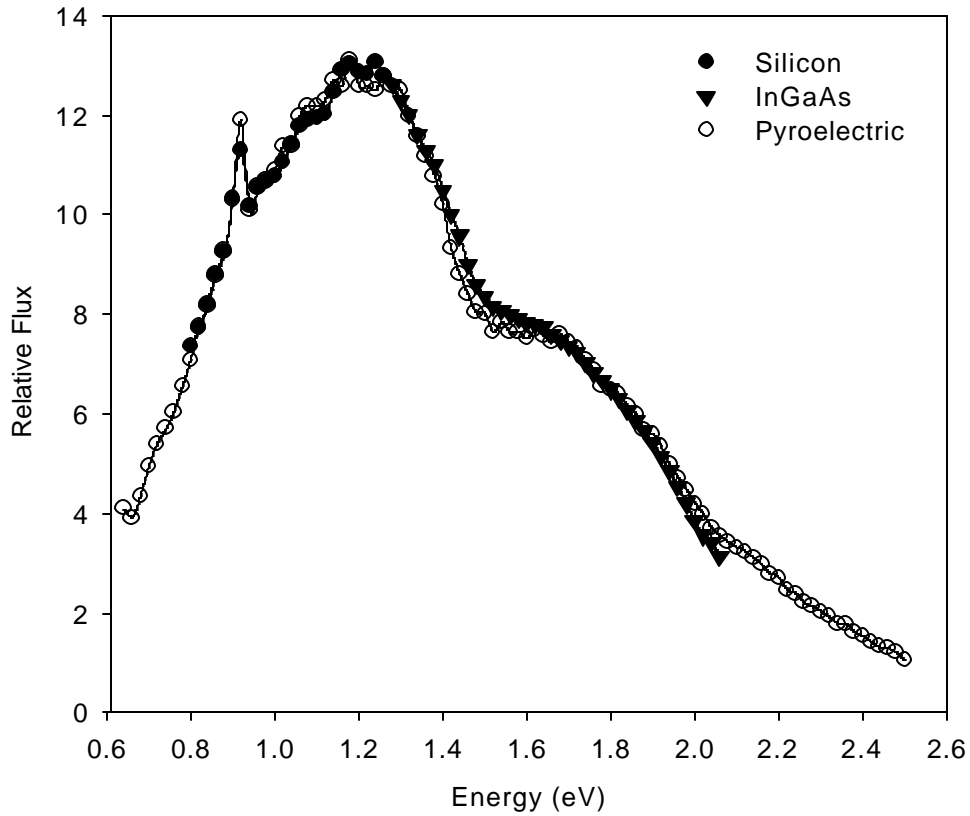
Figure 3.6.     Flux spectrum of white light obtained using Silicon and InGaAs p-i-n photodiodes and pyroelectric detector.

## 3.5. Dual Beam Photoconductivity Spectrum

Dual beam photoconductivity system does not result in an absolute absorption coefficient spectrum. It is a relative measurement. Energy dependence of the raw current spectrum is obtained by changing the energy of the incoming light on the sample. Since the incoming light does not provide a flat flux curve, the raw photocurrent is divided by the relative flux data. The resulting spectrum is called normalized photocurrent spectrum. In the Figure 3.7, a raw and a normalized photocurrent spectrum is shown for an a-Si:H sample. The shape of the spectrum is similar to the absolute absorption spectrum of a-Si:H including exponential tail state absorption down to 1.4 eV and sub-bandgap absorption shoulder below 1.4 eV. Therefore, the final goal is to convert the normalized photocurrent spectrum to the

absolute sub-bandgap absorption spectrum. In fact, it is only possible to obtain the absolute absorption coefficient values using the photocurrent spectrum if the required assumptions and conditions are satisfied in DBP method. These are explained in detail in chapter 2 when the DBP method is defined. The necessary conditions are: constant $\mu\tau$ of majority carriers, uniformly absorbed light condition, and constant R and $\eta$. In DBP system, d.c. bias light has much higher generation rate than that of a.c. monochromatic light. Therefore, quasi-Fermi levels for electrons and holes are fixed by bias light and $\mu\tau$ becomes unchanged and thus $I_{dc}/I_{ac}>>1$. The second light, i.e. monochromatic a.c. light, is the modulated light and results in photoconductivity, which will be linearly proportional to the generation rate of the a.c. light. Although $\gamma$ measured by the dc bias light is less than unity, for the a.c. light $\sigma_{ac} \propto G^{\gamma}$, where $\gamma$ is equal to unity. Thereby, the a.c. light does not change $\mu\tau$ product during the measurement. The second condition, which is uniformly absorbed light, is also satisfied. Even at the energies around the
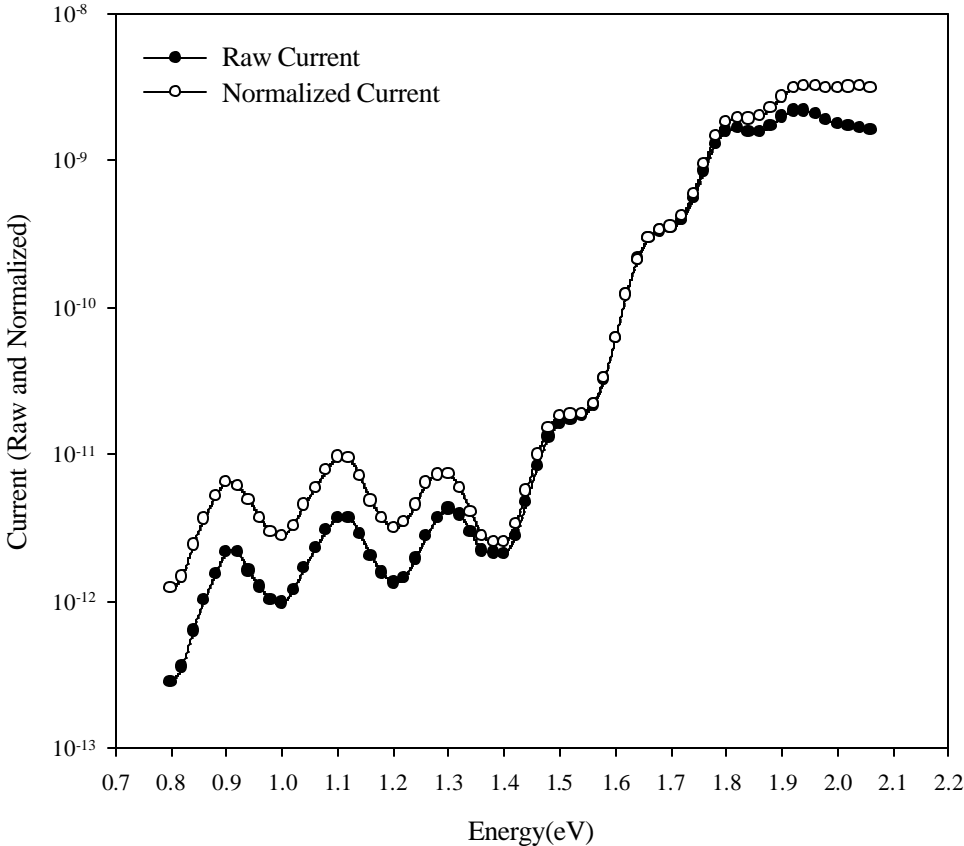


Figure 3.7. Raw and normalized photocurrent spectra of an a-Si:H thin film measured by DBP method

bandgap, where $\alpha$ ($E_{GAP}$) $\approx 10^3$ cm$^{-1}$, $\alpha$ t product is smaller than unity for 1 μm thick sample. When the energy decreases, $\alpha$(hν) reduces exponentially and $\alpha$t becomes much more smaller than unity. If one has absolute absorption coefficient data down to the bandgap energies, the normalization of photocurrent spectrum to absolute absorption spectrum at a single energy will result in $\alpha$(hν) values down to 0.8 eV. These values at lower energies are important indications of the defect states lying in the bandgap of amorphous semiconductor. Absolute $\alpha$(hν) values at about bandgap energies are generally measured using T&R spectra of the same sample or using the PDS spectrum.

It is sometimes very difficult to obtain reliable $\alpha$(hν) values down to bandgap energies using T&R for 1 μm thick films. Therefore, accuracy of sub-bandgap absorption spectrum of DBP method relies on the reliability of absolute $\alpha$(hν) values at normalization energy. Example of normalized photocurrent spectra to absolute $\alpha$(hν) values at one energy is shown in Figure 3.8. Photocurrent spectrum normalized at 1.70 eV
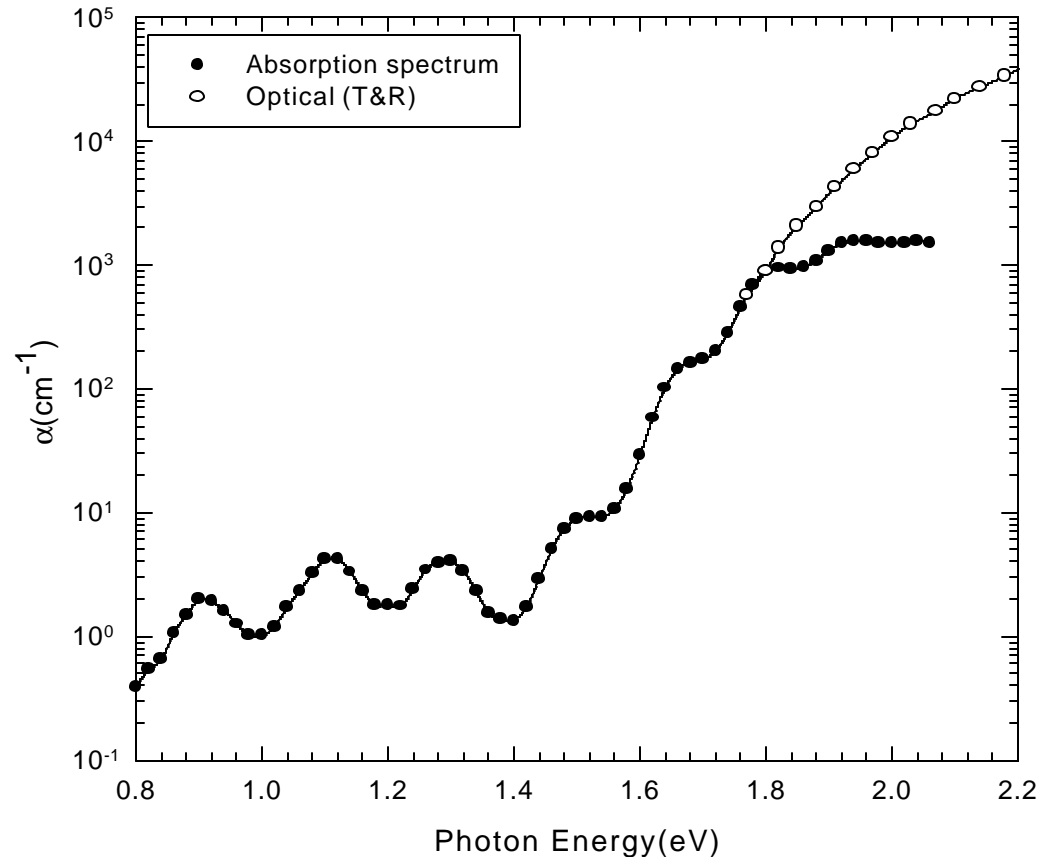


Figure 3.8.    Sub-bandgap absorption and T&R spectrum of an a-Si:H thin film

shows a good transition to absorption coefficient values at lower energies. However, at higher energy part where d.c. and a.c. photocurrents become comparable, above 1.78 eV a deviation exists in the DBP spectrum. It is due to non-uniform absorption of light and deviations from the assumptions used in this method. However, below normalization point, spectrum gives exponential valance band tail state absorption and sub-bandgap absorption shoulder below 1.4 eV. The magnitude of $\alpha(h\nu)$ in the low energies below 1.4 eV can be used to evaluate the density of states in a-Si:H films.

### 3.5.1. Intensity Dependence of Dual Beam Photoconductivity Spectrum

The major advantage of dual beam photoconductivity technique is to use two light beams. The monochromatic a.c. light is used to probe especially band-gap defects. Bias light is used to investigate sub-bandgap absorption for different generation rate values. Physically, the bias light controls the quasi-Fermi levels and changes the occupation of the midgap defect states in the bandgap. Since more defect states can be investigated quasi-Fermi levels move towards the band edges with increasing bias light intensity, this property is reflected in an increased electron transition from the midgap states into the conduction band edge. Thereby an increase in absorption curve in low energies is observed. However, this increase is not observed at the Urbach edge and extended states, which means that altering the bias light does not add any states to tail and extended states. It only shows the effects of occupied midgap states due to bias light intensity.

A red light emitting diode (LED) combination was used as a bias light to perform the experiments for a-Si:H based samples. The LEDs were hold close to each other and a diffuser was used to obtain a uniform illumination. The current, which is only due to bias light in the dark, was matched to the photocurrent from the steady state photoconductivity measurement to use the correct generation rate value. For all thin films, sub-bandgap absorption was measured for a few generation rate values of bias light. Figure 3.9 shows sub-bandgap absorption spectra of an a-Si:H thin film for different generation rates. The increase in generation rate leads to an increase in absorption in the subgap region. The change in sub-bandgap absorption at higher intensity depends on the quality of the sample, in other words it depends on the density, nature and distribution of midgap defect states in the film. Hence, intensity dependence

of the DBP spectra allows us to obtain additional information about the midgap defect states in the bandgap.
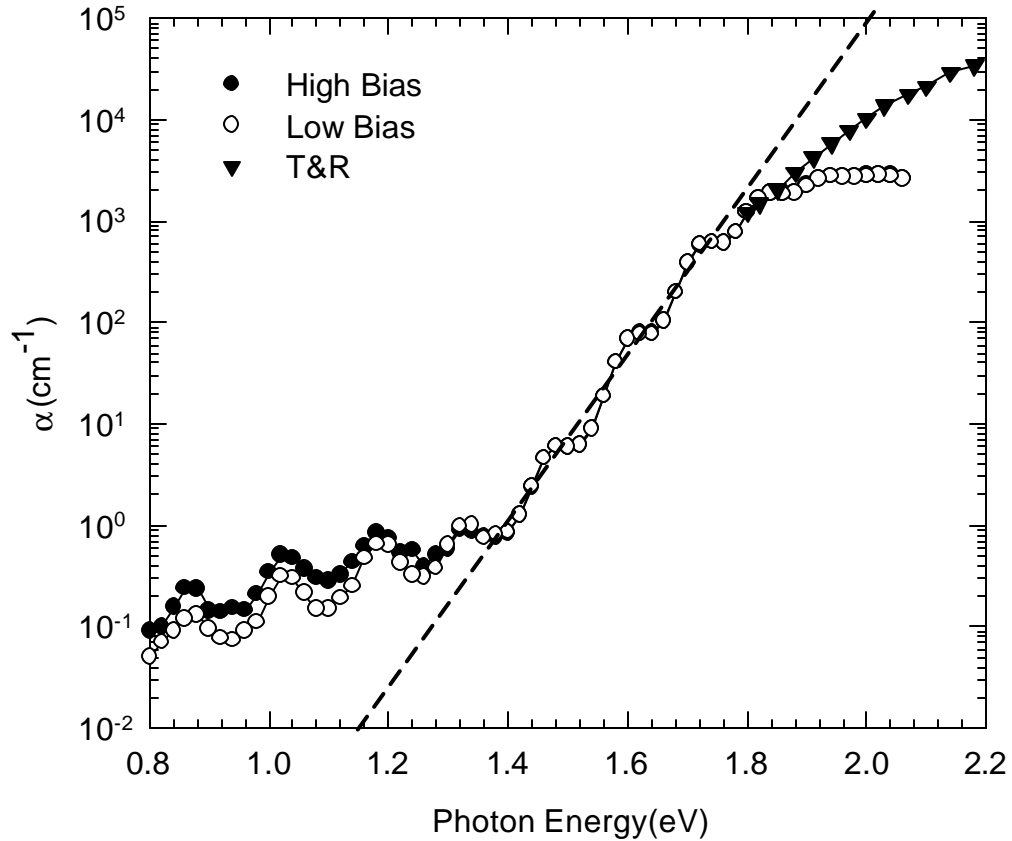


Figure 3.9    Sub-bandgap absorption spectra of an a-Si:H thin film for two different generation rates.

### 3.5.2. Valance Band Tail Slope

One of the main features of the subgap absorption spectrum is to identify the exponential absorption region resulting from the transitions of electrons from occupied exponential valence band tail states in to the empty conduction band extended states. The value of the characteristic energy (Urbach slope) of the exponential decay in the sub-band gap spectrum is used to find the characteristic energy of the exponential valence band tail states distribution. The characteristic energy, $E_{0V}$, is a measure of the degree of disorder in amorphous network and determines whether the thin film is device quality or not. For a-Si:H, in the range of approximately 1.4 eV-1.8 eV, the absorption

coefficient has an exponential dependence on photon energy as seen in Figure 3.9 (dashed line) and can be written as:

$$a_{EXP} = a_0 - \exp\left(\frac{E}{E_{0V}}\right)$$ (Eq. 3.2)

where $\alpha_0$ and $E_{0V}$ are characteristic absorption coefficient and energy of the exponential absorption region, respectively. A narrow valence band tail gives a small characteristic energy that can be interpreted as a device quality film. The film having 50-55 meV characteristic energy of exponential absorption region is known as device quality film for a-Si:H. The valence band tail slope was calculated for all a-Si:H thin films by using the sub-bandgap absorption spectra. These are given in chapter 4.

### 3.5.3. Estimation of the Density of Midgap States

After measuring the reliable sub-bandgap absorption coefficient spectrum, the analysis of sub-bandgap absorption spectra is not straightforward. The absolute value of the derived density of states depends on the method of data analysis and calibration factors. Generally the calibration factor is obtained from ESR measurements but there must be an agreement in that ESR and the sub-bandgap absorption methods detect the same defects. In this thesis, the absorption coefficient at a single energy [62-64] described in chapter2 was used to interpret sub-bandgap absorption spectra and to acquire density of states using the low intensity DBP spectrum. Since the condition for low intensity is close to that of CPM spectrum and it is believed that only defect states below the midgap are estimated at this condition. Then, this will allow us to judge the electronic quality of a-Si:H films by comparing their sub-bandgap absorption coefficients at low energies and the estimated defect state densities in the samples. The results and extended discussion will be given in the following chapter.

### 3.5.4. Transmission Spectrum

Transmission measurements are important to get knowledge about the material in addition to absorption measurements. An example of transmission and absorption spectrum is shown in Figure 3.10. At higher energies, most of the portion of light is

absorbed by the film. Transmission decreases with increasing absorption. Reflection does not change significantly according to these results. Thereby, one of the assumptions of DBP, constant reflection, is satisfied.

The pyrodetector was mounted into the sample holder to obtain the transmission spectrum by measuring the voltage by means of lock-in amplifier. A 9V standard battery was used to operate the pyroelectric detector. The major property of the pyroelectric detector is that it is sensitive to a wide range of the optical spectrum including the red and the infrared regions. The normalized spectra were obtained by dividing the voltage-photon energy ratio to flux. Transmission spectrum can also be used to obtain the film thickness. The sample thicknesses were calculated by using the maximum points of the fringes at the minimum energies of the transmission spectra. The thickness values are given in chapter 4. They are approximately 1 µm as expected.
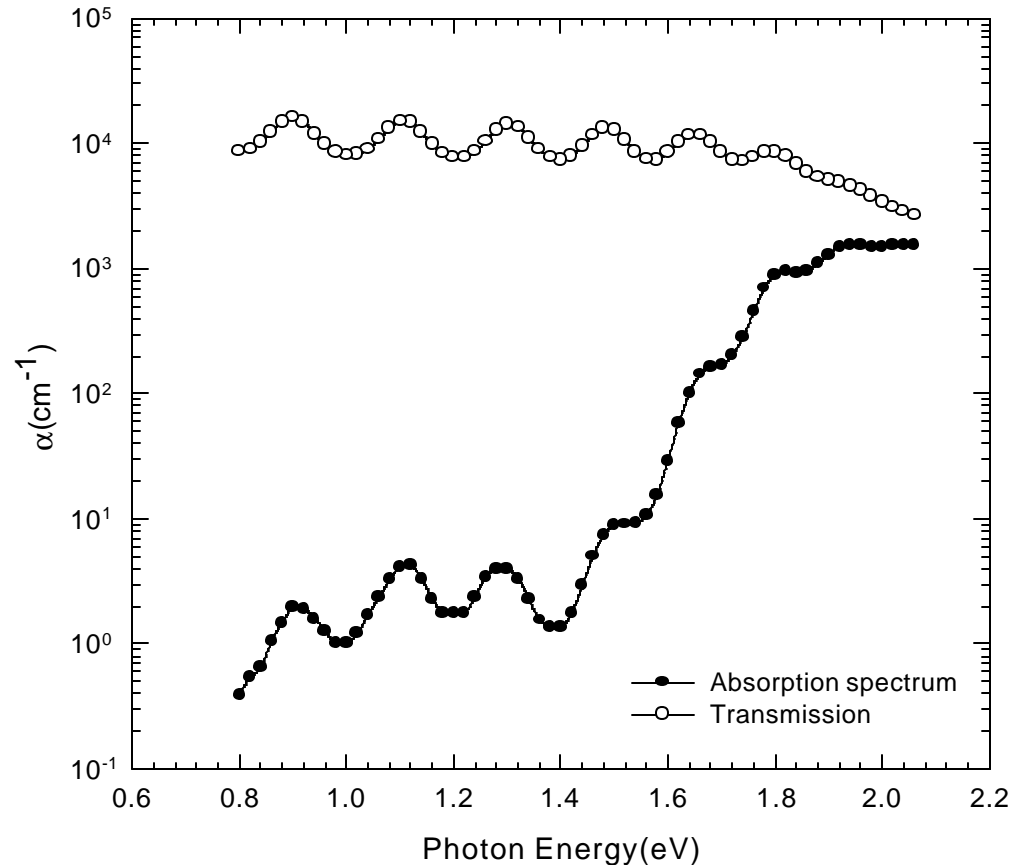


Figure 3.10. A characteristic transmission spectrum of undoped an a-Si:H thin film with its absorption spectrum

## 3.6. Conclusion

In this chapter, the setup, the properties and the applications of the dual beam spectroscopy system were explained in detail. The system was established to measure the sub-bandgap absorption spectra of a-Si:H thin films. These relative spectra will provide true absorption coefficient spectra using their respective transmission and reflection data. In addition, the system was used to obtain transmission data of the films and calibrate the flux of white light using photodiodes and pyrodetector. According to above results, the system gives reliable data and can be used to characterize defect states and understand their behavior in a-Si:H thin films both in the annealed and light soaked states since the absorption coefficient is directly related to band tail disorder and density of midgap defect states. In fact, the final aim is to use the system in an efficient way and to investigate optical and electrical properties of these films in detail. The detailed experimental results on these thin films are given in chapter 4.

# CHAPTER 4

# EXPERIMENTAL RESULTS IN
# HYDROGENATED AMORPHOUS SILICON THIN FILMS

## 4.1. Introduction

Hydrogenated amorphous silicon (a-Si:H) is an important class of amorphous semiconductors due to its electrical and optical properties. Due to disorder in the structure, there exist electronic defects in the bandgap of the material such as dangling bonds and tail states. These defect states mainly control dark and light transport properties. Their effects can be observed in electronic and optical characterization. In this chapter, the dual beam photoconductivity technique established in this thesis study and dark and photoconductivity will be used to understand the effects of these defect states. Furthermore, a-Si:H films degrade under white light illumination due to the creation of the light induced defects in addition to those of native ones. The effects of light induced defects will also be characterized using the same methods. For this purpose, device quality undoped (intrinsic) a-Si:H films prepared by various deposition systems will be used and their properties will be investigated. The samples studied in this thesis are shown in Table 4.1.

Table 4.1. A-Si:H samples used in this study where $T_S$ is the substrate temperature.

| SAMPLE | DEPOSITION TECHNIQUE | DEPOSITION PLACE |
|---|---|---|
| LJ51 (Diluted) | RF-PECVD | Pennsylvania State University and United Solar Systems Corporation of Michigan(USA) |
| LJ70 (Undiluted) | RF-PECVD | |
| SmartA1 ($T_S$=260 $^o$C) | DC-Glow Discharge | BP Solarex (Pennsylvania) (USA) |
| SmartB1 ($T_S$=215 $^o$C ) | | |
| 1586T | RF Magnetron Sputtering | University of Illinois Urbana-Champagne (USA) |

In this study, mainly two deposition systems were used to prepare a-Si:H thin films. These are plasma enhanced chemical vapor deposition (PECVD) and RF magnetron sputtering. PECVD consists of forming deposits by initiating chemical reactions in Silane (SiH$_4$) with an electric discharge (plasma) [70]. Growth is controlled by chemical reactions between precursor species (SiH$_4$ and H$_2$) and the surface. During PECVD, SiH$_4$ gas with or without H$_2$ (dilution) gas is pumped through a set of parallel plate electrodes, where radio frequency (RF) or direct current (DC) power drives one electrode and creates the glow discharge. Hydrogen dilution technique is the incorporation of H$_2$ gas through the silane (SiH$_4$) in the plasma at some definite ratios, R=H$_2$ / SiH$_4$. In DC-PECVD called DC-glow discharge [70], the substrate acts as a cathode. The anode is usually a metal plate or screen located a few centimeters above the substrate. In RF-PECVD, generally only one electrode is powered and substrate is located on the grounded electrode. These systems usually operate at 13.56 MHz. In RF Magnetron sputtering system [3,71], the plasma extends between the parallel target and the substrate. A polycrystalline Silicon target is located on the powered electrode and the sputtering atmosphere is a mixture of Argon and H$_2$. Argon gas is ionized by RF electric field. When the ions impact the target (the material to be sputtered) they can set up a series of collisions with the target atoms, which lead to ejection of these atoms. These atoms condense on the substrate and a thin film is formed.

## 4.2. Annealed State and Native Defects

In the annealed state, dark and light transport properties of a-Si:H films are controlled by native defects. Their effects will be investigated using dark conductivity, photoconductivity and sub-bandgap absorption methods.

### 4.2.1. Dark Conductivity

Activation energy is the energy difference between conduction band mobility edge and the dark Fermi level. The position of the dark Fermi level is sensitive to the impurities, defects, and dopants, and thereby it determines the occupation of gap states in the dark. Bandgap and the position of dark Fermi level depend strictly on the deposition conditions and hydrogen content of the film. Hence, dark conductivity and the position of the Fermi level are important physical parameters for undoped a-Si:H

films. The optical bandgap of undoped a-Si:H is generally between 1.7 eV-1.8 eV. It is approximately equal to the energy at $\alpha = 1000$ cm$^{-1}$. Mobility gap or "recombination gap" is assumed to be about 0.1 eV larger than the optical gap [69]. The Fermi levels of undoped a-Si:H thin films are generally at or near the middle of the bandgap.

The annealing system described in section 2.5.2 was used to perform the dark conductivity measurements as a function of temperature. Dark conductivities were calculated from Eq.2.25 using dark current, applied voltage and sample geometry. The slopes of Arrhenius plots of dark conductivities were used to find the activation energies in the temperature range between 340 K and 430 K. The dark conductivity measurements of hydrogen diluted and undiluted a-Si:H prepared by RF-PECVD, and films prepared by DC-Glow discharge and RF magnetron sputtering are shown in Figure 4.1. Dark conductivity data at room temperature and the activation energy values of the a-Si:H samples are given in Table 4.2. All undoped films show similar characteristics such that dark Fermi level is near the middle of the bandgap. However, the magnitude of dark conductivity shows a variation of 1 order of magnitude due to differences in preparation conditions. Although there is a variation in dark conductivity, its value is very low implying that undoped a–Si:H is a perfect resistor in dark. RF-PECVD samples have the highest dark conductivity values at high temperatures. However, at room temperature, LJ70 and SmartA1 have higher dark conductivity than the others due to differences in the bandgap and activation energy values of the samples.

Table 4.2. Room temperature dark conductivity and activation energy values of undoped a-Si:H films.

| SAMPLE | $E_{ACT}$ (eV) | $\sigma_{DARK}$(room T) $(\Omega\text{-cm})^{-1}$ |
|---|---|---|
| LJ51 (Diluted RF-PECVD) | 1.07 | $6.0 \times 10^{-12}$ |
| LJ70 (Undiluted RF-PECVD) | 0.91 | $1.5 \times 10^{-11}$ |
| SmartA1 (DC-GD) | 0.90 | $1.0 \times 10^{-11}$ |
| SmartB1 (DC-GD) | 0.98 | $3.0 \times 10^{-12}$ |
| 1586T (Sputtered) | 1.07 | $1.5 \times 10^{-12}$ |
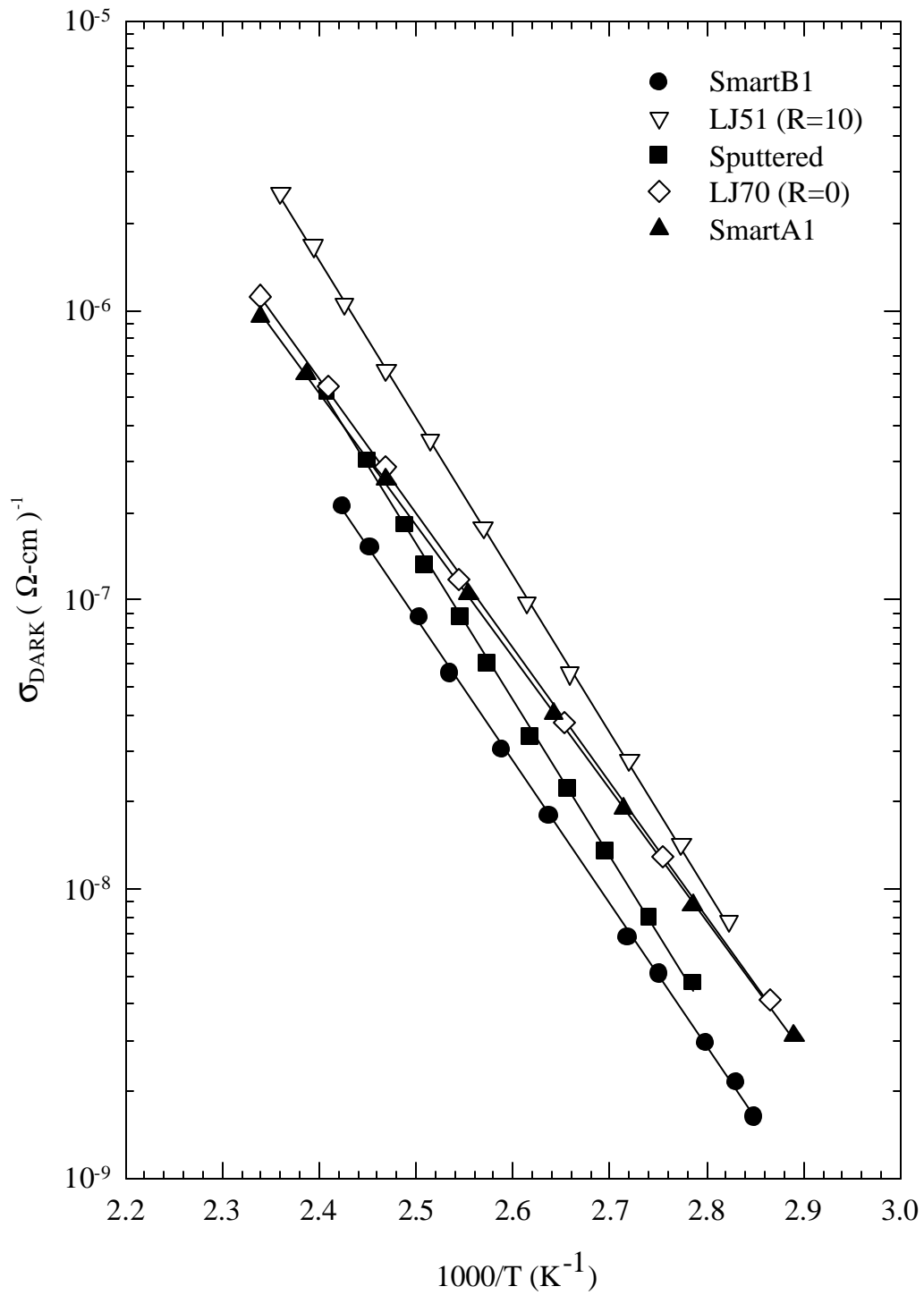
Figure 4.1.    Arrhenius plots of undoped a-Si:H thin films prepared by RF-PECVD, DC-Glow Discharge and Magnetron Sputtering.

### 4.2.2. Steady-state Photoconductivity

Steady-state photoconductivity is a complex process of free carrier generation across the bandgap, recombination of free carriers through the defect states and transport of free carriers at the conduction band mobility edge. Therefore, it involves the absorption coefficient of material, density and nature of recombination centers and mobility of free carriers at the extended states. In other words, it provides full information about the material. The non-integer power-law dependence on generation rate of steady-state photoconductivity, ($\sigma_{PH} \propto G^{\gamma}$), is an important physical feature, giving information about the recombination kinetics as described in chapter 2. The value of $\gamma$ indicates the type of recombination kinetics between the electrons and holes. It also provides additional information about the material itself. Steady-state photoconductivity is also used to obtain the electron mobility-time product, $\mu\tau$, of charge carriers, which is a significant parameter for device applications. Due to existence of tail states in amorphous semiconductors, free carriers are mainly trapped and emitted during the transport in the extended states. In a-Si:H, the valence band tails are wider than the conduction band tails. Hence, free holes are mainly trapped in the valence band tail states and their mobilities are found to be lower than that of electrons. Therefore, photoconductivity will be dominated by the free electrons in the conduction band. For this reason, $\mu\tau$ product obtained from the steady-state photoconductivity will give a direct information about the majority carrier electrons.

Steady-state photoconductivity measurements in the annealed state were performed for volume generation rates from $10^{15}$ to $10^{20}$ cm$^{-3}$s$^{-1}$ at room temperature. The steady-state photoconductivity system described in section 2.5.1 was used for the measurements. Incident flux of white light was calibrated before each measurement using silicon p-i-n photodetector and was calculated using Eq.2.22 and quantum efficiency values for 690 nm interference filter. Neutral density filters were used to obtain lower values of incident flux. Generation rate for the filter 690 nm was calculated using the respective absorption coefficient value, $\alpha$(690 nm), incident flux, reflection, and sample thickness. The reflection from the front surface was taken to be R=0.35 as given in literature. Figure 4.2 shows steady-state photoconductivity measurements versus relative intensity values of a-Si:H sample SmartB1 prepared by DC-glow discharge for both 690 nm interference and RG-610 nm bandpass filters. Since the

optical gap of a-Si:H is about 1.7-1.8 eV, it can be expected that photons with 1.8 eV (690nm) excite electrons from valence band extended states to the conduction band extended states. For samples used in this study, $\alpha(1.8 \text{ eV}) \approx 1000 \text{ cm}^{-1}$ and the thickness of the samples is around 1 $\mu$m. Thus, the condition for uniform absorption is $\alpha t = 0.1 << 1$. For these samples, measured photoconductivity due to volume absorption of light is reliable and reflects the effect of bulk of the samples. For the filter RG-610, photons with wavelength greater than 610 nm are absorbed by the film. RG-610 is a bandpass filter. The generation rate calculation for this filter is directly impossible. However, as seen from relative intensity vs. photoconductivity data, both filters show the same power dependence ($\sigma_{PH} \propto F^{\gamma}$). Using this property, we can use the 690 nm data and shift the curve of RG-610 filter multiplying relative intensities of RG-610 filter by a constant number. This constant number is used to find the 100% generation rate value of RG-610 filter using the generation rate of 690 nm filter. This simple process can be written as the following. In Figure 4.2, at point A $\sigma_{PH} \propto G(610)*r_A$ and at point B; $\sigma_{PH} \propto G(690)*r_B$, where G(690) and G(610) are generation rate values for 100% and $r_A$ and $r_B$ are relative intensity values of RG-610 and 690 nm filters, respectively. Since photoconductivity values at A and B are equal, $G(610) = G(690)(r_B / r_A)$. The idea of this normalization is that under the same generation rate due to either 690 nm filter or RG-610 filter, resulting photoconductivities are the same. After normalization, it can be seen that data obtained using two filters lie on the same line and mostly the values of RG-610 give the higher generation rate values as seen in Figure 4.3. Using RG-610 bandpass filter allows us to obtain higher generation rates and observe the effects of native defect states in a wider generation rate values.

Using this process, measured steady-state photoconductivity and calculated $\mu\tau$ products of the a-Si:H films produced by RF-PECVD system are shown in Figure 4.4. Sample LJ70 prepared without H$_2$ dilution has higher photoconductivity and its exponent $\gamma$ is 0.91. For sample LJ51 prepared in the same system with H$_2$ dilution, $\sigma_{PH}$ decreased by a few factor due to slight increase of the bandgap or differences in the defect states. The exponent $\gamma$ also decreased slightly to 0.84. However, both values of $\gamma$ are closer to unity, meaning that electrons in the conduction band mobility edge recombine with holes through the midgap defect states. In addition, the $\mu\tau$ products of electrons are shown in the Figure 4.4b imply that those are in the range of the device quality a-Si:H films reported in the literature[69]. Similar device quality a-Si:H films
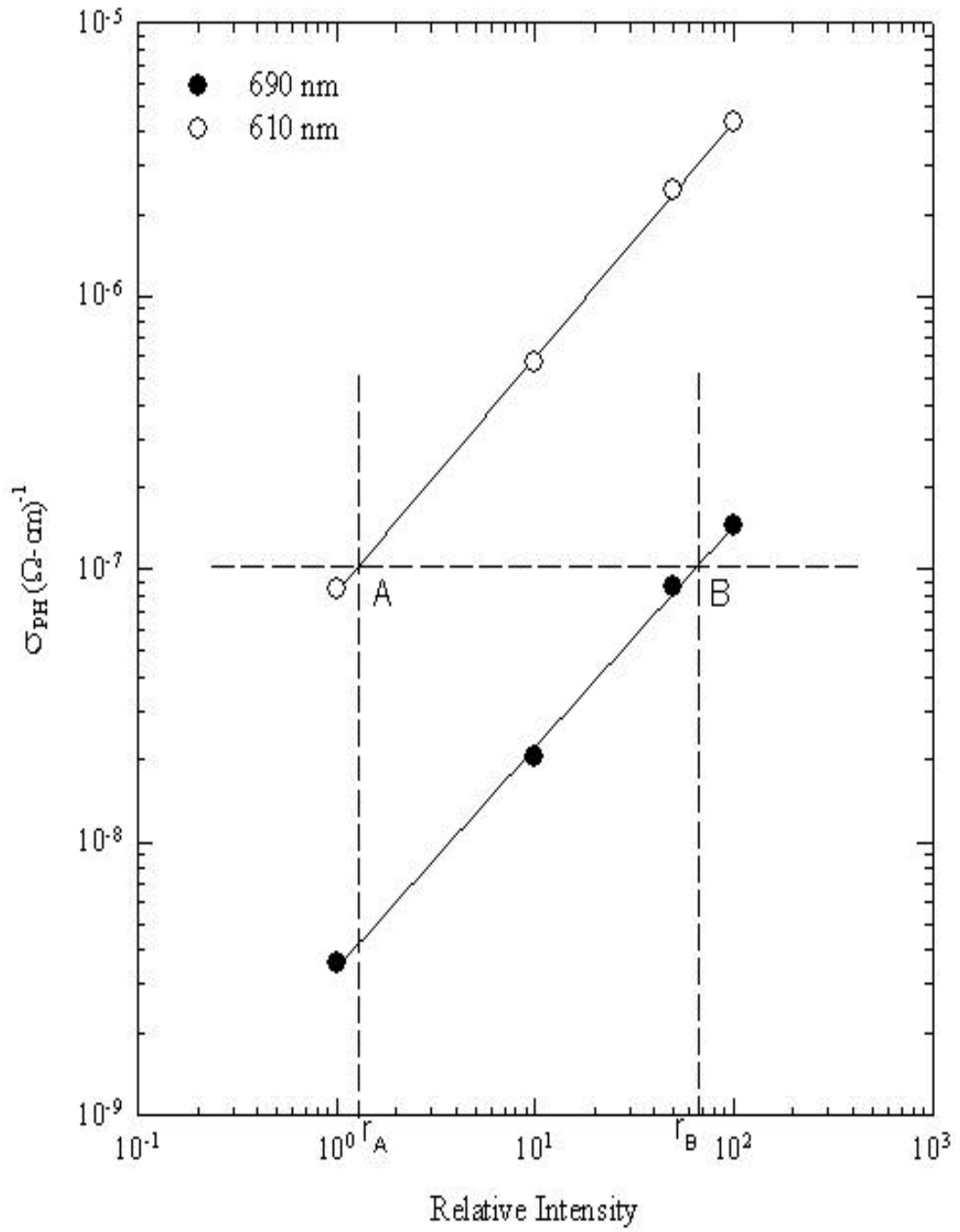
Figure 4.2. Steady-state photoconductivity of DC-GD a-Si:H sample SmartB1 measured using 690 nm and RG-610 filters in the annealed state.
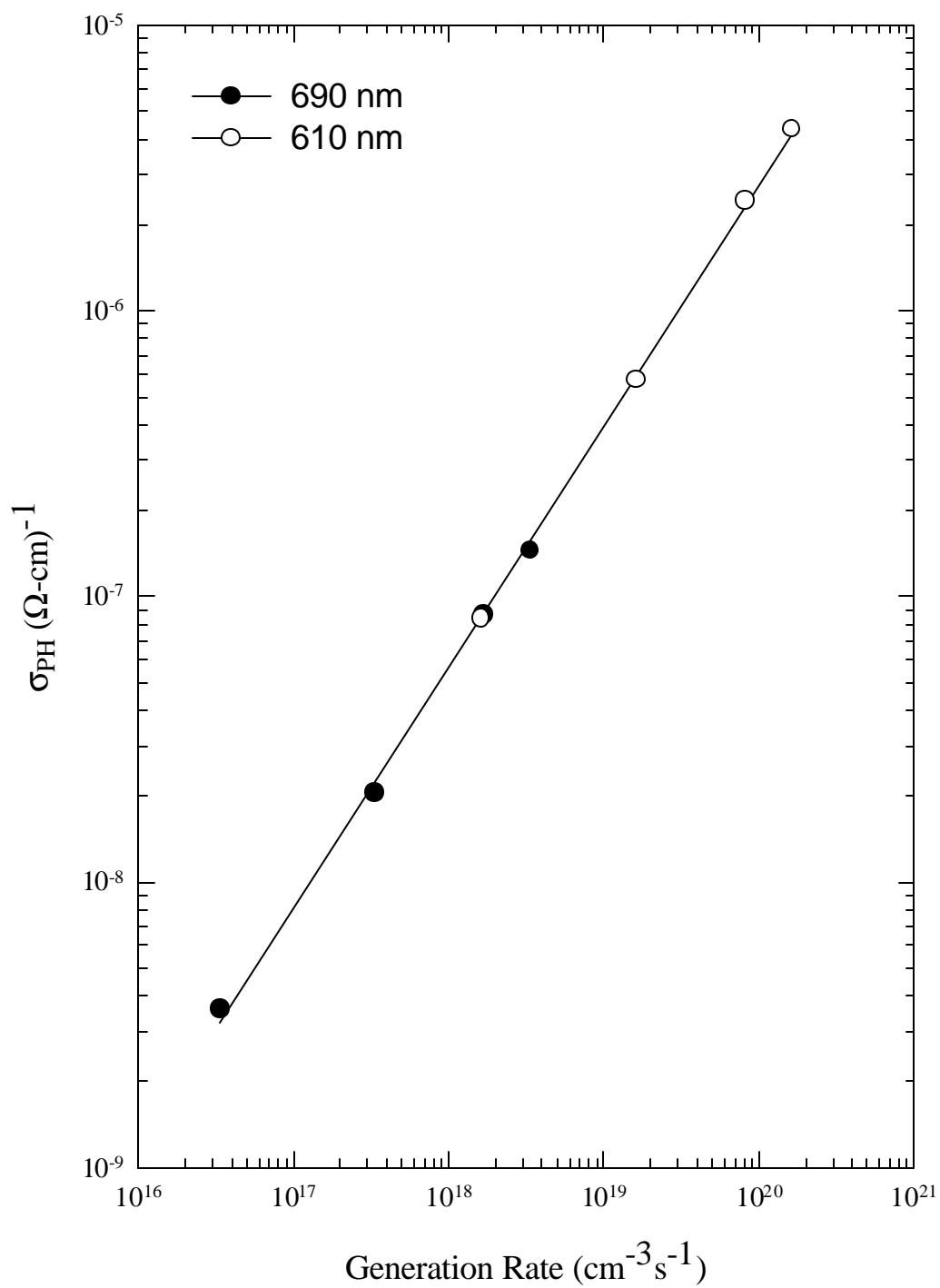
Figure 4.3.    Combined steady-state photoconductivity graph of DC-GD a-Si:H sample SmartB1.

can also be prepared using DC-glow discharge [70] and magnetron sputtering [3,71] systems. Steady-state photoconductivities of those films are shown in Figure 4.5a and respective $\mu\tau$ products in Figure 4.5b. As seen from this figure, all three samples have $\gamma$ around 0.85 indicating similar defect distribution in the bandgap. However, there exists a difference in the magnitude due to differences in the defect density in different materials. Sample SmartA1 is prepared at 260 $^{o}$C and SmartB1 is at 215 $^{o}$C. Differences in substrate temperatures during the deposition lead to different H concentration in the films. This changes defect density in the film and reflected in measured photoconductivity. Similarly, a-Si:H prepared by sputtering gives similar result, both in magnitude and in the exponent of photoconductivity.

Table 4.3 summarizes the results of photoconductivity measurements. Thicknesses of the samples were obtained using transmission measurements. For all a-Si:H films, the values of $\gamma$, are between 0.8 and 1.0, close to unity. This indicates that free electrons in the conduction band recombine with the free holes in the valance band through the recombination centers in the bandgap. Therefore, defect states exist in the bandgap, and these states affect the electronic properties of material. The differences in $\gamma$ values can be due to differences in the density and energy distribution of defect states in the bandgap of a-Si:H films. For two generation rates, photoconductivity and $\mu\tau$ product values are compared in Table 4.3. It is clearly seen that $\sigma_{PH}$ at high generation rate (G=$10^{20}$ cm$^{-3}$s$^{-1}$) is much higher than $\sigma_{DARK}$ for all samples by 5 or 6 orders of magnitude. Hence, the photosensitivity, $\sigma_{PH}/\sigma_{DARK}$, is very high indicating that a-Si:H films are very good materials for optoelectronic applications. LJ70 gives the highest photoconductivity and thus the highest $\mu\tau$ values whereas DC-Glow Discharge sample SmartB1 shows the lowest values for both generation rates. DC-GD samples SmartA1 and SmartB1 shows almost same $\gamma$ values whereas their photoconductivity values are different. This indicates that electronic properties of a-Si:H films are strongly dependent on the preparation conditions even if they are made in the same system.

Mobility–lifetime product, $\mu\tau$, results of a-Si:H films in the annealed state were deduced from steady-state photoconductivity measurements using Eq.2.26. As seen in Figures 4.4 and 4.5, when the generation rate increases, the $\mu\tau$ product decreases since $\gamma$ values are less than unity. This means that increase in generation rate results in that more midgap defect states transform into the recombination centers as suggested by Simmons and Taylor statistics [72,73]. More recombination centers reduce the lifetime
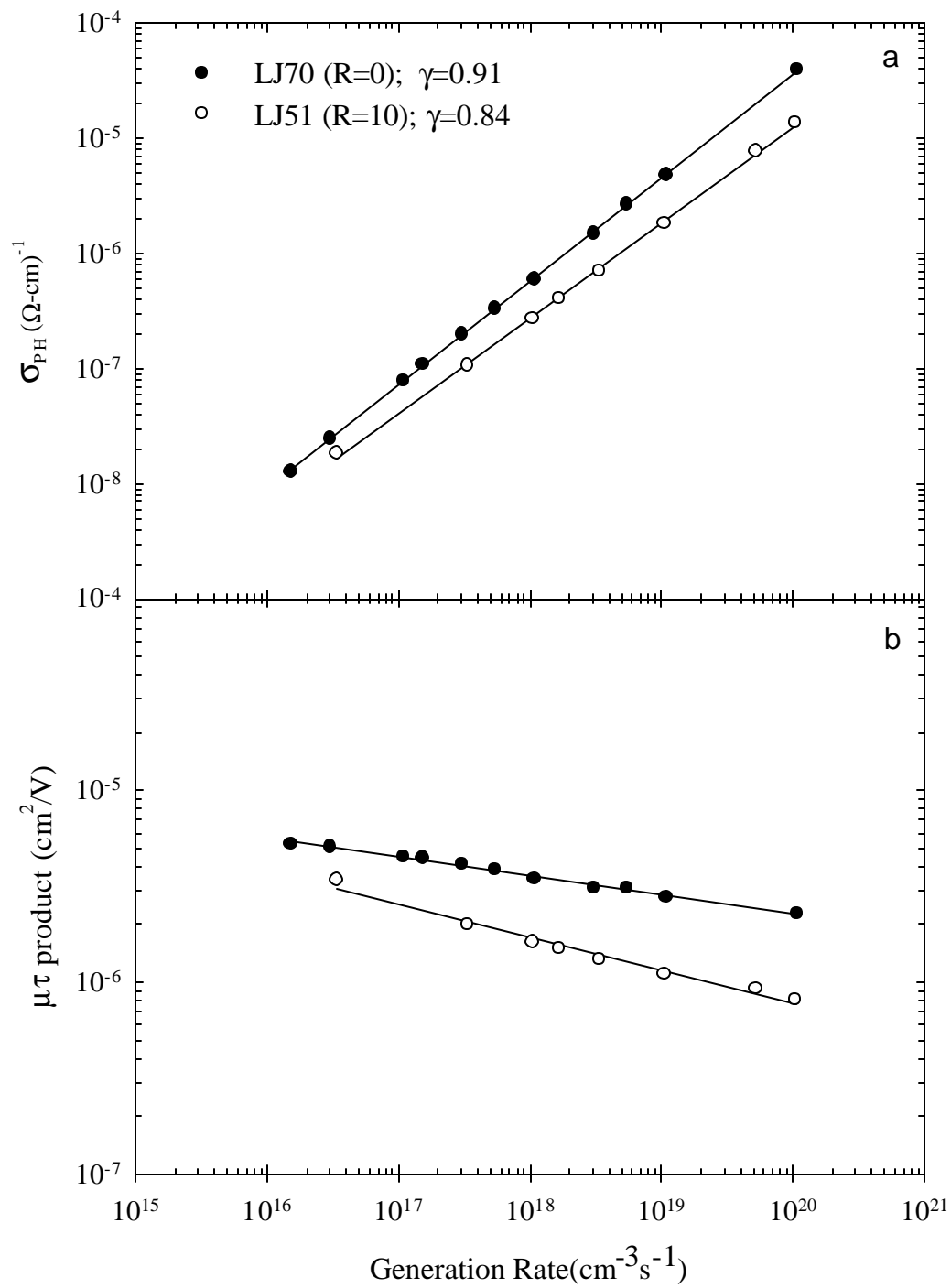
Figure 4.4.    Steady-state photoconductivity (a) and $\mu\tau$ product (b) versus generation rate results of RF-PECVD a-Si:H samples in the annealed state.
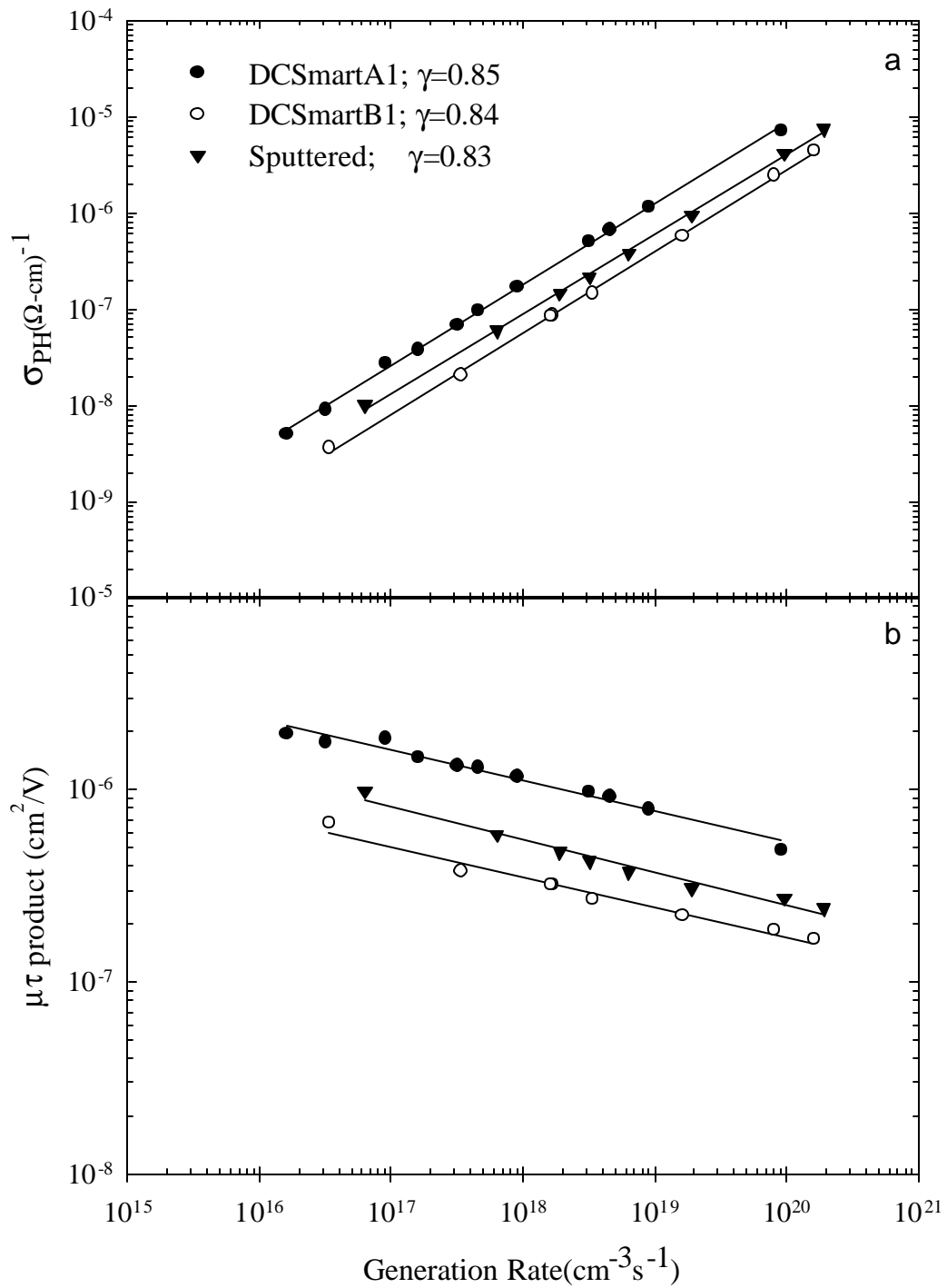
Figure 4.5.    Steady-state photoconductivity (a) and $\mu\tau$ product (b) versus generation rate results of DC-GD and sputtered a-Si:H samples in the annealed state.

of the carriers, which directly affects the electronic quality of the material. The values of photoconductivity and $\mu\tau$ product of the a-Si:H films show differences but they are very close to each other within in a factor of 3. Since midgap defect states are the main recombination centers in a-Si:H samples and control the photoconductivity, densities of these states are expected to be very close to each other for these films. However, it is not possible to obtain quantitative information about these defect states using these $\sigma_{PH}$ results due to complexity in the generation and recombination processes in a-Si:H films.

Table 4.3.     Steady-state photoconductivity and $\mu\tau$ product results of a-Si:H thin films in the annealed state

| SAMPLE | LJ51 | LJ70 | SmartA1 | SmartB1 | 1586T |
|---|---|---|---|---|---|
| Thickness ($\mu$m) (from transmission) | 0.88 | 1.26 | 1.10 | 1.10 | 1.10 |
| $\gamma$ | 0.84 | 0.91 | 0.85 | 0.84 | 0.83 |
| $\sigma_{PH}(G=10^{20}\text{cm}^{-3}\text{s}^{-1})(\Omega\text{-cm})^{-1}$ | $1.3\times10^{-5}$ | $3.6\times10^{-5}$ | $7.9\times10^{-6}$ | $2.8\times10^{-6}$ | $4.0\times10^{-6}$ |
| $\sigma_{PH}(G=5\times10^{16}\text{cm}^{-3}\text{s}^{-1})(\Omega\text{-cm})^{-1}$ | $2.3\times10^{-8}$ | $3.6\times10^{-8}$ | $1.4\times10^{-8}$ | $4.2\times10^{-9}$ | $7.1\times10^{-9}$ |
| $\mu\tau(G=10^{20}\text{ cm}^{-3}\text{s}^{-1})(\text{cm}^2/V)$ | $7.4\times10^{-7}$ | $2.3\times10^{-6}$ | $5.1\times10^{-7}$ | $1.8\times10^{-7}$ | $2.6\times10^{-7}$ |
| $\mu\tau(G=5\times10^{16}\text{ cm}^{-3}\text{s}^{-1})(\text{cm}^2/V)$ | $3.0\times10^{-6}$ | $4.5\times10^{-6}$ | $1.7\times10^{-6}$ | $5.7\times10^{-7}$ | $8.9\times10^{-7}$ |
| Photosensitivity $\sigma_{PH}(G=10^{20}\text{cm}^{-3}\text{s}^{-1})/\sigma_{DARK}$ | $2.2\times10^{6}$ | $2.4\times10^{6}$ | $7.9\times10^{5}$ | $9.3\times10^{6}$ | $2.7\times10^{6}$ |

### 4.2.3. Sub-bandgap Absorption Spectra

As we studied in the previous section, the effects of the midgap defect states are observed qualitatively in $\sigma_{PH}$ results. More direct investigation about these defect states can be seen in the optical absorption at low photon energies. This is called sub-bandgap absorption spectroscopy. Sub-bandgap absorption spectrum in a-Si:H is due to absorption of photons with energies lower than the bandgap. In a-Si:H films, there is a continuous distribution of defect states located below the bandgap energies. The effects of these defect states have been observed in $\sigma_{PH}$ measurements in the previous section. Therefore, electrons excited from these defect states into the conduction band edge by the absorption of low energy photons can be detected by measuring the sub-bandgap photoconductivities. In this section, the results of the sub-bandgap photoconductivity obtained by the dual beam photoconductivity (DBP) method for undoped a-Si:H films will be presented. The details of the DBP were described previously in chapter 3.

An example of sub-bandgap absorption spectra for the undoped a-Si:H film LJ70 prepared using RF-PECVD without H-dilution of silane for two generation rates is shown in Figure 4.6. The fringes shown in sub-bandgap absorption figures in chapter 3 were removed to obtain an effective $\alpha(h\nu)$ spectrum. Fast Fourier transform (FFT) technique was used to average these interference fringes. After removing the fringes, the photoconductivity spectra were normalized to the $\alpha(h\nu)$ values obtained from the T&R measurements at about optical gap energy. A good overlap can be easily remarked between the T&R spectrum and the normalized spectrum. In parabolic energy region above the bandgap energy, it can be seen that absorption spectra show deviations from T&R measurements. In this region, uniform absorption condition, $\alpha(h\nu)t \ll 1$, in the DBP technique is not satisfied. In addition, dc light current-ac light current ratio (Idc/Iac) is smaller than the required value, which is necessary not to alter quasi-Fermi level during the measurement. Idc/Iac ratios for the two generation rate values are shown in the inset of Figure 4.6. Normalization of the DBP spectrum has to be done by paying attention to $I_{dc}/I_{ac}$ ratio at normalization energy, where $I_{dc}/I_{ac} \gg 1$. For this reason, firstly high bias light DBP data is normalized to that of T&R at a single energy, where $I_{dc}/I_{ac} \gg 1$ and $\alpha t \ll 1$ condition is also satisfied. In the second step, low bias light intensity DBP spectrum is normalized to that of high bias light DBP spectrum since it reflects correct absorption coefficient below normalization energies and T&R

data cannot give reliable values at those energies. Idc/Iac ratio for low bias light DBP spectrum is also taken into account. As seen in the inset, Idc/Iac ratio is greater than 10, where reliable normalization shifted to lower energies, around 1.5-1.6 eV. Then normalization of low G data is done at a single energy in the exponential tail absorption region. Above that normalization point, the DBP data of low bias light is not reliable that can be replaced by the data of high bias light DBP or removed. After normalization of the low bias light DBP, a good overlap can be seen in the exponential region between two DBP measurements. However, deviations exist below 1.4 eV where it is called the sub-bandgap absorption region.

From the optical gap, E ($\alpha$=1000 cm$^{-1}$), down to about 1.4 eV, $\alpha$(hv) decreases exponentially. The exponential decrease represents tail states absorption from the valence band extending into midgap region. A narrow valence band tail gives a small characteristic energy that can be interpreted as a device quality film as defined in Eq.3.1. The characteristic energy, $E_{0V}$, is obtained by fitting to the linear exponential absorption region. For the sample LJ70, it is 53 meV.

As photon energy decreases below 1.7 eV, the $\alpha$(hv) decreases exponentially until energy around 1.4 eV. Then, the $\alpha$(hv) shows a shoulder at lower energies. The DBP spectrum measured at low generation rate reflects the contribution of midgap defect states in the $\alpha$(hv) spectrum. Therefore, the magnitude of $\alpha$(hv) is a kind of representation of the midgap defect states. Defective films show higher sub-bandgap absorption and lower $\mu\tau$ products. In this thesis, our goal is to investigate the level sub-bandgap absorption due to these native defects present in a-Si:H. The reason to use low generation rate DBP spectrum is that sub-bandgap spectrum under this condition will mainly be controlled by the occupied defect states below the dark Fermi level, which is similar to the sub-bandgap absorption spectrum measured by the constant photocurrent method (CPM). This spectrum and magnitude of $\alpha$(hv) at low energies provide a comparison of films prepared under different deposition conditions. For sample LJ70, the $\alpha$(hv) at 1.2 eV is 0.99 cm$^{-1}$. Estimating the density of midgap states located below the Fermi level is not straightforward using the $\alpha$(hv) values. As we described in chapter 2, several procedures have been applied. However, there are serious difficulties in each procedure since each method requires a calibration and certain assumptions. Therefore, we will only use the magnitude of $\alpha$(hv) at a single energy (1.2 eV) to compare the defect levels in different films.
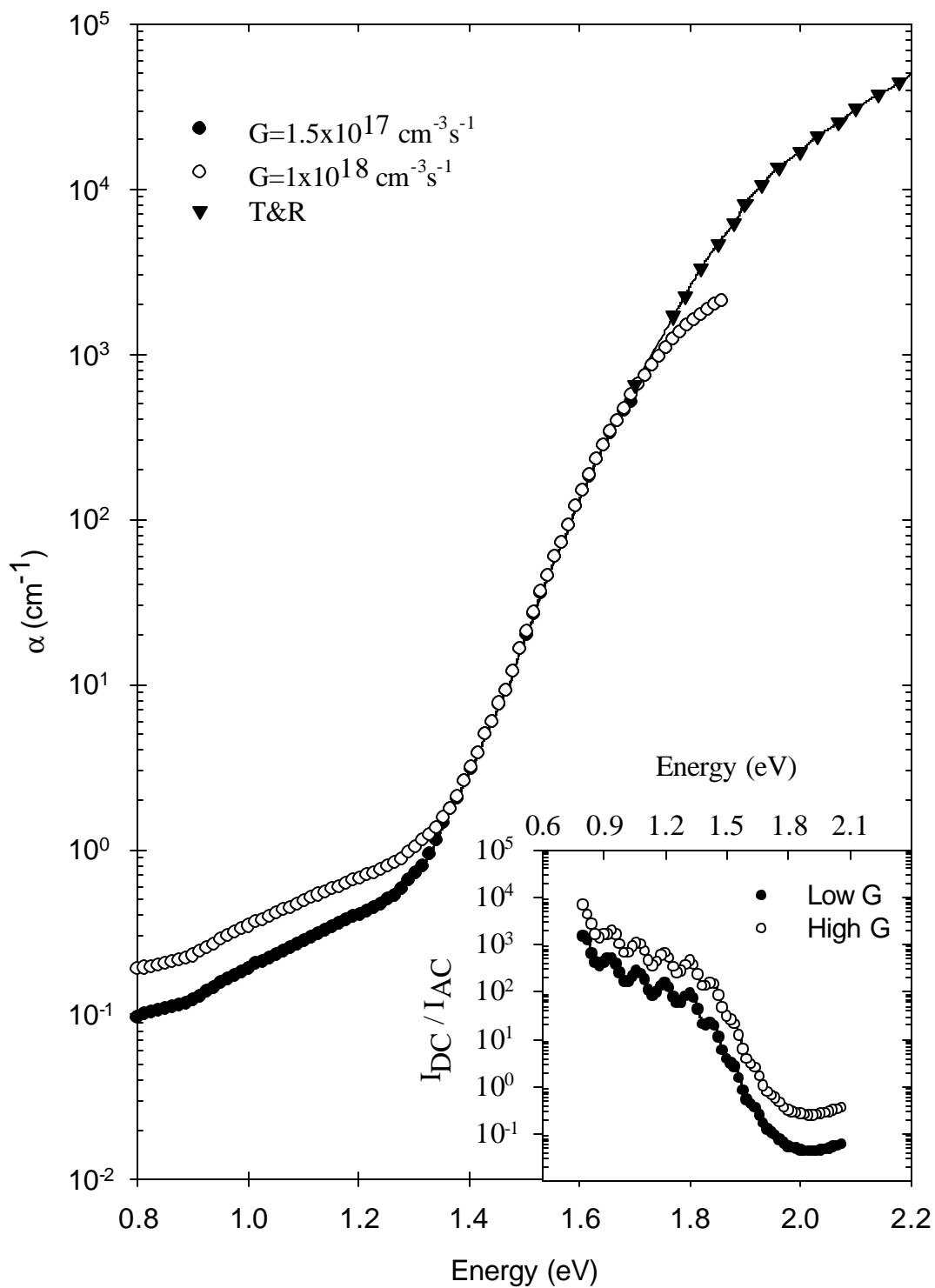
Figure 4.6.    Sub-bandgap absorption spectra of RF-PECVD undiluted a-Si:H sample LJ70 at two generation rates in the annealed state. In the inset, Idc/Iac ratio is shown for two bias light intensities.

In DBP, dc bias light allows us to control the occupation of defect levels in the bandgap. For this reason, changing the generation of bias light will provide us additional information about the defect states. The DBP spectrum measured at high generation rate is given in Figure 4.6 for the same sample LJ70. The $\alpha(h\nu)$ spectra at high energies down to 1.4 eV are exactly same for both generation rates. However, the $\alpha(h\nu)$ in sub-bandgap region shows a significant increase from the low generation rate DBP spectrum. This indicates that only transitions at lower energies contribute to the sub-bandgap absorption. These transitions can originate from the electron occupied states above the Fermi level, which are caused by the high generation rate dc bias light. However, the amount of increase in the $\alpha(h\nu)$ is not a simple process. It depends on a detailed physics of occupation of these defect states as explained by Simmons and Taylor [72,73]. In this study, we will only compare the amount of increase in the magnitude of $\alpha(h\nu)$ at 1.0 eV to compare the native defect distributions in the films. Thus, the intensity dependence of sub-bandgap absorption, $\Delta\alpha(1.0 \text{ eV}) = \alpha(1.0 \text{ eV})(\text{highG})-\alpha(1.0 \text{ eV})(\text{low G})$ for the sample LJ70 is 0.40 cm$^{-1}$ and provides an additional information about the defect states in a-Si:H films.

The effects of midgap defect states in sub-bandgap absorption for other device quality films prepared using different deposition techniques were also carried out. The DBP spectra measured for two generation rates are shown in the Figures 4.7, 4.8, 4.9 and 4.10. The DBP spectra for each film were normalized to the absolute $\alpha(h\nu)$ values obtained from T&R measurements of the same sample. As mentioned previously, the accuracy of the sub-bandgap absorption spectrum is determined by this normalization, where there must be reliable $\alpha(h\nu)$ values. Therefore, we believe that the experimental error in the absolute $\alpha(h\nu)$ in the normalization energies is less than 10%, which is the limit of experimental error. As we see from the sub-bandgap absorption spectra for all samples, there is a fairly good overlap between the DBP spectra and the absolute $\alpha(h\nu)$ of T&R. At higher energies, the $\alpha(h\nu)$ represents absorption through the parabolic extended states. As the energy decreases, there is a sharp decrease in the $\alpha(h\nu)$, showing an exponential decrease in the semi-log plot. This is a characteristic absorption edge for a-Si:H film and the slope of this absorption region is an indication of the disorder in the amorphous network. The characteristic energy, $E_{0V}$, obtained by the linear fit to the absorption curve in energy range from 1.4 eV to 1.7 eV is the characteristic slope of the valence band tail states of amorphous network. For device quality a-Si:H films, $E_{0V}$ is

Figure 4.7.    Sub-bandgap absorption spectra of RF-PECVD diluted a-Si:H sample LJ51 at two generation rates in the annealed state.

Figure 4.8.    Sub-bandgap absorption spectra of DC-GD a-Si:H sample SmartA1 at two generation rates in the annealed state.
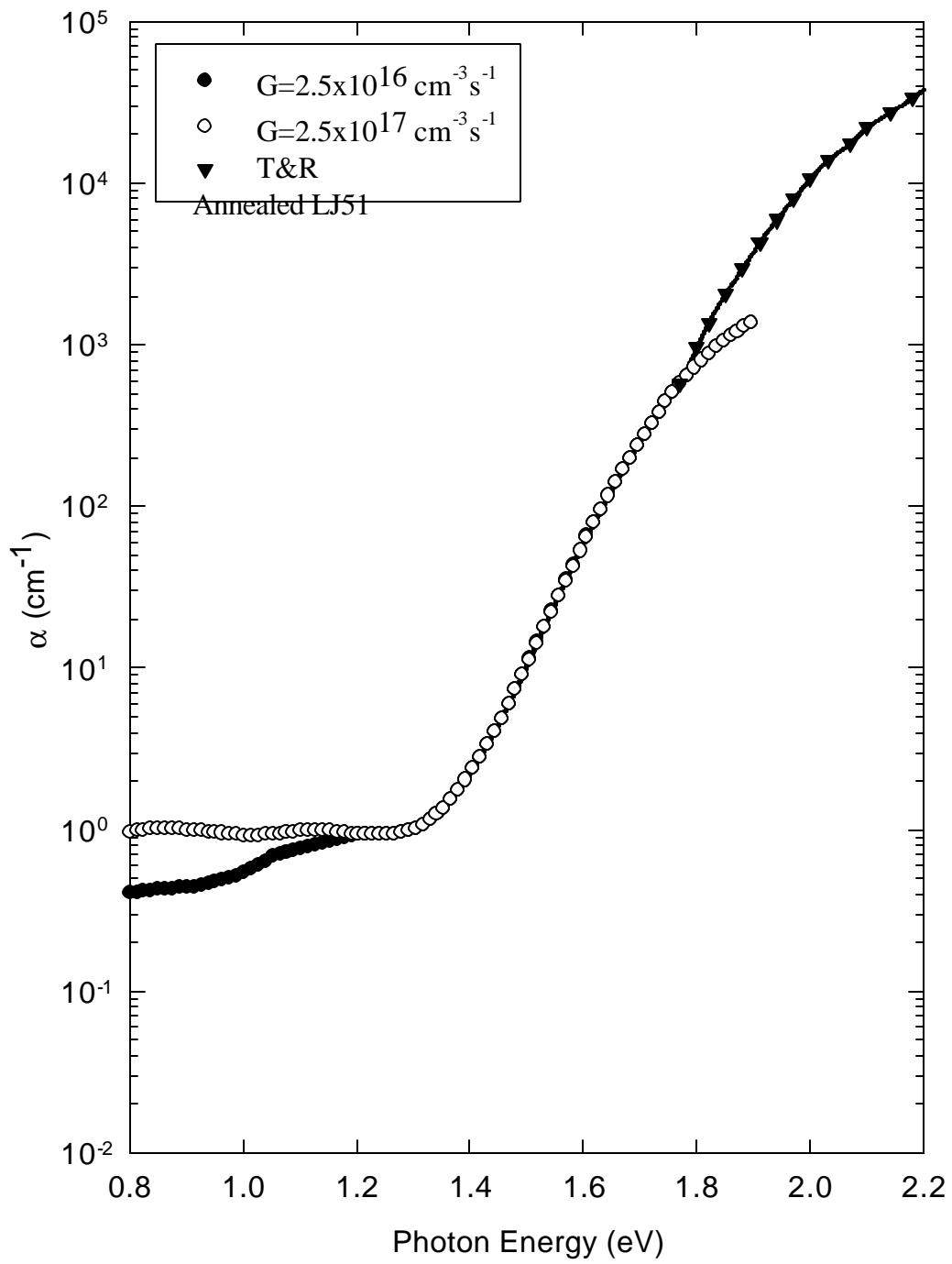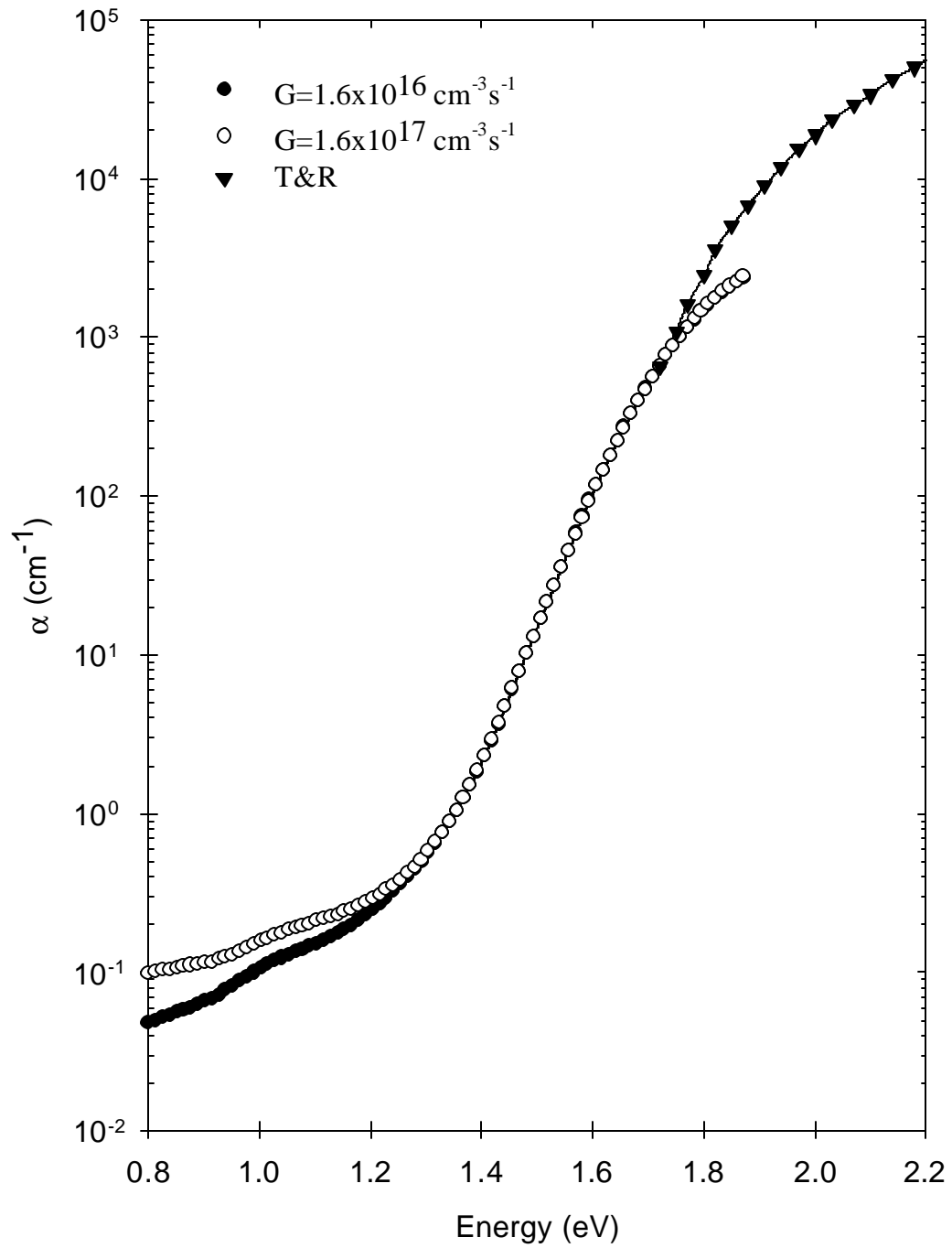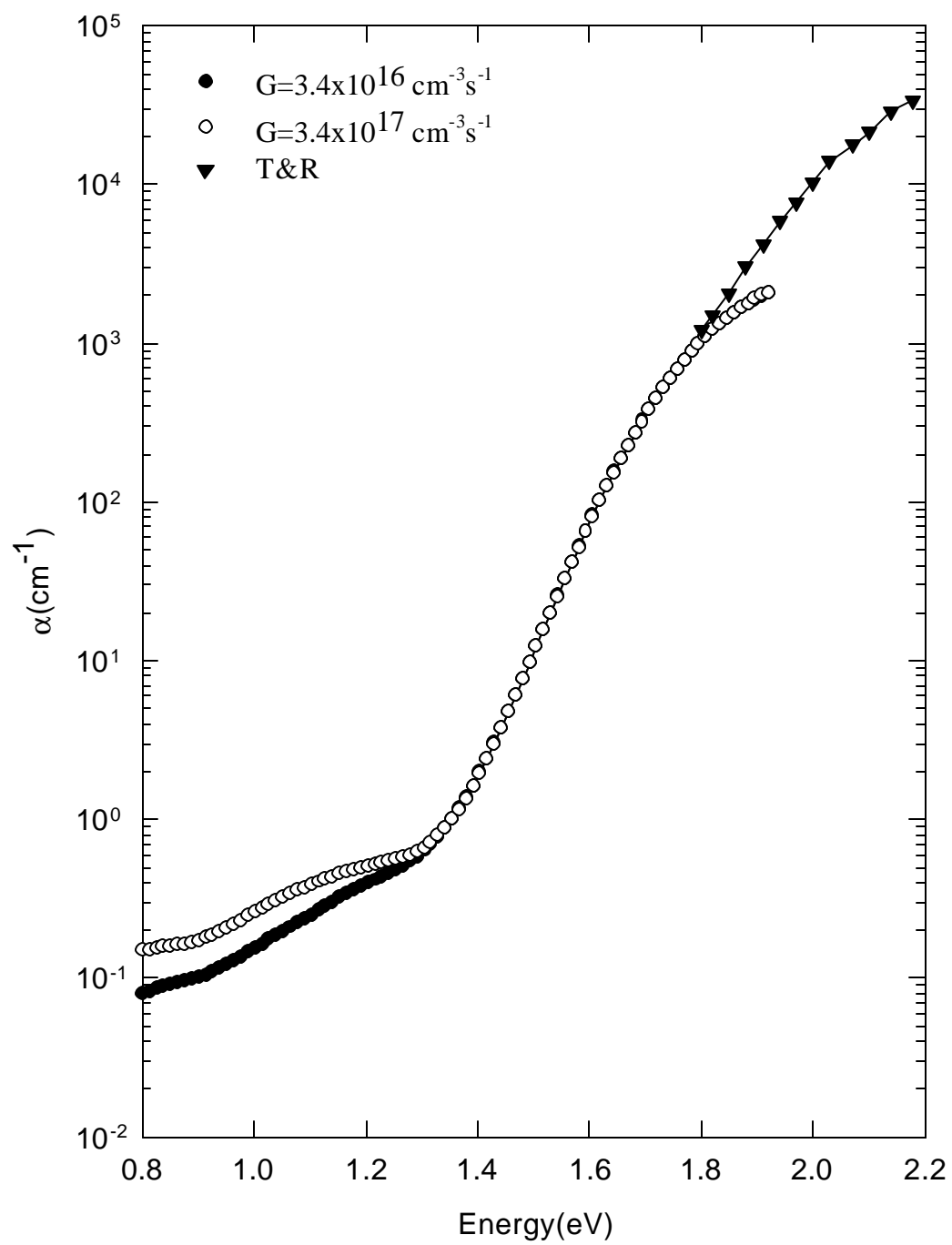
Figure 4.9.    Sub-bandgap absorption spectra of DC-GD a-Si:H sample SmartB1 at two generation rates in the annealed state.
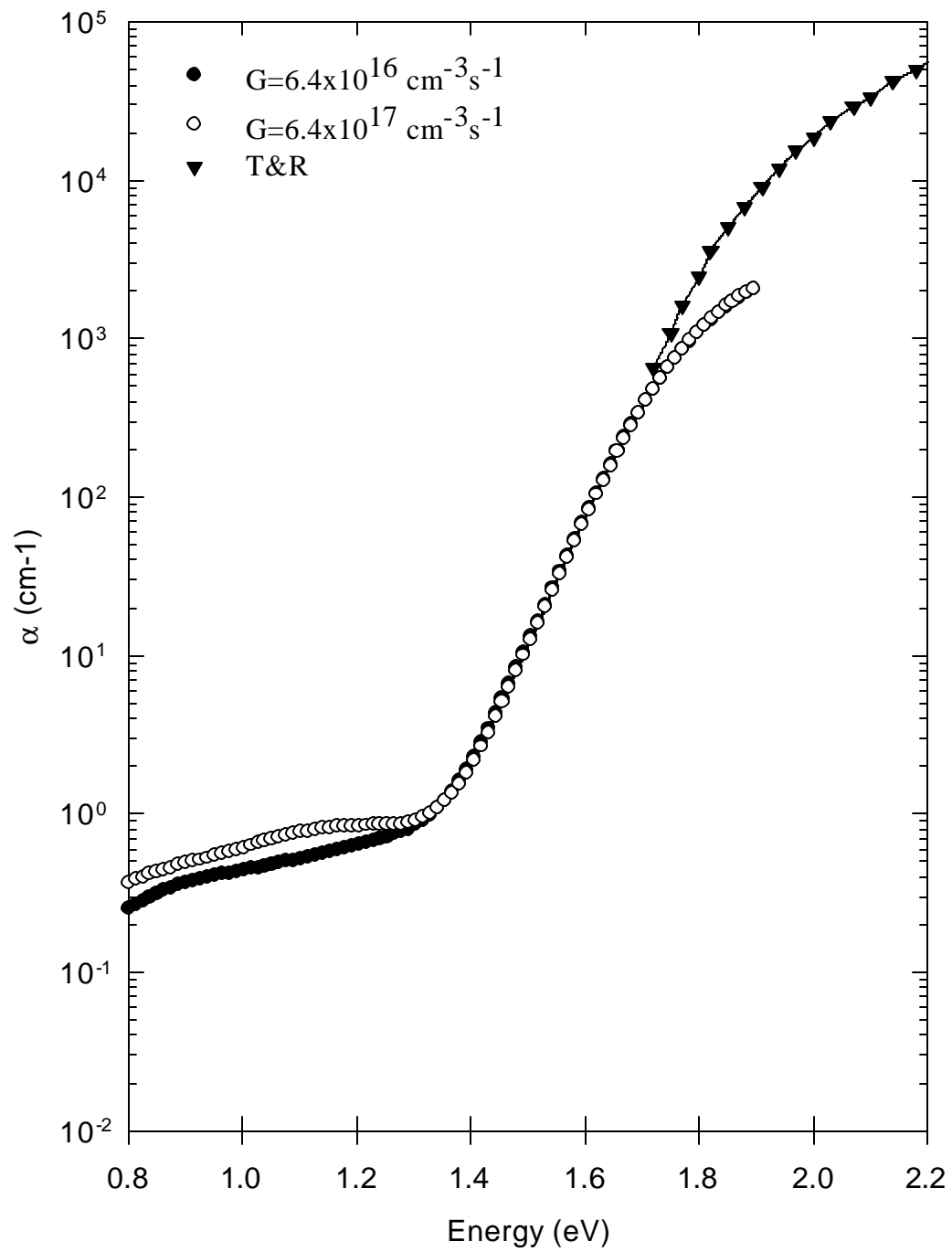
Figure 4.10.    Sub-bandgap absorption spectra of sputtered a-Si:H sample 1586T at two
generation rates in the annealed state.

around 50 meV to 60 meV. For the samples studied here, $E_{0V}$ values are summarized in Table 4.4. It is seen that all of the samples show $E_{0V}$ values in this range indicating similar degree of disorder and device quality.

As energy decreases further down to much lower energies, the sub-bandgap absorption below 1.4 eV deviates from the exponential absorption profile. All films show this behavior. However, the magnitude of the $\alpha(h\nu)$ is not the same for all films. The DBP spectrum measured at low generation rates is used for comparison of the defect levels present in the samples. The magnitude of $\alpha(h\nu)$ at 1.2 eV is shown in Table 4.4. It is clearly seen that $\alpha(1.2\ eV)$ shows variations in its magnitude from 0.25 $cm^{-1}$ to 1.0 $cm^{-1}$. This implies that the defect states below the Fermi level are not the same for these samples even though they have similar $E_{0V}$ values. If $\alpha(1.2\ eV)$ is taken as a direct consequence of the defect states, we expect a factor of 4 differences in the defect densities among the samples. It is expected that this part of the spectrum is very sensitive to the deposition condition of the sample and it can be easily modified. Finally, an estimation of these defect densities can be done using a calibration parameter obtained for the sub-bandgap absorption by Gunes et al. [65]. Again it is important to note that this calibration was obtained using the saturated light soaked DBP spectrum and ESR study carried out on the same samples. It assumes that the DBP spectrum and the ESR detect the same defects, namely neutral silicon dangling bonds. Under these assumptions, $N_{DOS}$ was estimated as $N_{DOS}\ (ESR)=\alpha(1.2\ eV)x3x10^{16}\ cm^{-3}$. For the samples studied here, $N_{DOS}$ values change from $7x10^{15}\ cm^{-3}$ to $3x10^{16}\ cm^{-3}$, which are assumed to be low defect levels as compared to the defect density of $10^{19}$-$10^{20}\ cm^{-3}$ present in unhydrogenated a-Si:H films.

In addition, the DBP spectrum at higher generation rate of bias light for the same films can be seen in the figures. For all of them, the sub-bandgap absorption spectrum shows a dependence on the bias light intensity, the $\alpha(h\nu)$ at lower energies increases with increasing generation rate. As explained previously, the increase of the $\alpha(h\nu)$ only at lower energies is due to increased electron occupied defect states above the Fermi level. Therefore, change in the $\alpha(h\nu)$ will be directly related to the defect states above the Fermi level. This will allow us to obtain qualitative information about the defects above the Fermi level for different films. The change in the sub-bandgap absorption at 1.0 eV is taken as a comparison for the intensity dependence and those values for each

sample are shown in Table 4.4. $\Delta\alpha(1.0$ eV) values are the lowest for DC-GD films and relatively higher for RF-PECVD and magnetron sputtered films.

Table 4.4     Experimental sub-bandgap absorption results of a-Si:H thin films in the annealed state where $N_{DOS}=\alpha(1.2$ eV$)x(3x10^{16})$ [65].

| SAMPLE | LJ51(R=10) | LJ70(R=0) | SmartA1 | SmartB1 | 1586T |
|---|---|---|---|---|---|
| $\alpha$ (1.2 eV) cm$^{-1}$ | 0.99 | 0.40 | 0.25 | 0.40 | 0.65 |
| $E_{0V}$ (meV) | 62 | 53 | 53 | 53 | 58 |
| $N_{DOS}$ (cm$^{-3}$) | $3.0x10^{16}$ | $1.2x10^{16}$ | $7.5x10^{15}$ | $1.2x10^{16}$ | $2.0\ x10^{16}$ |
| $\Delta\alpha(1.0$ eV) | 0.38 | 0.15 | 0.05 | 0.11 | 0.17 |
| $\mu\tau$ (G=$5x10^{16}$) | $3.0x10^{-6}$ | $4.5x10^{-6}$ | $1.7x10^{-6}$ | $5.6x10^{-7}$ | $9.1x10^{-7}$ |

Finally, the comparison of $\mu\tau$ products obtained from the steady-state photoconductivity and estimated defect density for the samples provides important conclusions about these defect levels. It is well known that both sub-bandgap absorption and steady state photoconductivity are mainly controlled by these defects. For this reason, $\mu\tau$ values measured at low generation rate (G=$5x10^{16}$ cm$^{-3}$s$^{-1}$), where mainly defects below Fermi level are active as recombination centers, and defect density estimated from low generation rate from DBP spectrum are compared. For higher defect levels, we expect lower $\mu\tau$ products. As we compare the results in Table 4.4, RF-PECVD films are more defective, but at the same time they have higher $\mu\tau$ products. It is well established that photoconductivity is a complex process and depends on the density, distribution and the nature of recombination centers. If there is only one kind of defect, such as neutral dangling bonds detected by ESR, $\mu\tau$ products and sub-bandgap absorption spectrum should be proportional. However, our results indicate that more than one kind of defect is present in the bandgap of a-Si:H. Photoconductivity and sub-bandgap absorption data provide only a qualitative understanding of a-Si:H films. In conclusion, there are more than one kind of native defect states present in the annealed

state of a-Si:H film. Differences in these defects exist due to the deposition conditions. Their effects are clearly seen in the measured photoconductivity and the sub-bandgap absorption results.

## 4.3. Staebler-Wronski Effect and Light Induced Defects

Although a-Si:H thin films are photoconductive materials, at the same time, light is a troublesome for these materials. After exposing to illumination, both dark conductivity and photoconductivity of a-Si:H thin films decrease. This phenomenon is known as the Staebler-Wronski effect (SWE) [12] and it restricts especially solar cell applications. The observed changes are generally attributed to the increase of the density of midgap defect states. Therefore, it is inevitable to investigate light induced defects and their effects on photoconductivity and sub-bandgap absorption when a-Si:H materials are studied. In this section, room temperature steady-state photoconductivity and sub-bandgap absorption measurements of a-Si:H thin films are investigated in the light soaked state. The changes in the light soaked state are compared with the corresponding annealed state results to understand the effects of SWE.

### 4.3.1. Steady-state Photoconductivity

Steady-state photoconductivity of the undoped a-Si:H films was measured after high intensity light soaking process. Since it takes very long time to investigate the long-term stability of these materials under AM1.5 light soaking (1sun $\approx$ 100 mW/cm$^2$), the high intensity degradation procedure was applied to samples [74]. In this study, the samples were exposed to white light soaking for 10 hours using the light soaking system shown in Figure 4.11. The system was established at IZTECH to study light soaked state of amorphous semiconductors. An Osram 300W ELH lamp was used as a white light source. A fan was used to cool the films during the degradation to prevent them from not being annealed during the degradation. For all the films, similar light soaking conditions were maintained during the degradation process.
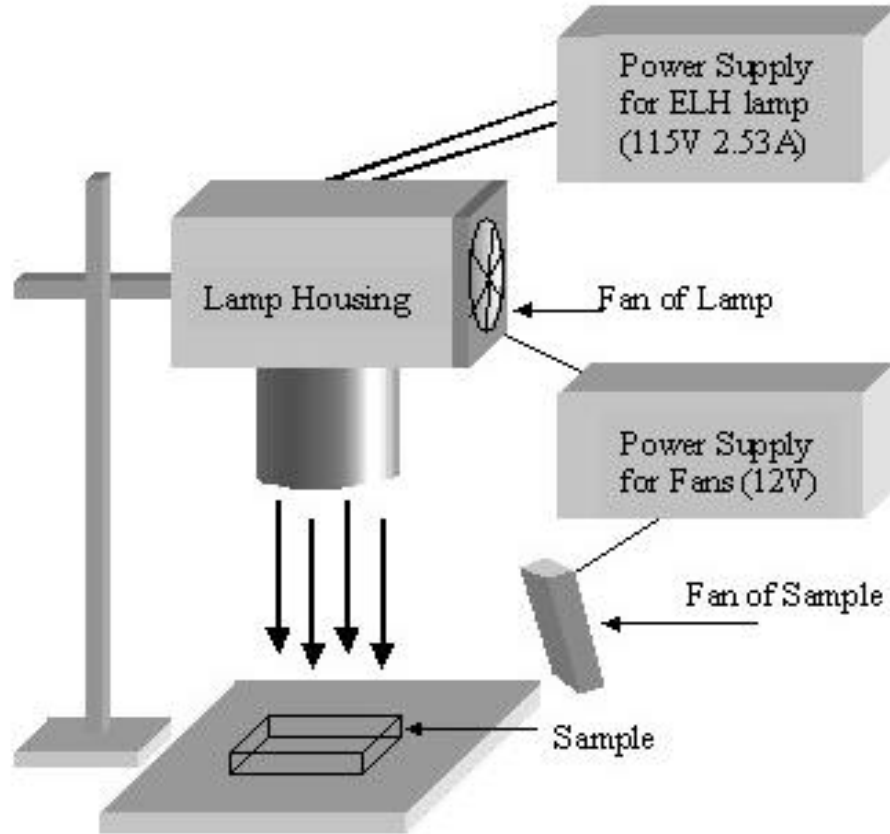
Figure 4.11.    The light soaking station used to apply high intensity light soaking to the thin films.

The results of steady state photoconductivity in the light soaked state for the sample LJ70 is shown in Figure 4.12. The Staebler-Wronski effect is significant in that $\sigma_{PH}$ decreased after light soaking. The exponent $\gamma$ also shows a slight decrease after light soaking implying that amount of decrease in $\sigma_{PH}$ are not the same as measured at high and low generation rates. Generally, the comparison of the degradation is carried out using the high G values. In this case, we will use the $\sigma_{PH}$ values measured at G=$10^{20}$ cm$^{-3}$s$^{-1}$ to quantify the degradation due to SWE. The decrease in $\sigma_{PH}$ indicates that new recombination centers, i.e. defects were created by white light illumination. Similar measurements were carried out after light soaking of the other a-Si:H films. Those results are shown in Figure 4.13, 14, 15, and 16. All a-Si:H films clearly exhibit the SWE because $\sigma_{PH}$ or $\mu\tau$ products show a significant degradation. In addition, the exponent $\gamma$ becomes almost the same for all the samples. As we summarize the results in

Table 4.5, the $\gamma$ values are around 0.84 for the samples except the sample LJ70, which has the $\gamma$ value of 0.76 after light soaking. The uniformity in the $\gamma$ values indicates that the distribution of the defect states after light soaking is very similar for the samples even though they have different annealed state characteristics. However, the magnitude of degradation in $\sigma_{PH}$ or $\mu\tau$ products shows wide range of differences. The ratio of $\sigma_{PH}(G=10^{20}cm^{-3}s^{-1})$(Annealed) / $\sigma_{PH}(G=10^{20}cm^{-3}s^{-1})$(Soaked) is the highest for LJ70. The degradation in photoconductivity is more than 1 order of magnitude. The sample SmartA1 degrades by a factor of 20 and the others show almost the similar degradation by a factor of 4. These results indicate that new defects are created by light and their effects are detected by the photoconductivity measurements. However, the exact nature and densities of light induced defect states cannot be easily accessible using these results. Their effects can only be relatively obtained using the photoconductivity results.

Figure 4.12.    Steady-state photoconductivity (a) and $\mu\tau$ product (b) versus generation rate results of RF-PECVD undiluted a-Si:H sample LJ70 in the annealed and light soaked states.
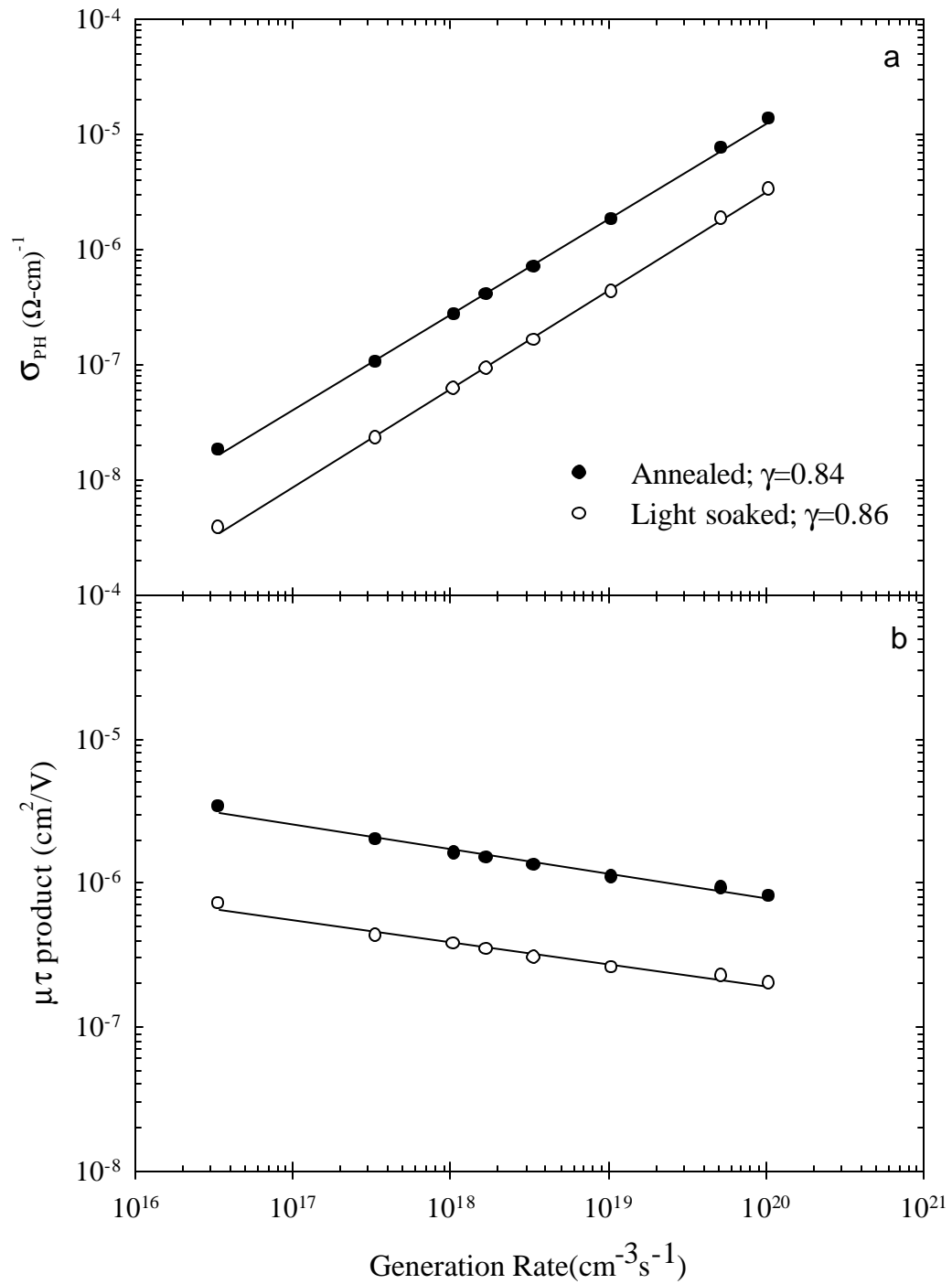
Figure 4.13.   Steady-state photoconductivity (a) and $\mu\tau$ product (b) versus generation rate results of RF-PECVD diluted a-Si:H sample LJ51 in the annealed and light soaked states.
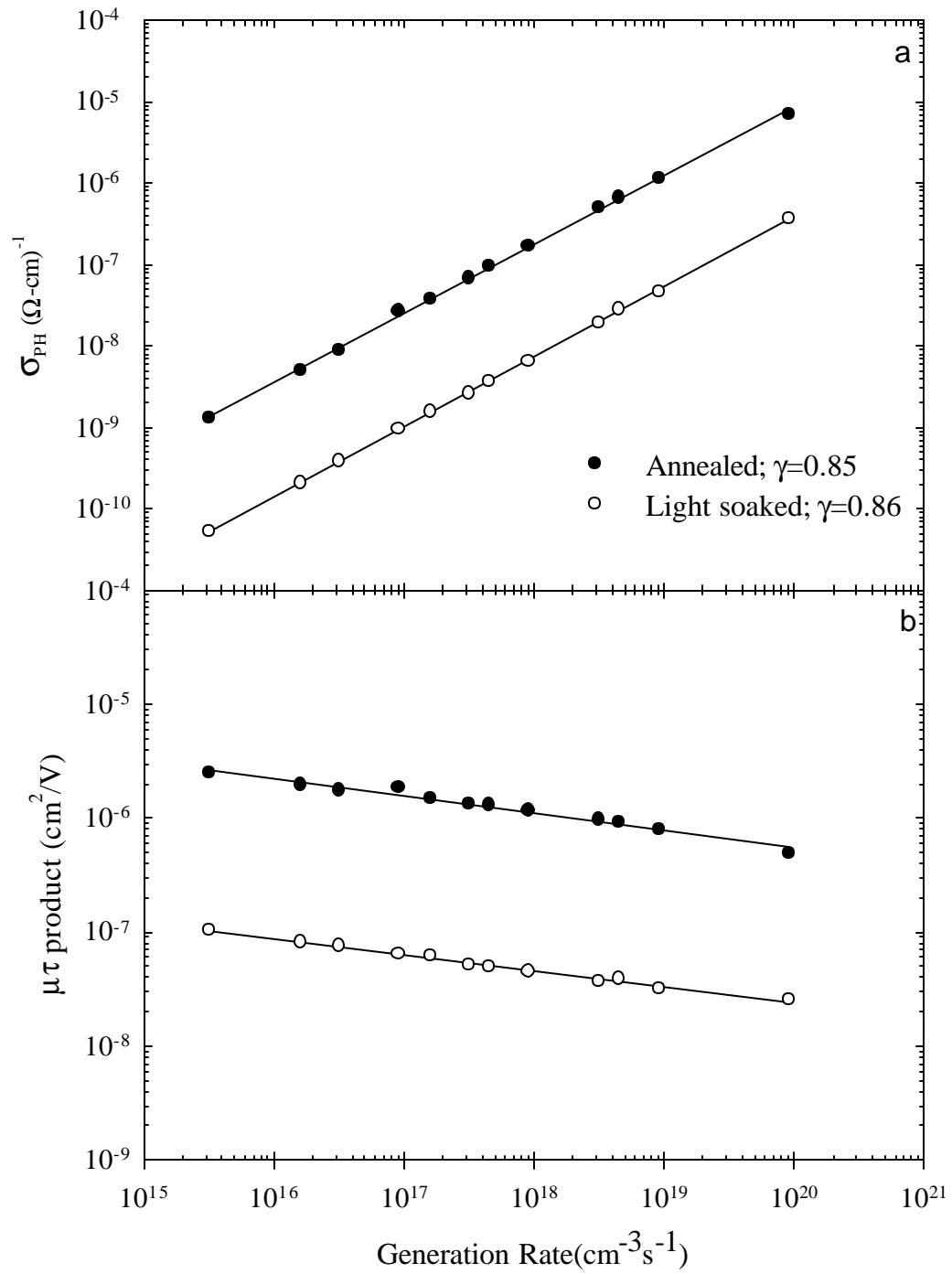
Figure 4.14. Steady-state photoconductivity (a) and $\mu\tau$ product (b) versus generation rate results of DC-GD a-Si:H sample SmartA1 in the annealed and light soaked states.
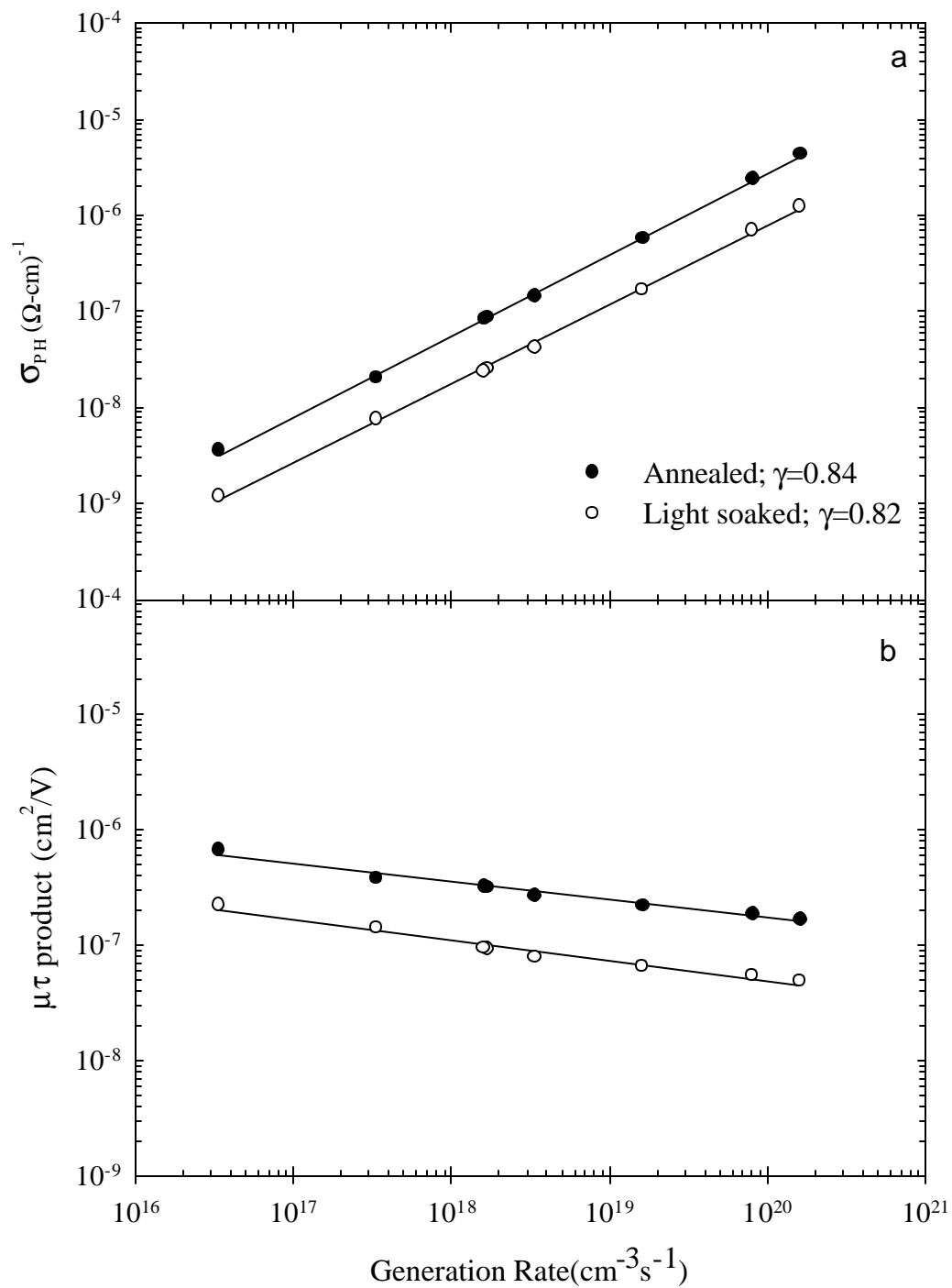
Figure 4.15.    Steady-state photoconductivity (a) and $\mu\tau$ product (b) versus generation rate results of DC-GD a-Si:H sample SmartB1 in the annealed and light soaked states.
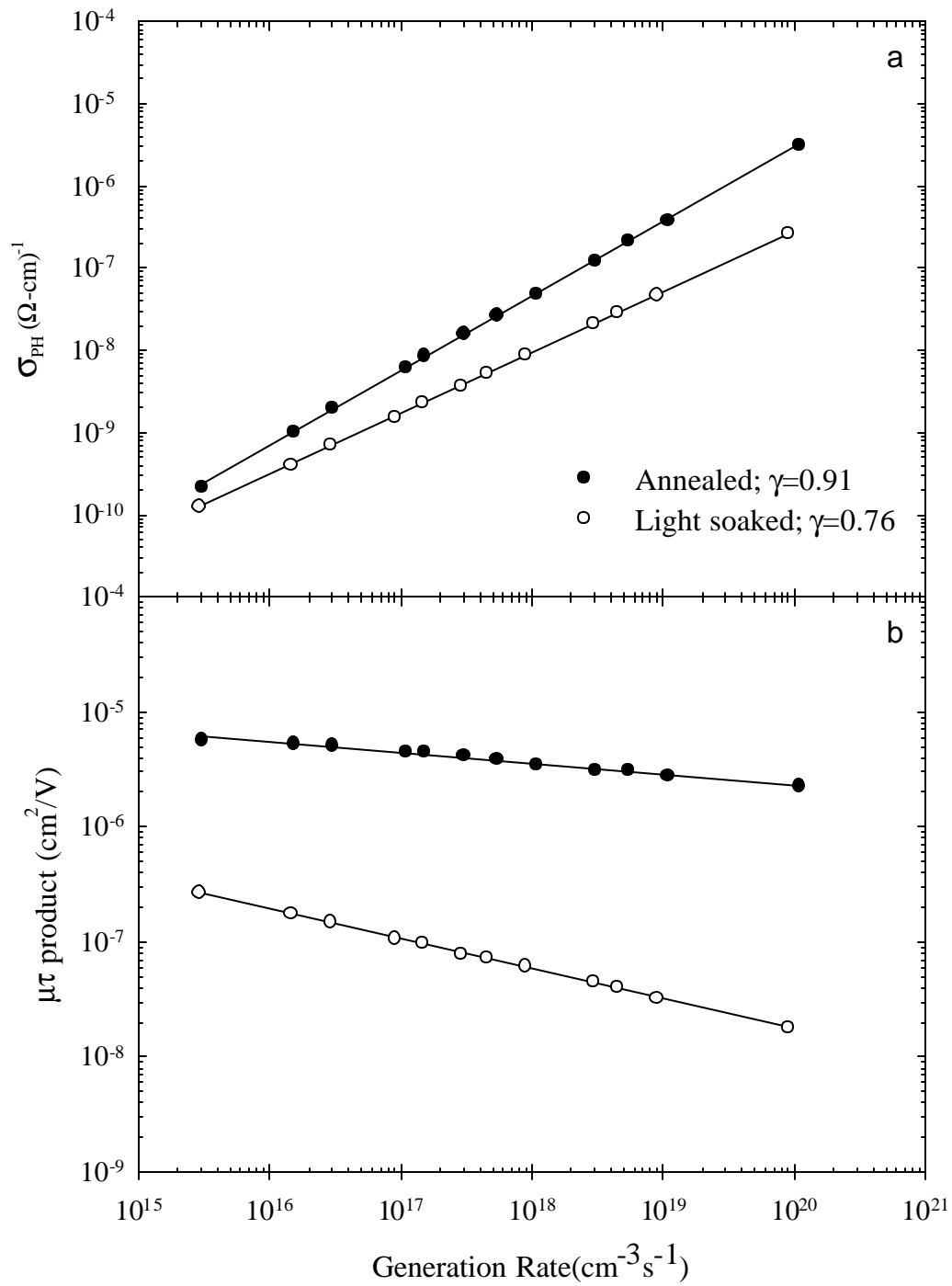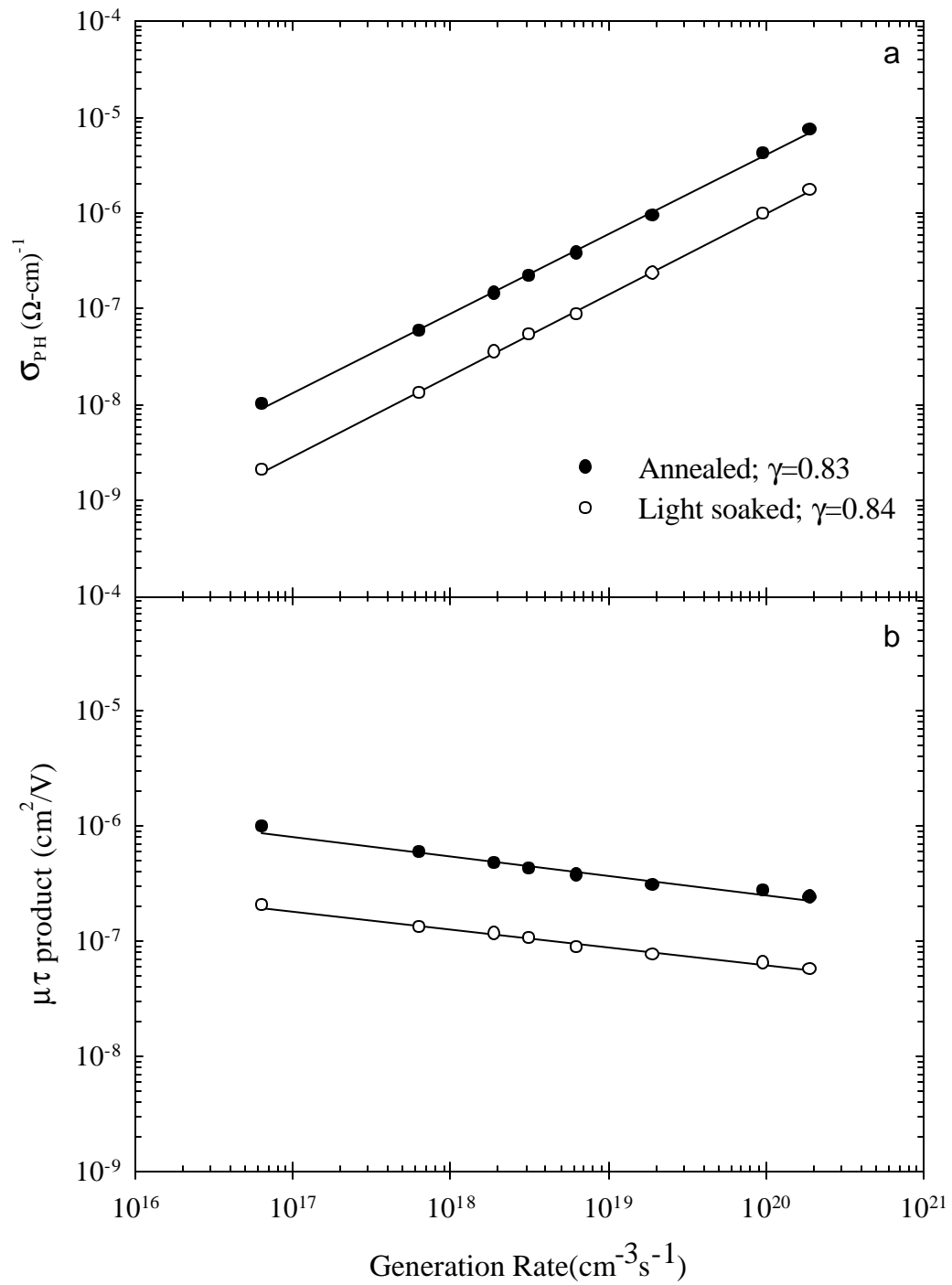
Figure 4.16.   Steady-state photoconductivity (a) and $\mu\tau$ product (b) versus generation rate results of sputtered a-Si:H sample 1586T in the annealed and light soaked states.

Table 4.5. Experimental steady-state photoconductivity results in the annealed and light soaked states

| SAMPLE | LJ51(R=10) | LJ70(R=0) | SmartA1 | SmartB1 | 1586T |
|---|---|---|---|---|---|
| $\gamma$(Annealed) | 0.84 | 0.91 | 0.85 | 0.84 | 0.83 |
| $\gamma$ (Light soaked) | 0.86 | 0.76 | 0.86 | 0.82 | 0.84 |
| $\sigma_{PH}(G=10^{20})(\Omega\text{-cm})^{-1}$ Annealed | $1.3 \times 10^{-5}$ | $3.6 \times 10^{-5}$ | $7.9 \times 10^{-6}$ | $2.8 \times 10^{-6}$ | $4.0 \times 10^{-6}$ |
| $\sigma_{PH}(G=10^{20})(\Omega\text{-cm})^{-1}$ Light Soaked | $3.1 \times 10^{-6}$ | $2.9 \times 10^{-7}$ | $3.9 \times 10^{-7}$ | $8.3 \times 10^{-7}$ | $9.6 \times 10^{-7}$ |
| $\mu\tau(G=10^{20})(cm^2/V)$ Annealed | $7.4 \times 10^{-7}$ | $2.3 \times 10^{-6}$ | $5.1 \times 10^{-7}$ | $1.8 \times 10^{-7}$ | $2.6 \times 10^{-7}$ |
| $\mu\tau(G=10^{20})(cm^2/V)$ Light Soaked | $1.8 \times 10^{-7}$ | $1.7 \times 10^{-8}$ | $2.2 \times 10^{-8}$ | $5.1 \times 10^{-8}$ | $6.1 \times 10^{-8}$ |
| $\sigma_{PH}(G=10^{20})(\Omega\text{-cm})^{-1}$ Annealed / Soaked | 4.2 | 124 | 20.3 | 3.4 | 4.2 |
| $\mu\tau(G=5 \times 10^{16})(cm^2/V)$ Annealed | $3.0 \times 10^{-6}$ | $4.5 \times 10^{-6}$ | $1.7 \times 10^{-6}$ | $5.7 \times 10^{-7}$ | $8.9 \times 10^{-7}$ |
| $\mu\tau(G=5 \times 10^{16})(cm^2/V)$ Light Soaked | $6.4 \times 10^{-7}$ | $1.4 \times 10^{-7}$ | $6.8 \times 10^{-8}$ | $1.9 \times 10^{-7}$ | $2.1 \times 10^{-7}$ |
| $\mu\tau(G=5 \times 10^{16})(cm^2/V)$ Annealed / Soaked | 4.7 | 32 | 25 | 3.0 | 4.2 |

### 4.3.2. Sub-bandgap Absorption Spectra

The Staebler-Wronski effect in a-Si:H films was presented in the previous section that the $\sigma_{PH}$ values decreased due to the creation of additional defect states in the bandgap of a-Si:H after light soaking. The effects of these light induced defect states were also detected using the sub-bandgap absorption measurements. Experimental results of DBP measurements for LJ70 both in the annealed and light soaked states are shown in Figure 4.17. As seen in this figure, the illumination on the film does not lead to any significant change in exponential tail and extended valence band states, whereas the $\alpha(h\nu)$ measured by low generation rate DBP below about 1.4 eV increases with respect to that of annealed state. This is consistent with degradation of $\sigma_{PH}$ values presented in the previous section. Since tail states are mainly due to disorder in the material, this means that light does not lead to any change in the disorder configuration of the material. However, the increase in the shoulder region indicates that illumination creates additional midgap defect states called light induced defects. This reduces photoconductivity as expected from the Staebler-Wronski effect. In addition, the DBP spectrum at higher generation rate shown in the Figure 4.17 indicates that the sub-bandgap absorption shows an increase at lower energies for increased generation rate of bias light. This implies that additional defect states above the Fermi level were also created by light soaking. Their effects can be observed by comparing the change in $\alpha(h\nu)$ at 1.0 eV. $\Delta\alpha(1.0\ eV)$ values obtained from two generation rate DBP are summarized in Table 4.5. It is interesting to see that values are larger than those of the annealed state. The sub-bandgap absorption spectra of DBD method indicate that light soaking creates new defect states located below as well as above the Fermi level. There is no change detected in the exponential absorption region indicating no change in E$_{0V}$ parameter after light soaking. The similar characterization on the other a-Si:H films studied in this thesis was carried out almost under the same conditions. The sub-bandgap absorption measurements at two different bias light intensities were carefully measured and properly normalized to the absolute $\alpha(h\nu)$ data as explained previously. These results are shown in Figure 4.18 to Figure 4.21 in the annealed and light soaked states for low generation rates. Comparison of low generation rate DBP allows us to monitor the net increase in the defect states created below the Fermi level. All samples indicate substantial increase in the $\alpha(h\nu)$ at low energies and no change in the exponential
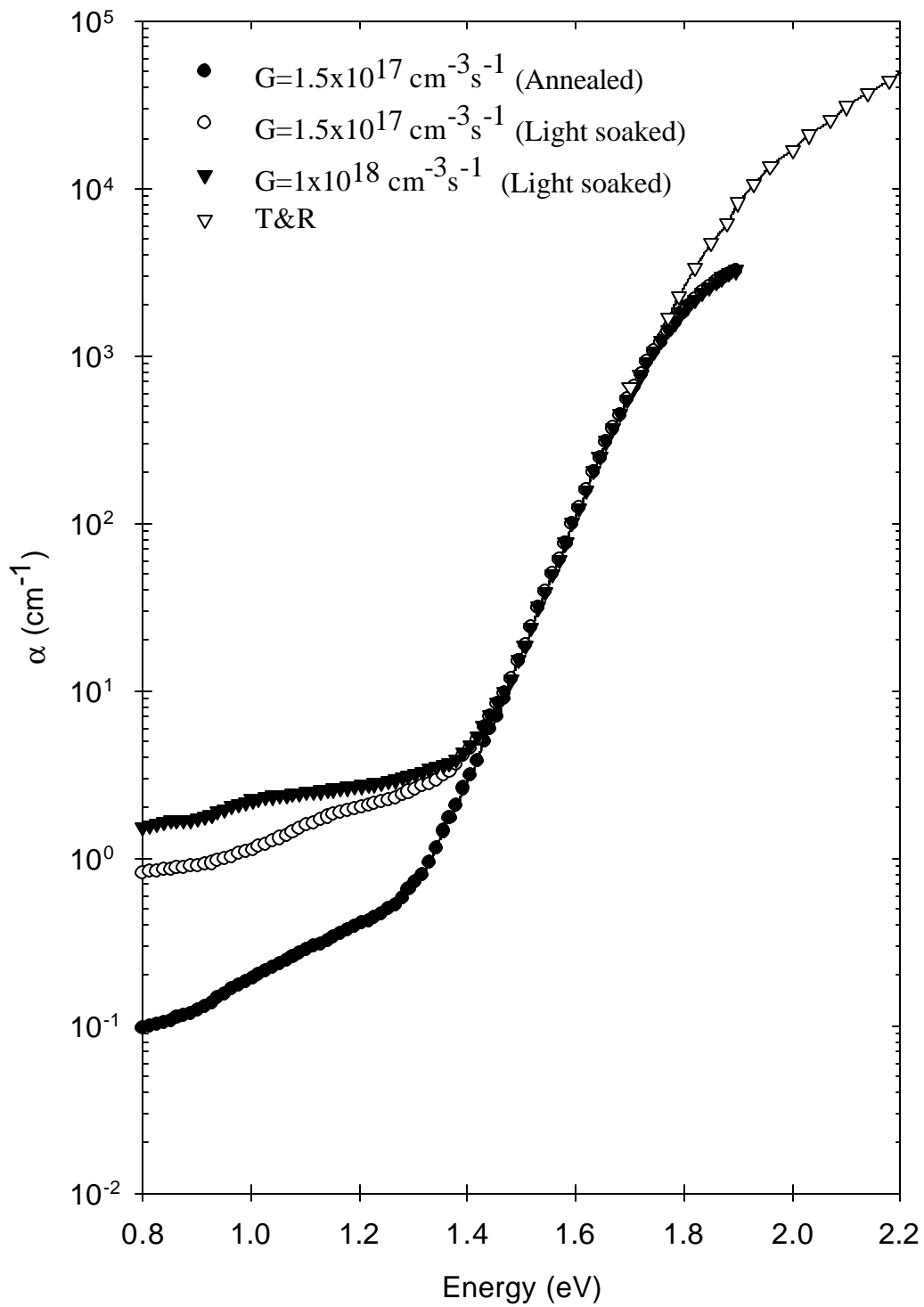
Figure 4.17.    Sub-bandgap absorption spectra of RF-PECVD a-Si:H sample LJ70 both in annealed and light soaked states.

absorption region. The amount of increase in $\alpha(h\nu)$ is taken at 1.2 eV and this is tabulated in Table 4.5. The $\alpha(1.2\ eV)$ in the light soaked state changes from 2.0 cm$^{-1}$ to 4.4 cm$^{-1}$ for the samples. The net increase in $\alpha(h\nu)$ is represented by the ratio of $\alpha(1.2\ eV)(soaked)/\alpha(1.2\ eV)(annealed)$. The ratio changes from 3.1 to 8.1 indicating that each film shows different amount of increase in defects after light soaking. However, the increase in the sub-bandgap absorption is generally consistent with the decrease of photoconductivity values as previously discussed. Estimated density of defect states, $N_{DOS}$, reaches to the level of $10^{17}$cm$^{-3}$ after light soaking. This is consistent with the values reported in the literature [69].

In addition to the increase of sub-bandgap absorption spectrum measured at low generation rate, there is also notable increase in the intensity dependence of DBP spectra. The $\Delta\alpha(1.0\ eV)=\alpha(1.0\ eV)(highG)-\alpha(1.0\ eV)(lowG)$ increases after light soaking. All samples exhibit an increase in $\Delta\alpha(1.0\ eV)$, where it changes from 0.25 cm$^{-1}$ to 1.0 cm$^{-1}$, which are higher than respective annealed state values. The meaning of the increase in $\Delta\alpha(1.0\ eV)$ is that higher density of new defects above and below the Fermi level is created by light. Their density is larger than the native defects present in the annealed state as seen from $\Delta\alpha(1.0\ eV)$ and $\alpha(1.2\ eV)(Soaked)$ data. How eVer, there is no direct correlation between the increase of $\alpha(1.2\ eV)$ or estimated density of defects, NDOS, and the decrease of photoconductivity. For this reason, the results are compared. It is found that the ratio of $\alpha(1.2\ eV)(soaked)/\alpha(1.2\ eV)(annealed)$ is not proportional to the ratio of $\mu\tau(5x10^{16})(annealed)/\mu\tau(5x10^{16})(soaked)$. Similar comparison is also valid for the high generation rate data of photoconductivity. Therefore, it is not possible to directly compare the amount of degradation in $\mu\tau$ products or $\sigma_{PH}$ with the net increase in the sub-bandgap absorption. These results indicates that more than one kind defect, generally assumed neutral silicon dangling bonds detected by ESR, are created by light soaking which cause unproportional change in photoconductivity and sub-bandgap absorption.
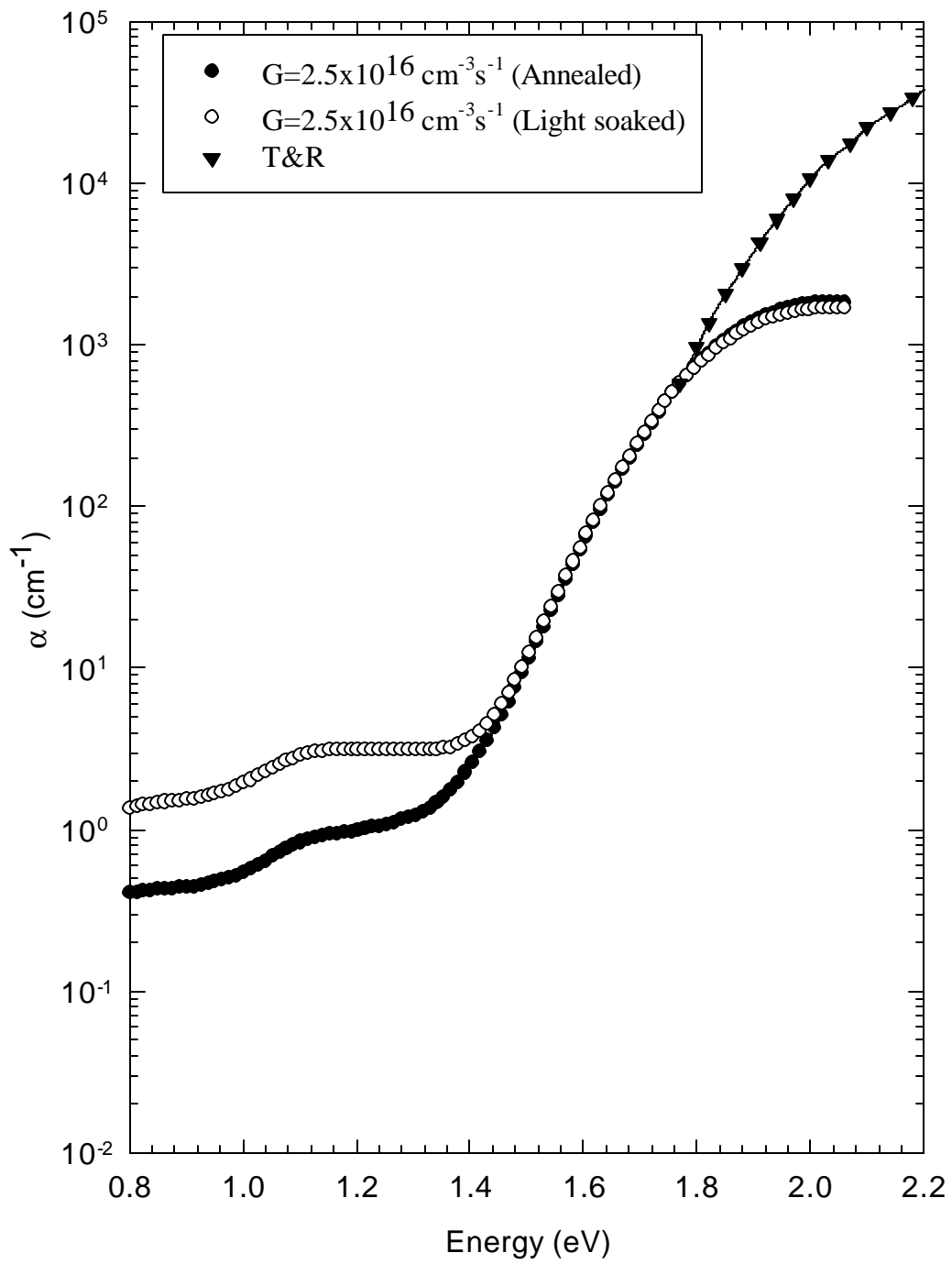
Figure 4.18.    Sub-bandgap absorption spectra of RF-PECVD a-Si:H sample LJ5l both in annealed and light soaked states.
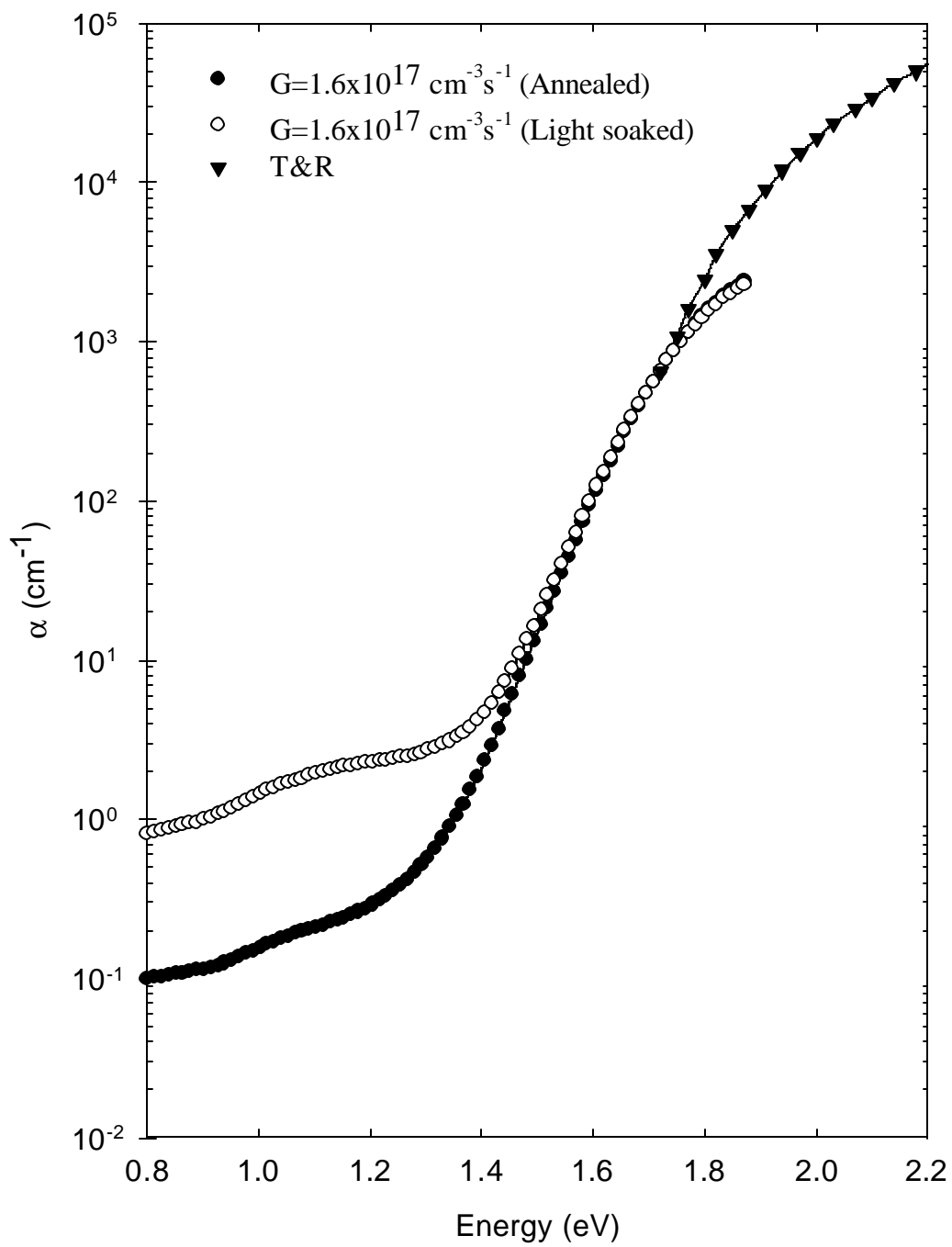
Figure 4.19.    Sub-bandgap absorption spectra of DC-GD a-Si:H sample SmartA1 both in annealed and light soaked states.
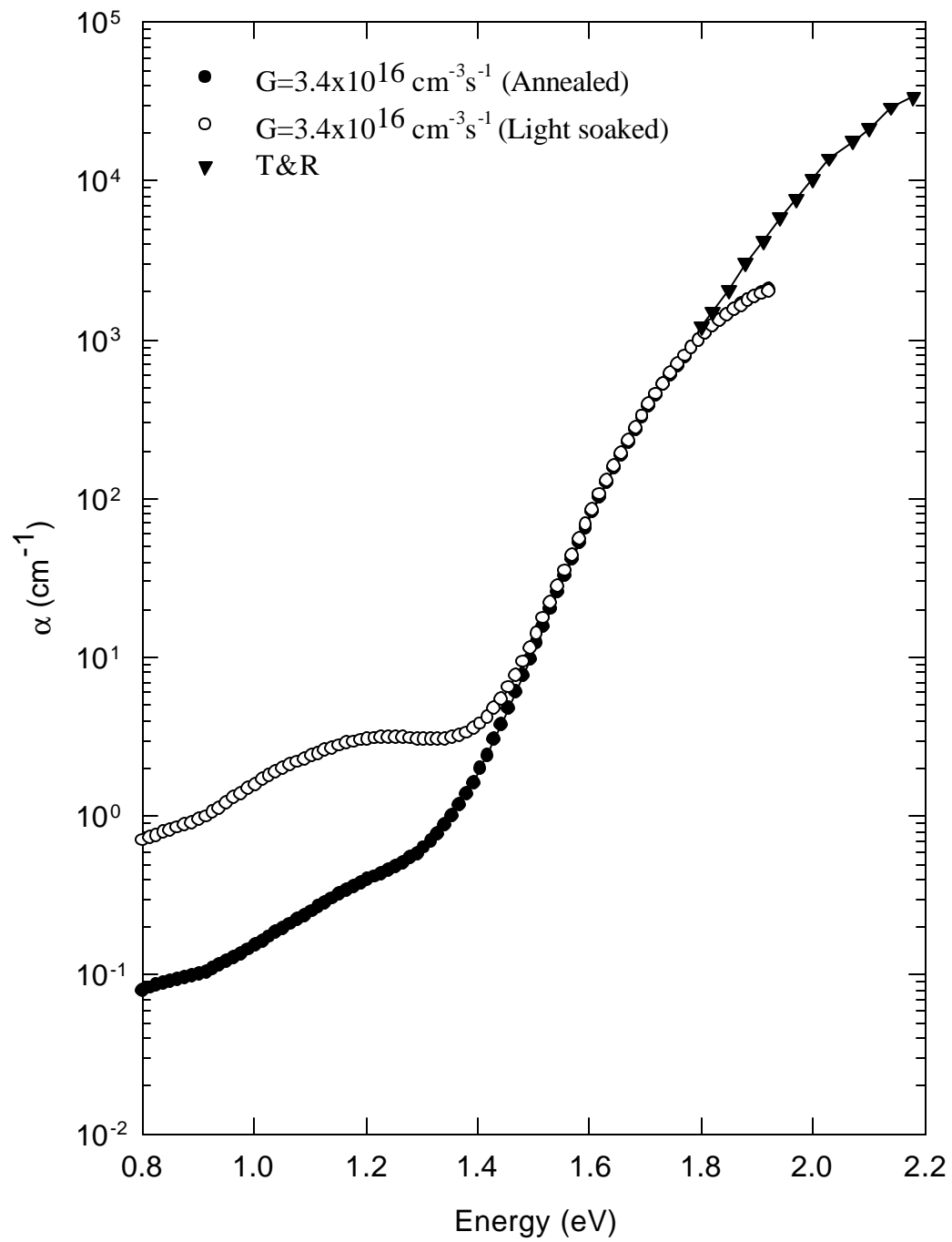
Figure 4.20.    Sub-bandgap absorption spectra of DC-GD a-Si:H sample SmartB1 both in annealed and light soaked states.
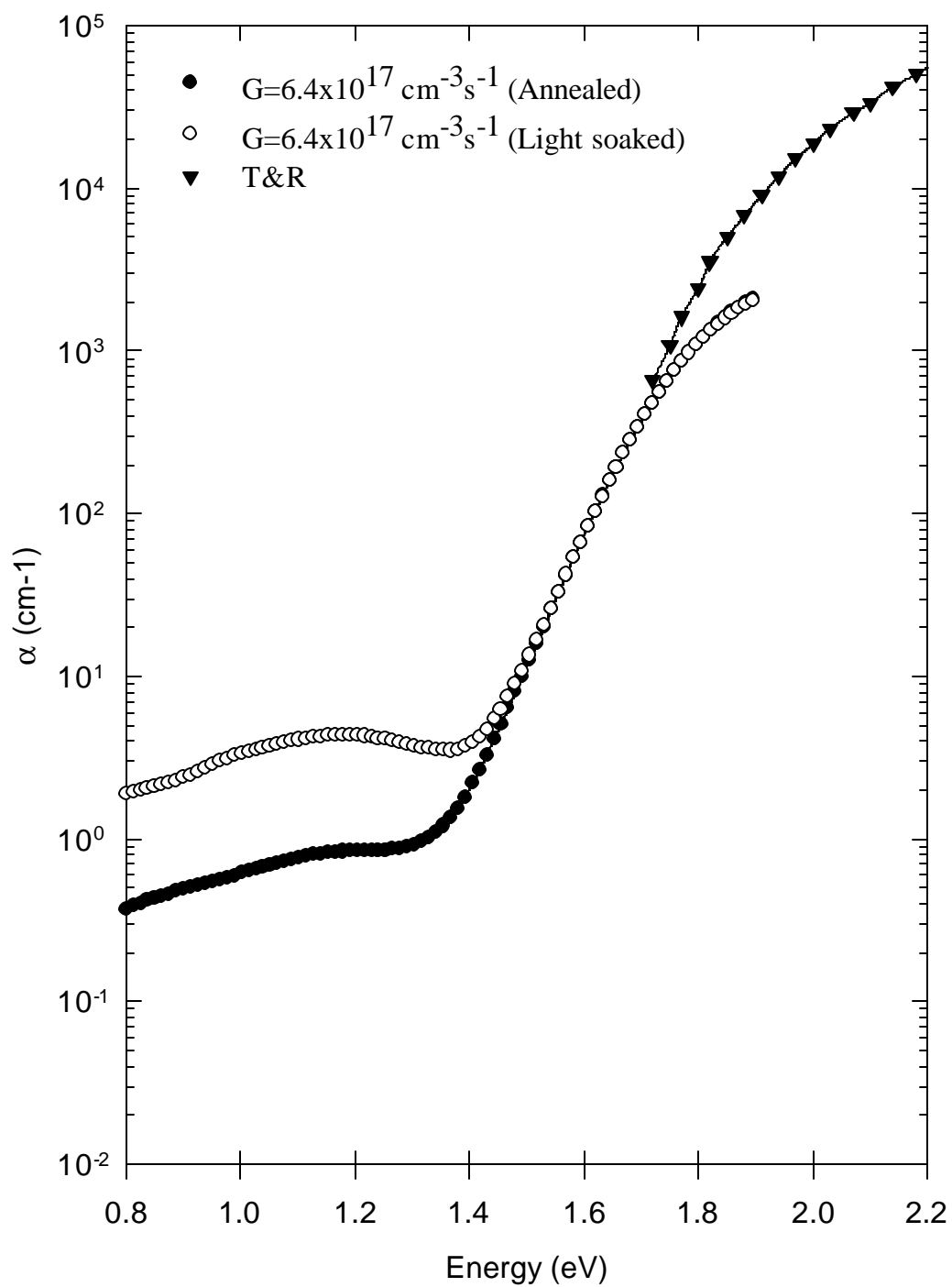
Figure 4.21. Sub-bandgap absorption spectra of sputtered a-Si:H sample 1586T both in annealed and light soaked states.

Table 4.6    Experimental sub-bandgap absorption results in the annealed and light soaked states where $N_{DOS}=\alpha(1.2\ eV)x(3x10^{16})$ [65]

.

| SAMPLE | LJ51(R=10) | LJ70(R=0) | SmartA1 | SmartB1 | 1586T |
|---|---|---|---|---|---|
| $\alpha$ (1.2 eV) cm$^{-1}$ (Annealed-lowG) | 0.99 | 0.40 | 0.25 | 0.40 | 0.65 |
| $\alpha$ (1.2 eV) cm$^{-1}$ (Light soaked-lowG) | 3.1 | 2.0 | 2.1 | 3.1 | 4.4 |
| $\alpha$ (1.2 eV) cm$^{-1}$ Soaked / Annealed | 3.1 | 5.0 | 8.4 | 7.8 | 6.8 |
| $N_{DOS}$ (cm$^{-3}$) (Annealed) | $3.0x10^{16}$ | $1.2x10^{16}$ | $7.5x10^{15}$ | $1.2x10^{16}$ | $2.0x10^{16}$ |
| $N_{DOS}$ (cm$^{-3}$) (Light soaked) | $9.3x10^{16}$ | $6.0x10^{16}$ | $6.3x10^{16}$ | $9.3x10^{16}$ | $1.3x10^{17}$ |
| $\Delta\alpha(1.0\ eV)$ cm$^{-1}$ (Annealed) | 0.38 | 0.15 | 0.05 | 0.11 | 0.17 |
| $\Delta\alpha(1.0\ eV)$ cm$^{-1}$ (Light soaked) | 0.67 | 1.0 | 0.25 | 0.31 | 0.87 |
| $\sigma_{PH}(G=10^{20})(\Omega\text{-cm})^{-1}$ Annealed / Soaked | 4.2 | 124 | 20.3 | 3.4 | 4.2 |
| $\mu\tau(G=5x10^{16})(cm^2/V)$ Annealed / Soaked | 4.7 | 32 | 25 | 3.0 | 4.2 |

## 4.4. Conclusion

In this chapter, the dark conductivity, the steady-state photoconductivity and the dual beam photoconductivity techniques described in chapters 2 and 3, respectively, were used to investigate a-Si:H thin films prepared by various deposition methods. In the annealed state, dark conductivity measurements provided the position of the dark Fermi level of a-Si:H samples indicating that these samples are nearly intrinsic materials. From the room temperature dark conductivity values, it can be seen that a-Si:H is very resistive in its undoped state in dark. However, under high intensity light, the conductivities of the samples increased by 5 to 6 orders of magnitude meaning that a-Si:H is a good photoconductor. Steady state photoconductivity results also presented the information about recombination kinetics of a-Si:H. The $\gamma$ values of the films are nearly the same and $0.8 < \gamma < 1.0$ showing the recombination path passes through the midgap defect states. In addition, similar defect distributions exist in these films. Both photoconductivity and $\mu\tau$ product values are near to that of device quality a-Si:H films reported in the literature and these can vary depending on the deposition conditions. Since steady state photoconductivity is a limited measurement to understand the nature and the distribution of midgap defect states, sub-bandgap absorption measurements using dual beam photoconductivity (DBP) technique were also carried out on these films. The results of DBP indicate that a-Si:H thin films in this study involves midgap defect states in addition to its disorder structure which creates valence band tail states as well as extended states. The characteristic energy of valence band tail states is in the rage of 50 meV and 60 meV meaning that a-Si:H films used in this study are device quality materials. The density of the midgap defect states was estimated using $\alpha$(1.2 eV) and a calibration constant. It was found to be on the order of $10^{16}$ cm$^{-3}$ in the annealed state and thereby the films are suitable for device applications. The advantage of DBP, intensity dependence of sub-bandgap absorption, was also investigated for these samples by choosing a reference energy, 1.0 eV. It was shown that as the generation rate of bias light increases sub-bandgap absorption also increases due to splitting of quasi-Fermi levels and thereby due to the contribution of defect states above the Fermi level.

In the light soaked state, a-Si:H samples showed a degradation in photoconductivity as expected from the Staebler-Wronski effect. The order of degradation differs one film to another according to the samples. The $\gamma$ values also

changed slightly except undiluted RF-PECVD sample. Nearly same γ values imply that similar defect distributions exist after light soaking. The increase in sub-bandgap absorption and invariant exponential absorption in all the samples show that light soaking creates new defect states in the midgap but does not change the disorder of these materials. The density of defect states is on the order of $10^{17}$ cm$^{-3}$ after light soaking. However, the order of degradation in photoconductivity and increase in sub-bandgap absorption are not correlated well. This implies that one type of defect is not adequate to explain the results and midgap defect states. The intensity dependence of sub-bandgap absorption at 1.0 eV showed that the amount of increase in sub-bandgap absorption increased for all the samples after light soaking. Hence, new defect states were created by light both above and below the Fermi level.

According to the results, DBP gives reliable absorption coefficient values at low absorption region. For high absorption region, the conditions and assumptions have to be satisfied as described in both chapter 3 and chapter 4. In addition, the advantage of DBP, intensity dependence of DBP spectrum, can be used to detect more gap states. This allows that a wider energy range in the bandgap of these films can be investigated. In other words, defect states above Fermi level as well as below can be detected. Therefore, DBP is a convenient and a useful technique to measure sub-bandgap absorption and analyze the midgap defect states.

# CHAPTER 5

# DISCUSSION AND CONCLUSIONS

This thesis study covers the investigation of hydrogenated amorphous thin films (a-Si:H) that are widely used in electronic applications, especially photovoltaics. Although a-Si:H has about three decades history, a-Si:H is still needed to be investigated and improved since it can not be fabricated uniquely and it shows deficiency under illumination as a photoactive material, which is the Staebler-Wronski effect [12]. In this thesis study, undoped hydrogenated amorphous silicon (a-Si:H) thin films prepared by different deposition techniques such as RF-PECVD, DC-Glow discharge, and RF-Magnetron sputtering have been investigated in detail. Since these films are photosensitive materials, the investigation was carried out both in the annealed and light soaked states. Dual beam photoconductivity (DBP) technique was established as the main goal of this thesis to acquire reliable sub-bandgap absorption coefficient spectra of amorphous semiconductors. Some assumptions and procedures were used to reach the reliable spectra described in chapter 2 and 3. These spectra were obtained for a-Si:H thin films here and used to analyze their optoelectronic properties, and especially to investigate nature and the density of midgap defect states in the bandgap of a-Si:H. Dark conductivity as function of temperature and steady-state photoconductivity versus generation rate at room temperature measurements were used as supportive techniques to characterize these materials.

In the annealed state, undoped a-Si:H films were kept in a vacuum at 150 $^{o}$C for a few hours and dark conductivity was measured as a function of temperature. The slope of dark conductivity versus 1000/T, which is Arrhenius plot, graph gives the position of dark Fermi level with respect to the conduction band mobility edge called activation energy. The activation energies of the samples are between 0.9 eV and 1.1 eV. Even if some samples are prepared by the same system, the activation energies can vary according to substrate temperatures and H dilution ratio. Samples prepared by the same DC-GD system show differences due to their different substrate temperatures because the substrate temperature directly affects the hydrogen content, microstructure and bandgap of the a-Si:H films. In fact, changes in these parameters lead to difference in the density of midgap defect states, which strictly affect the position of dark Fermi

level. Diluted RF-PECVD sample has higher activation energy than undiluted RF-PECVD sample as expected since H dilution widens the bandgap. The optical bandgap of undoped a-Si:H films are generally between 1.7 eV-1.8 eV. It is approximately defined to be the energy of $\alpha(E_g)$ =1000 cm$^{-1}$. Mobility gap is assumed to be 0.1 eV larger than the optical gap [69]. Therefore, the samples used in this study exhibit activation energies around 0.90 eV, which indicates that the samples are intrinsic and dark Fermi level lies in the middle of the bandgap. In addition, the dark conductivity values at room temperature are on the order of $10^{-11}$-$10^{-12}$ $(\Omega$-cm$)^{-1}$ These values are consistent with the data reported in the literature and indicate that undoped a-Si:H is a perfect resistor in the dark.

Steady-state photoconductivity measurements are used to understand transport and recombination kinetics of photogenerated carriers. Due to continuous distribution of gap states in a-Si:H, the recombination kinetics is different from that in crystalline silicon. All gap states between two quasi Fermi levels, which establish the distribution of carriers in the gap states, are attributed to recombination centers [72,73]. Carriers captured by these recombination centers recombine with other carriers and most recombination traffic passes through these centers, which govern the lifetimes of carriers. Photoconductivity is determined by the density of these recombination centers, their occupancies and capture cross sections. These gap states can be probed by steady-state photoconductivity at room temperature using monochromatic light with energy greater than the optical gap. This leads to the excitation of free electrons from the valence band to the conduction band. After a certain time, referred to lifetime of carriers, excited free electrons recombine with free holes either directly in the valence band (bimolecular recombination) or through the midgap defect states (monomolecular recombination). Changes in light intensity of monochromatic light is reflected as changes in recombination mechanism. The increase in illumination causes an increase in the free carrier densities and thereby the movement of electron and hole quasi Fermi levels towards their respective band edges. More recombination traffic takes place. Therefore, steady state photoconductivity depending on the illumination intensity gives information about the recombination processes.

In this study, steady-state photoconductivity for different intensities was measured for all films in the annealed state using monochromatic light. Steady state photoconductivity in a-Si:H exhibits a non-integer power law dependence on light

intensity, i.e generation rate ($s_{PH} = CG^?$) where $\gamma$ is the exponent explained in chapter 2. The exponent $\gamma$ depends on whether main recombination process takes place in the valence band or through the midgap defect states and is $1/2 < \gamma < 1$. For samples in this study, the $\gamma$ values are in the range of 0.8-1.0. In other words, ? values are close to unity for all samples. Therefore, $\gamma$ values show that monomolecular recombination is dominant for undoped a-Si:H films. For all the films, the recombination path passes through the midgap defect states. In other words, the sub-linear dependence of photoconductivity on light intensity is a direct consequence of the continuous distribution of gap states. Since quasi Fermi levels split when light intensity increases, higher lying states are converted to recombination centers. This increases the density of recombination centers as explained by the Simmons-Taylor statistics [72,73] and reduces the carrier lifetimes. In the annealed state, photoconductivity and $\mu\tau$ product values are consistent with the generally reported magnitudes, which are in the range of the device quality a-Si:H reported in the literature [69]. In addition, photoconductivity increases about 6 orders of magnitude with respect to dark conductivity implying that a-Si:H is extremely photosensitive material and useful for optoelectronic applications.

Conventional d.c. measurement devices are limited to perform very low-level measurements. Since the density of midgap defect states are lower than the extended states about 6 orders of magnitude, it is not possible to detect these states by d.c. measurement methods. That is one of the reasons why steady state photoconductivity measurements are limited to energies higher than the bandgap of a-Si:H. Instead, a.c measurements like lock-in technique should be used to identify midgap defect states. Unlike steady state photoconductivity, sub-bandgap absorption spectrum is due to absorption of photons with energies lower than the bandgap of a-Si:H. It gives further information about the midgap defect states. Electrons excited from these defect states into the conduction band by absorption of low energy photons, which are obtained varying the monochromatic chopped (or a.c.) light, can be detected by measuring sub-bandgap photocurrent. Dual beam photoconductivity (DBP) spectroscopy was established as a main goal of this thesis to obtain reliable absorption coefficient spectrum of a-Si:H films. In this thesis study, sub-bandgap absorption measurements were carried out using DBP for different generation rates as described in detail in chapter 3. The obtained photocurrent spectra of a-Si:H films were matched to the corresponding absorption coefficient, $\alpha(h\nu)$, values of T&R measurements. These sub-

bandgap absorption spectra give information about valence band tail states and midgap defect states. Using the same system, the flux calibration of white light and transmission measurements on the a-Si:H films were also performed. Flux data were used to remove the energy dependence of flux, which affects the sub-bandgap absorption spectra. Transmission measurements were used to obtain thickness of the films.

In the annealed state, all the samples were measured for at least two bias light intensities. The sub-bandgap absorption spectra of a-Si:H films show deviations from T&R spectra above bandgap energy region due to unsatisfied assumptions of the technique as described in chapter 2. At normalization energy and at lower energies, there is a smooth transition in the $\alpha(h\nu)$ spectrum from the T&R data to that of DBP. The accuracy of DBP spectrum depends on the reliable absolute $\alpha(h\nu)$ values around the normalization energy. The $\alpha(h\nu)$ measured by the T&R method has difficulties at lower energies due to very large interference fringes that appear in the spectrum. The normalized DBP spectra has accuracy limit less than 10% in the absolute scale. To obtain more accurate normalization procedure, we extended our study in hydrogenated microcrystalline silicon thin films ($\mu c$-Si:H) and DBP spectra were normalized to the absolute $\alpha(h\nu)$ spectra obtained by the photothermal deflection spectroscopy (PDS). We have found out that PDS spectra give absolute and reliable $\alpha(h\nu)$ spectra down to 1.0 eV and there is a perfect overlap in the $\alpha(h\nu)$ spectra obtained by DBP and PDS after normalization [75]. Therefore, normalization of DBP spectrum to the T&R values as done in this thesis are reliable within the limit of experimental error when necessary preconditions are satisfied. The characteristic valence band tail energies of a-Si:H films vary since these are determined by the disorder in the materials and a narrow valence band tail gives a small characteristic energy. For a-Si:H films in this study, valence band tail slopes are between 50-60 meV that can be interpreted as device quality films. Below the tail states, $\alpha(h\nu)$ values are related to midgap defect states and henceforth spectrum shows a shoulder. For low generation rate values, sub-bandgap absorption spectrum is mainly due to midgap states below the dark Fermi level. Since the density of these midgap states can be deduced from the $\alpha(h\nu)$ values by choosing a single energy [65], it gives quantitative information about the midgap states as well as qualitative consequences. It was assumed that sub-band gap absorption below tail states come from the same type of defect states, neutral silicon dangling bonds. The estimated densities of midgap defect states are close to $10^{16}$ cm$^{-3}$ for a-Si:H films used in this

study in the annealed state. This is in the range of accepted values for the device quality a-Si:H films. Some films shows higher defect density whereas they have higher photoconductivity than the others, which imply that there is no direct correlation between the photoconductivity and sub-bandgap absorption. Hence, the densities of midgap states do not follow the photoconductivity results. If there were one type of defect, higher defect density would produce lower photoconductivity (or lower $\mu\tau$ product) in these films. Therefore, there should be different types of defect states as well as neutral dangling bonds in these materials below and above the Fermi level and these states can directly affect the sub-bandgap absorption and photoconductivity. These can be charged dangling bonds described both by the previous defect models [35-37,69]. An interesting feature of DBP was also applied to a-Si:H samples, which is to use different bias light intensities. When the generation rate is further increased, quasi Fermi levels moves toward the band edges. Then defects above the Fermi level become occupied. Changes in their occupation affect both steady-state photoconductivity and sub-bandgap photoconductivities. The DBP spectrum at higher generation rate is directly influenced by these changes. For all samples, we have detected an increase in the sub-bandgap spectrum at lower energies photon energies. That means that only defect levels contributed to the sub-bandgap photoconductivity due to optical transition of electrons from occupied defect states to the conduction band edge. This feature of DBP can be used to obtain additional information about the midgap defect states lying both above and below the dark Fermi level. This is an advantage of DBP method over the other sub-bandgap absorption methods such as CPM, which is only sensitive to the occupied defect states the dark Fermi level.

In the light soaked state, $\sigma_{PH}$ values decrease in all samples as expected by the Staebler-Wronski effect. The $\mu\tau$ product values also decrease indicating that new recombination centers, defect states, are created by light soaking. The magnitude of degradation in $\sigma_{PH}$ and $\mu\tau$ product varies according to the samples. The $\gamma$ values of a-Si:H films change slightly but they are nearly same which means that similar defect distributions exist in the bandgap after light soaking.

The creation of defect states can also be observed in sub-bandgap absorption by an increase in $\alpha(h\nu)$ about a factor of between 3-10. This increase corresponds to a density of defect states of about $10^{17}\,cm^{-3}$. However, $E_{0V}$ values do not show any change since the disorder of the structure does not change significantly. According to the

results, the increases in density of defect states are not directly correlated to photoconductivity results since while some films shows less degradation in photoconductivity they can exhibit large increases in density of states. This can be due to difference in defect distributions and different types of defects as previously mentioned. Using different generation rate also results in an increase in sub-bandgap absorption in the light soaked state. However, this increase is higher than the annealed state value for all films used this study, which is defined as $\Delta\alpha$(1.0 eV) in chapter 4. Increasing bias light intensity results in the splitting of quasi Fermi levels and the defect states above the Fermi level can be observed. Since the density of states above increases as well as below the Fermi level after light soaking, which was reflected in the $\Delta\alpha$(1.0 eV) values and light soaked $\Delta\alpha$(1.0 eV) is larger than annealed $\Delta\alpha$(1.0 eV).

The DBP technique was also applied to hydrogenated microcrystalline silicon thin films [75], which were not mentioned in this thesis. These spectra were compared with their respective constant photocurrent method (CPM) and photothermal deflection spectroscopy (PDS) spectra to see only the reliability of DBP spectra. According to results, the low generation rate DBP spectra match with CPM spectra at sub-bandgap absorption region where both CPM and DBP are unlike from the PDS as expected. In addition, DBP spectra show deviations from the others at high energy region since the assumptions described in chapter 2 are not satisfied.

In conclusion, both in the annealed and light soaked state, a-Si:H films involves midgap defect states as well as tail states due to disorder. These midgap states are experimentally observable both in photoconductivity and sub-bandgap absorption. DBP is a useful technique to measure the sub-bandgap absorption but it requires normalization to T&R values at high energies and its assumptions should be verified to obtain reliable absorption coefficient values at lower energies. DBP has also the advantage of using different bias light intensities to detect defect states above the Fermi level. Light soaking creates new defect states in the bandgap, which can be either neutral dangling bonds or other types of defects. Charged dangling bonds [35-37,69] and floating bonds [41,43] can be the candidates of types of defects. In this thesis study, only native and light induced defects are observed and interpreted in a-Si:H films and the densities of these defect states are estimated. In addition, the reliability of DBP technique was investigated. Detailed numerical analyses of the sub-bandgap absorption results are needed to explain the types and the distribution of defect states and also relation between photoconductivity and the density of midgap states in a-Si:H films.

**5.1. Future proposed research**

      In this thesis study, the dual beam system was established as the main goal and was used to investigate a-Si:H thin films. It was also applied to microcrystalline silicon thin films to check its reliability. The technique can be further applied to the other photosensitive materials either amorphous or crystalline. The obtained spectra of a-Si:H thin films were only used to estimate density of states and analyze midgap defect states qualitatively. Therefore, detailed numerical analyses are needed to investigate distribution of midgap states and the nature of native and light soaked defects using these spectra.

# REFERENCES

1) R. C. Chittick, J. H. Alexander, and H. F. Sterling, J. Electrochem. Soc. 116, 77 (1976).

2) P. A. Walley, Thin Solid Films 2, 327 (1968).

3) M. H. Brodsky, R. S. Title, K. Weiser, and G. D. Pettit, Phys. Rev. B 1, 2632 (1970).

4) W. E. Spear, and P. G. Le Chomber, Solid State Comm. 17, 1193 (1975).

5) W. E. Spear, P. G. Le Chomber, S. Kinmond, and M. H. Brodsky, Appl. Phys. Lett. 28, 105 (1976).

6) H. Y. Wey, H. Fritzsche, J. Non Cryst. Solids 8-10, 336 (1972).

7) W. Funs, K. Niemann, J. Stuke, in Tetrahedrally Bonded Amorphous Semiconductors, edited by M. H. Brodsky, S. Kirkpatrick, D. Weaire (American Institute of Physics, Newyork, 1974), p. 345.

8) B. T. Kolomiets, V. M. Lyubin, V. S. Maidzinski, R. A. Plisova, G. A. Federova, and E. I. Federova, Sov. Phys. Semic ond. 8, 1339 (1972).

9) D. E. Carlson and C. R. Wronski, Appl. Phys. Lett. 28, 671 (1976).

10) M. H. Brodsky, M. Cardona and J.J. Cuoma, Phys. Rev. B 16, 3556 (1977).

11) H. Fritzsche, in Proc. 7th Int. Conf. on Amorphous and Liquid Semiconductors, edited by W. E. Spear (CICL Edinburgh, 1977),p.3

12) D. L. Staebler and C. R. Wronski, Appl. Phys. Lett. 31, 292 (1977).

13) N. B. Goodman, Philos.Mag.B. 45, 407 (1982).

14) M. Grunewald, K. Weber, W. Funs, and P. Thomas, J. Phys.Colloq. 42, C4-523 (1981).

15) D. V. Lang, J. D. Cohen, J. P. Harbison, and A.M. Sergent, Appl. Phys. Lett. 40, 474 (1982).

16) J. I. Pankove, and J. E. Berkenheiser, Appl. Phys. Lett. 37, 705 (1980).

17) N. M. Amer, A. Skumanich, and W. B. Jackson, Physica 117&118B, 897 (1983).

18) I. Hirabayashi, K. Morigaki, S.Nitta, Jpn. J. Appl. Phys. 19, L357 (1980).

19) H. Dersch, J. Stuke, and J. Beichler, Appl. Phys. Lett. 38, 456 (1981)

20) M. Tanelian, N. B Goodman, H. Frizche, J. Phys. Colloq. Orsay, Fr. 42, Suppl. 10, C4-375 (1981).

21) G. O. Johnson, J. A. McMillan, E. M. Peterson, AIP Conf. Proc. 79, 329 (1981).

22) H. P. Maruska, T. D. Moustakas, M. C. Hicks, Solar Cells 9, 37 (1983).

23) B. A. Scott, J. A Reiner, R. M. Plecenik, E. E. Simonyi, W. Reuter, Appl. Phys. Lett. 40, 973 (1982).

24) D. L. Staebler, C. R Wronski, Appl. Phys. Lett. 51, 3262 (1980).

25) D. Adler, in Semiconductors and Semimetals vol.21, edited by J. I. Pankove (Academic press, Orlando, 1984) pt.A, p.291.

26) D. Adler, J. Physique (Paris), 42, C4-3 (1983)

27) M. Stutzmann, Philos. Mag. B 56, 63 (1987).

28) R. A. Street and K. Winer, Phys. Rev. B 40, 6236 (1989).

29) G. Muller, Appl. Phys. A 45, 41 (1988).

30) R. A. Street, J. Kakalios, C. C. Tsai, and T. M. Hayes, Phys. Rev. B 35, 1316 (1987).

31) G. Muller, S. Kalbitzer, and H. Mannsperger, Appl. Phys. A 39, 250 (1986).

32) Y. Bar-Yam and J. D. Joannapoulos, J. Non Cryst. Solids 97&98, 467 (1987).

33) Z. E. Smith and S. Wagner, Phys. Rev. Lett. 59, 688 (1987).

34) K. Winer, Phys. Rev. B 41, 12150 (1990).

35) G. Schumm and G. H. Bauer, Philos. Mag. B 64, 515 (1991).

36) G. Schumm and G. H. Bauer, J. Non Cryst. Solids 137&138, 315 (1991).

37) H. M. Branz and M. Silver, Phys. Rev. B 42, 7240 (1990).

38) H. M. Branz, R. Crandall, and M. Silver, Am. Inst. Phys. Conf. Proc. 234, 29 (1991).

39) S. T. Pantelides, Phys. Rev. Lett 57, 2979 (1986).

40) S. T. Pantelides, Phys. Rev. B 36, 3479 (1987).

41) S. T. Pantelides, Mat. Res. Soc. Symp. Proc. 95, 23 (1987).

42) H. M. Branz, J. Non Crys. Solids 266-269, 391 (2000).

43) R. Biswas, Y. P. Li and B. C. Pan, Mat. Rec. Soc. Symp. Proc., Vol. 609

44) R. M. Dawson, Youming Li, M. Gunes, S.Nag, R. W. Collins, C. R. Wronski, and Y. M. Li, Proc. of 11th European PVSEC, 1992.

45) G. E. Jellison Jr., V. I. Merkulov, A. A. Puretzky, D. B. Geohegan, G. Eres, D. H. Lowndes, J. B. Caughman, Thin Solid Films 377-378, 68 (2000).

46) G. D. Cody, C. R. Wronski, B. Abeles, R. Stephens, and B. Brooks, Solar Cells, 2,227 (1980).

47) J. D. Cohen, D. V. Lang and J. P. Harbison, Phys. Rev. Lett. 45, 197 (1980).

48) D. V. Lang, J. D. Cohen and J. P. Harbison, Phys. Rev. B 25, 5285 (1982)

49) C. R. Wronski and R. E. Daniel, Phys Rev. B 23, 794 (1981).

50) M. Gunes, Y. M. Li, R. M. Dawson, C. M. Fortmann, and C. R. Wronski, in Proc. of IEEE XXIII Photovoltaic Specialists Conf. (IEEE, New York, 1993), p.885.

51) P. C. Taylor, in Semiconductors and Semimetals vol. 21, edited by J. I. Pankove (Akademic Press, Orlando, 1984), p.99.

52) W. B. Jackson and N. M. Amer, Phys. Rev B 25, 5559 (1982).

53) M. Vanecek, J. Kocka, J. Stucklik, Z. Kozisek, O. Stika, and A. Triska, Solar Energy Materials 8, 411 (1983)

54) C. R. Wronski, B. Abeles, T. Tiedje and G. D. Cody, Solid State Comm. 44, 1423 (1982).

55) K. Pierz, H. Mell, J. Terukov, J. Non. Cryst. Solids 77-78, 547 (1985)

56) S. Lee, S. Kumar, C. R. Wronski, and N. M. Maley, J. Non Cryst. Solids 114, 316 (1989)

57) M. Gunes and C. R. Wronski, Appl. Phys. Lett. 61, 678(1992).

58) H. Curtins, M. Favre, in Amorphous silicon and related materials, edited by H. Fritzche, (World Scientific, London, 1989), p. 329.

59) M. Vanecek, A. Abraham, O. Stika, J. Stuchlik, J. Kocka, Phys. Stat. Sol. (a)83, 617 (1984).

60) C. R. Wronski, Z. E. Smith, S. Aljishi, V. Chu, K. Shepard, D. S. Shen, R. Schwarz, D. Slobodin, S. Wagner, AIP Conf. Proc. 157, 70 (1987).

61) G. Nobile and T. J. McMahon, J. Appl. Phys. 67, 578 (1990).

62) N. Wyrsch, F. Finger, T. J. McMahon, M. Vanecek, J. Non Cryst. Solids, 137&138, 347 (1991).

63) K. Pierz, W. Fuhs, H. Mell, Phil. Mag. B 63, 123 (1991).

64) A. Lachter, R. L. Weissfield, W. Paul, Solar En. Mat. 7, 263 (1982).

65) M. Gunes, C. R. Wronski, and T. J. McMahon, J. Appl. Phys. 76, 2260 (1994).

66) S. Wiedeman, M. S. Bennett, and J. L. Newton, Mat. Res. Soc. Symp. Proc. Vol 95, 145 (1987).

67) Z. E. Smith, V. Chu, K. Shepard, S. Aljichi, D. Slobodin, J. Kolodzey, S. Wagner, T. L. Chu, Appl. Phys. Lett. 50, 1521 (1987).

68) H. G. Grimmeiss and L. A. Ledebo, J. Appl. Phys. 46, 2155 (1975).

69) M. Gunes, C. R. Wronski, J. Appl. Phys. 81, 3526 (1997).

70) Davied E. Carlson and Sigurd Wagner, " Amorphous silicon photovoltaic systems," in Renewable Energy-Sources for Fuels and Electricity, edited by T. B. Johansson, H. Kelly, A. K. N. Reddy and R. H. Williams, Island Press, Washington, 1991.

71) M. Pinarbasi, M.J. Kushner, J.R. Abelson, J. Vac. Sci. Technol. A, 8 (3), 1369 (1990).

72) J. G. Simmons and G. W. Taylor, Phys. Rev. B, 4, 502 (1971).

73) J. G. Simmons and G. W. Taylor, J-Non-Cryst. Solids 8-10, 947 (1972).

74) H. R. Park, J. Liu, and S. Wagner, Appl. Phys. Lett. 55, 2658 (1989).

75) M. Gunes, D. Akdas, O. Goktas, R. Carius, J. Klomfass, F. Finger, J. Mat. Sci: Materials in Electronics, (accepted for publishing) (2002).

# APPENDIX A

## COMPUTER PROGRAM FOR
## SUB-BANDGAP ABSORPTION MEASUREMENT

The computer program was written by using Objectbench software. It controls lock-in amplifier, monochromator driver, and filter driver using GPIB protocol. The commands and explanations are written in regular and italic fonts, respectively.


start*: the main loop*

graphcomment$="*Comments about the graph* "

filecomment$="*Comments about the data*"

format #1 energy["energy=","eV"], average["average=","A"],

avgdevia["phase=","degree"], ratio ["Idc/Iac",""], absorp["absorption coefficient=","A"]
*defines a data format for output to a file, a graph on the screen. All expressions written here will be included in data file and graph.*

input "Enter your data file name:",dbs$ *displays a dialog box to enter a value*

open #1, file= dbs$+".dat",desc$,overwrite *opens a data file for output defined in the format statement*

open #1, graph= "dualbeam",overwrite *opens a graph box*

open #1, screen *opens a macro shell window*

input "enter the first value of energy",start

input "enter the step value for energy",step

input "enter the number of measurements for each energy",n

input "enter dc current",dcac

input "enter the initial time constant(sec)"tc

--------------------------------------------------------------------------------------------------------------
*The initial commands of SR830 lock-in amplifier*

gpibwrite(8,"OUTX 1,OVRM 1") *sets the output interface to GPIB and remote operation*

gpibwrite(8,"*RST") *resets SR830 to its default configuration*

gpibwrite(8,"*CLS") *clears all status registers*

gpibwrite(8,"FMOD 0") *sets the reference source (external or internal)*

gpibwrite(8,"DDEF 1,1,0") *selects CH1 displays*

gpibwrite(8,"DDEF 2,1,0") *selects CH2 displays*

gpibwrite(8,"ICPL 0") *sets the input coupling (AC or DC )*

gpibwrite(8,"ISRC 2") *sets the input configuration (A, A -B, I(1M$\mathbf{W}$), I(100M$\mathbf{W}$))*

gpibwrite(8,"OFSL 3") *sets the low pass filter slope*

gpibwrite(8,"IGND 1") *sets the input shield grounding (Float or Ground)*

gpibwrite(8,"SENS 23") *sets the sensitivity (\*optional)*

gpibwrite(8,"SYNC 1") *sets the synchronous filter (off or below200Hz)*

gpibwrite(8,"OFLT 8") *sets the initial time constant (depends on the chopper frequency)*

gpibwrite(8,"AGAN") *sets the sensitivity AUTO GAIN*

gosub delay2 *goes to the sub -loop to wait 4 seconds here*

gpibwrite(8,"ARSV") *AUTO RESERVE;* gosub delay2

gpibwrite(8,"APHS") *adjust the reference phase shift AUTO PHASE;* gosub delay2

--------------------------------------------------------------------------------------------------------

include"fx080601" *the program includes fx080601 flux data (macro program file) to calculate normalized current by dividing the average current to flux*

energy=start

wl=6200/energy *gives the initial wavelength*

z=0

loop: *loop for 72 different energy values (2.06eV-0.64eV)*

sum=0 ; dvsum=0

r=1 ; z=z+1

gpibwrite(8,"ARSV") *AUTO RESERVE;* gosub delay3

if energy>1 and energy<1.2 then gosub timecons *increases time constant at lower photon energies*

if energy>0.8 and energy<1 then gosub timeconsa

if energy<0.8 then gosub timeconsb

loopa: *loop to repeat the measurements for each energy*

r=r+1

gpibwrite(8,"OUTR? 1") *sends the string to read the value of CH1*

a\$=gpibread\$(8) *reads the string value of CH1 (current)*

gpibwrite(8,"OUTR? 2") *sends the string to read the value of CH2*

j\$=gpibread\$(8) *reads the string value of CH2 (phase)*

curr=val(mid\$(a\$,1)) *returns the value of the string*

? "current=",curr," A" *write the measured current values to the macro shell(screen)*

devia=val(mid\$(j\$,1))

sum=sum+curr

dvsum=dvsum+devia

average=sum/n

avgdevia=dvsum/n

loopb: *loop for standard deviation (\*optional\*). It works only if write#1 command is included in loopa (means recording all current data in to the file)*

sd1=(curr-average)**2

sd1=sd1+(curr-average)**2

sd=sqrt(sd1/n)

? "Standard deviation=",sd

gosub delay0

if energy>1 and energy<1.2 then gosub delay1

if energy>0.8 and energy<1 then gosub delay3

if energy<0.8 then gosub delay4

if r<=n then go to loopa

b$=str$(wl) *converts wl to a string value*

wv=val(mid$(b$,1,5)) *returns the value of the string*

realw=2*wv

? "Average for",energy," eV(",realw,"A)=",average," A"

ratio=dcac/average

absorp=average/y(z) *includes y(z) array from fx080601 macro file*

? "Current/flux for",energy," eV=",absorp

if 1e-8<=average and average<1e-6 then gosub sensa *if condition is satisfied it goes to sub loop to change the sensitivity*

if 1e-9<=average and average<1e-8 then gosub sensb

if 1e-10<=average and average<1e-9 then gosub sensc

if 1e-11<=average and average<1e-10 then gosub sensd

if 1e-12<=average and average<1e-11 then gosub sense

if 1e-13<=average and average<1e-12 then gosub sensf

write #1 *writes the measured data in to the file*

-------------------------------------------------------------------------------------------------------------

*procedures to adjust the speed of monochromator crank and change the wavelength*

energy=energy-step *goes the second energy value to change the wavelength of monochromator*

wl=6200/energy *calculates desired wavelength*

c$=str$(wl)

wk=val(mid$(c$,1,5))

filterw=2*wk

kf=wk-wv *difference between the following wavelengths*

d$=str$(kf)

kw=0.5*kf *for large wavelength differences since the maximum speed of monochromator crank is about 150 steps/sec*

f$=str$(kw)

wt=val(mid$(f$,1,3))

i$=str$(wt)

kg=0.3*kf

g$=str(kg)

wy=val(mid$(g$,1,3))

h$=str$(wy)

if energy=1.76 then gosub ttl *goes sub-loop to change the filter at that value*

if energy=1.36 then gosub ttl

if energy=0.8 then gosub ttl

gosub delay2

gpibwrite(14,"C") *send clear command to monochromator*

gpibwrite(14,"E") *send current enable command to monochromator*

if energy>=0.9 then gosub shortw *goes sub-loop to change the wavelength*

if energy<0.9 and energy>0.8 then gosub midw

if energy<0.8 then gosub longw

gosub delay2

if z<=71 then goto loop

-----------------------------------------------------------------------------------------------------------------

gosub delay ; ? "Wait 30 seconds to finish the experiment"

gosub back *to return the initial value of monochromator*

close #1

read dbs$+".dat",d

print d.time$ *records the time of the experiment*

if not yesnobox("Okey?") then goto start ; stop

-----------------------------------------------------------------------------------------------------------------

*sub-loops*

ttl: *changes the place of filters*

gpibwrite(8,"AUXV 1,1.4") *sets the Aux output voltage to trigger the filter driver*

gpibwrite(8,"AUXV 1,0.8")

? "Filter at",filterw," A is ready"; return

sensa: gpibwrite(8,"SENS 26") *sets the sensitivity* ; return

sensb: gpibwrite(8,"SENS 25") ; return

sensc: gpibwrite(8,"SENS 20") ; return

sensd: gpibwrite(8,"SENS 17") ; return

sense: gpibwrite(8,"SENS 14") ; return

sense: gpibwrite(8,"SENS 11") ; return

shortw:

gpibwrite(14,"V+"+d$+",S") *adjust speed of the wavelength crank*

gpibwrite(14,"G+"+d$+",S") *changes the wavelength to desired value;* return

midw:

gpibwrite(14,"V+"+i$+",S") *adjust speed of the wavelength crank for large values*

gpibwrite(14,"G+"+d$+",S"); return

longw:

gpibwrite(14,"V+"+h$+",S") *adjust speed of the wavelength crank for large values*

gpibwrite(14,"G+"+d$+",S"); return

timecons: gpibwrite (8,"OFLT 10") *changes the time constant* ; return

timeconsa: gpibwrite (8,"OFLT 11") ; return

timeconsb: gpibwrite (8,"OFLT 12") ; return

back:

gpibwrite(14,"V120,S")

gpibwrite(14,"G-6678,S") *returns monochromator to the initial value*

return

*delay loops used in the program*

delay0: t=time; delaya if time-t<tc*1000 then goto delaya ; return

delay1: t=time; delayb:if time-t<1000 then goto delayb ; return

delay2: t=time; delayc:if time-t<4000 then goto delayc ; return

delay3: t=time; delayd:if time-t<tc*10000 then goto delayd ; return

delay4: t=time; delaye:if time-t<10000 then goto delaye; return

escape: ? "cancelled" stop